12-2005

Experimental, Theoretical, and Device Application Development of Nanoscale Focused Electron-Beam-Induced Deposition

Steven Jeffrey Randolph
University of Tennessee - Knoxville

To the Graduate Council:

I am submitting herewith a dissertation written by Steven Jeffrey Randolph entitled "Experimental, Theoretical, and Device Application Development of Nanoscale Focused Electron-Beam-Induced Deposition." I have examined the final electronic copy of this dissertation for form and content and recommend that it be accepted in partial fulfillment of the requirements for the degree of Doctor of Philosophy, with a major in Materials Science and Engineering.

Philip D. Rack, Major Professor

We have read this dissertation and recommend its acceptance:

David C. Joy, Anthony J. Pedraza, Michael L. Simpson

Accepted for the Council:
Carolyn R. Hodges

Vice Provost and Dean of the Graduate School

(Original signatures are on file with official student records.)

To the Graduate Council:

I am submitting herewith a dissertation written by Steven Jeffrey Randolph entitled "Experimental, Theoretical, and Device Application Development of Nanoscale Focused Electron-Beam-Induced Deposition." I have examined the final electronic copy of this dissertation for form and content and recommend that it be accepted in partial fulfillment of the requirements for the degree of Doctor of Philosophy, with a major in Materials Science and Engineering.

Philip D. Rack

Major Professor

We have read this dissertation and
recommend its acceptance:

David C. Joy

Anthony J. Pedraza

Michael L. Simpson

Accepted for the Council

Anne Mayhew
Vice Chancellor and
Dean of Graduate Studies

(Original signatures are on file with official student records.)

Experimental, Theoretical, and Device Application Development of Nanoscale Focused Electron-Beam-Induced Deposition

A Dissertation

Presented for the

Doctor of Philosophy

Degree

The University of Tennessee, Knoxville

Steven Jeffrey Randolph

December 2005

Dedication

This dissertation is dedicated to my wife, Veronica, whose unending support and encouragement during the course of my graduate study made difficult days bearable. I also want to dedicate this work to my parents, Jeff and Debbie Randolph, for their continuous love and support throughout this process. In addition, I would like to dedicate this work to my grandfather, James Sawyers, as his confidence and interest in my success facilitated this effort. A dedication is due my uncles Chris Randolph and Roger Randolph for their consistent support. My entire family's constant support is so greatly appreciated that I wish to dedicate my education to them all. Finally, I would like to dedicate this work to my advisor and friend, Dr. Philip Rack. His support and belief in my abilities was instrumental in this accomplishment.

Acknowledgements

I would like to thank Dr. Jason Fowlkes for guiding me along in my graduate work. I consider Dr. Fowlkes my mentor and many thanks are due him. I would like to thank the members of our research group, Yuepeng Deng, Seung-Ik Jun, Ryan Rucker, and Daryl Smith along with all members of Dr. David C. Joy's research group for whose help and support I am greatly appreciative. For the help that I received at Oak Ridge National Laboratory, I would like to thank Dr. Xiaojing Yang, Kate Klein, Dale Hensley, and Darrell Thomas. Without their efforts, this work would not be possible. Finally, I would like to thank my committee members: Dr. David Joy, Dr. Anthony Pedraza, Dr. Philip Rack, and Dr. Michael Simpson. Their expertise and guidance was indispensable.

Abstract

To elucidate the effects of beam heating in electron beam-induced deposition (EBID), a Monte-Carlo electron-solid interaction model has been employed to calculate the energy deposition profiles in bulk and nanostructured SiO_2. Using these profiles, a finite element model was used to predict the nanostructure tip temperatures for standard experimental EBID conditions. Depending on the beam energy, beam current, and nanostructure geometry, the heat generated can be substantial. This heat source can subsequently limit the EBID growth by thermally reducing the mean stay time of the precursor gas. Temperature dependent EBID growth experiments qualitatively verified the results of the electron beam-heating model. Additionally, experimental trends for the growth rate as a function of deposition time supported the conclusion that electron beam-induced heating can play a major role in limiting the EBID growth rate of SiO_2 nanostructures.

In an EBID application development, two approaches to maskless, direct-write lithography using electron beam-induced deposition (EBID) to produce ultra-thin masking layers were investigated. A single layer process used directly written SiO_x features deposited from a tetraethoxysilane (TEOS) precursor vapor as a masking layer for amorphous silicon thin films. A bilayer process implemented a secondary masking layer consisting of standard photoresist into which a pattern—directly written by EBID tungsten from WF_6 precursor—was transferred. The single layer process was found to be extremely sensitive to the etch selectivity of the plasma etch. As a result, patterns were successfully transferred into silicon, but only to a minimal depth. In the bilayer process,

EBID tungsten was written onto photoresist and the pattern transferred by means of an oxygen plasma dry development. A brief refractory descum plasma etch was implemented to remove the peripheral tungsten contamination prior to the development process. Conditions were developed to reduce the spatial spread of electrons in the photoresist layer and obtain minimal linewidths, which enabled patterning of ~ 35 nm lines.

Additionally, an EBID-based technique for field emitter repair was applied to the Digital Electrostatically focused e-beam Array Lithography (DEAL) parallel electron beam lithography configuration. Damaged or missing carbon nanofiber (CNF) emitters are very common in these prototype devices, so there is a need for a deterministic repair process. Relatively carbon-free, high aspect ratio tungsten nanofibers were deposited from a WF_6 precursor in a gated cathode and a damaged triode (DEAL) device. The I-V response of the devices during vacuum FE testing indicated stable, cold field emission from the EBID cathodes. The field emission threshold voltage was shown to decrease from -130 V to -90 V after a short initiation period. Finally, lithography was performed using the repaired device to write a series of lines in PMMA with variable focus voltage. Successful focusing of the beam with increased focus voltage was evident in the patterned and developed PMMA. The I-V and lithography results were comparable to CNF-based DEAL devices indicating a successful repair technique.

Table of Contents

List of Figures

Chapter 1

Chapter 2

Chapter 3

Chapter 5

Chapter 1—Introduction

1.1 Introduction

The ability to manipulate and process materials at the nanoscale with excellent reproducibility is vital to the advancement of the field of nanotechnology. Consequently, there has been a surge in the demand for the improvement of existing processing techniques as well as for the development of novel methods. In response to this demand, electron-beam-induced deposition (EBID) has received considerable attention in recent years as a viable nanoscale processing technique. EBID is the process by which a solid material can be deposited onto a solid substrate by means of an electron-mediated decomposition of a precursor molecule (a compound containing the species to be deposited). Typically, the precursor is a vapor, but EBID may also be performed using a liquid or viscous solid condensed on a substrate. The ideal metallic EBID process can be visualized as shown in Figure 1-1; a metal-containing vapor, *M*—*X*, is dissociated by an electron beam to produce a metal deposit, *M*, on a substrate, *S*, and a volatile byproduct, denoted by *X*.

One of the earliest reports of EBID was in regards to a common effect in electron microscopy known as carbon contamination or carbon staining. As an unwanted artifact of electron microscopy, carbon contamination occurs when an electron beam is projected onto a surface in an electron microscope in the presence of a carbonaceous species such as those found in vacuum pump oils. Hart *et al.* reported that high-energy electron

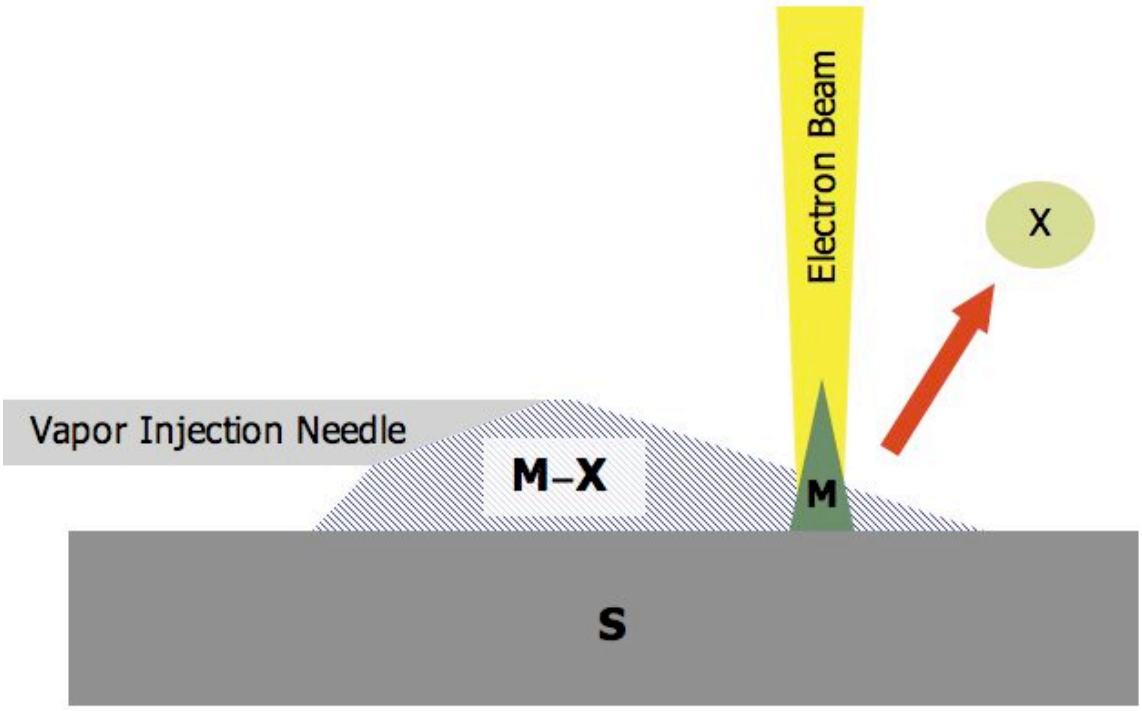

Figure 1-1: Generalized EBID Mechanism

A metal-containing precursor, MX, is introduced to a substrate, S. The substrate is exposed to an electron beam in the region of the incident vapor plume. The electron bombardment induces a dissociation reaction resulting in a metal deposit, M, and a volatile byproduct, X.

bombardment of a substrate in the presence of a carbon-containing gas resulted in contamination of the surface with a carbon film. The work focused on the effects of substrate temperature and the residual gas atmosphere and showed that contamination is due to an electron interaction with the precursor.[1]

1.2 Experimental Setup

Controlled electron-beam-induced deposition must be performed in a vacuum environment to reduce electron scattering and deposit contamination. The most common EBID setup utilizes a modified scanning electron microscope (SEM)[2], but a transmission electron microscope (TEM)[3], a scanning transmission electron microscope (STEM)[4], and a scanning tunneling microscope (STM)[5] have all been used to investigate EBID.

Regardless of the type of system used, modification is usually necessary to accommodate EBID experiments. Typically, the system is fitted with some type of vapor injection system that allows precursor to flow into the vacuum chamber from a source located outside of the chamber. Figure 1-2 is a generalized schematic of an EBID system built on a modified SEM. Essentially, the only modification to the SEM in Figure 1-2 is the attachment of a vapor injection system. The use of an injector capable of three-dimensional positioning allows for vapor localization at the beam interaction region.

The actual dynamics of the vapor flow in a given injection system is a complex function of the vacuum pumping speeds, chamber geometry, injector geometry, precursor vapor pressure or flow rate, and vacuum lines connecting the precursor source

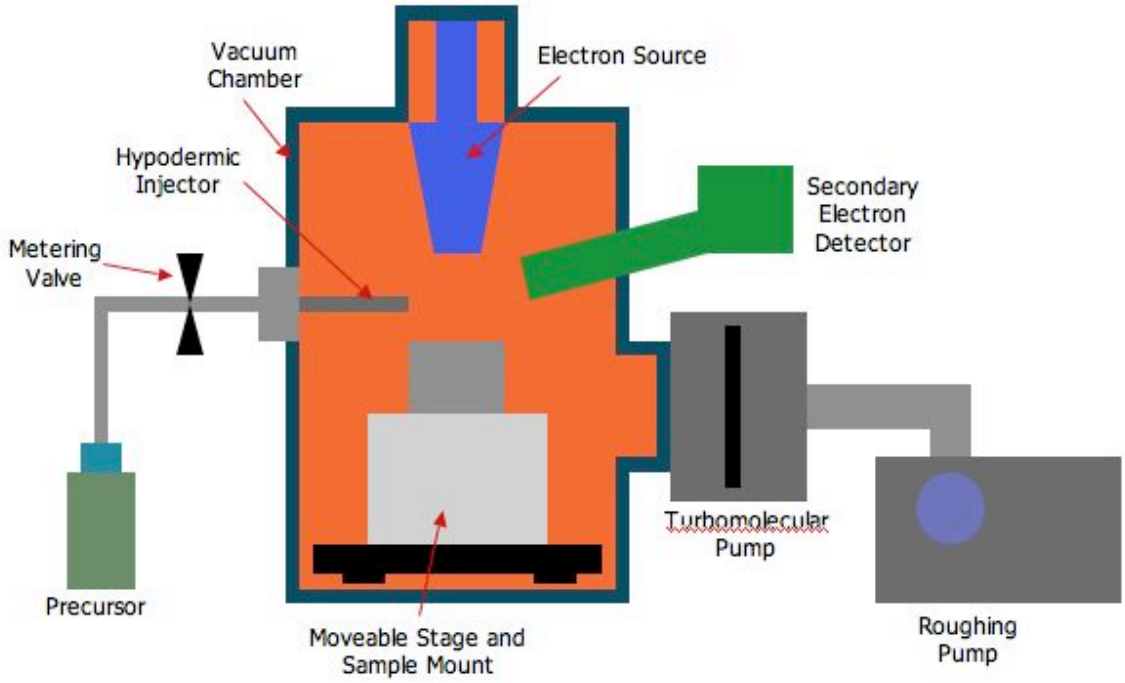

Figure 1-2: EBID System Schematic

A schematic representing a typical SEM modified for use in EBID experimentation. The system is essentially a standard SEM equipped with a vapor injection system capable of precursor delivery to the substrate.

to the chamber. The complexity of these interactions and their dependence on the individual system eliminate the possibility of standard, generalized flow calculations to predict vapor dynamics. Koops *et al*. proposed a computer-controlled vapor injection system for use with EBID.[6] Others have performed analysis of the vapor flow in their own systems.[7] In addition, analytical models of molecular beams emanating from tube sources have been developed which may be used to estimate the properties of the injected vapor flow.[8] However, the most reliable and accurate prediction of vapor flow dynamics is probably achieved by finite element modeling (FEM) of the particular injection system and vapor of interest.

The standard electron microscope is typically only capable of scanning simplistic patterns such as squares, rectangles, lines, and other simple geometries. In order to deposit more complex features by EBID, integration of a pattern generator is usually necessary. Two-dimensional pattern generators can be used to force the electron beam to scan a desired pattern on the substrate, resulting in the desired deposit geometry.[9,10] In addition to standard pattern generators, a three-dimensional pattern generator has been developed and reported for use in focused ion beam (FIB) chemical vapor deposition (CVD).[11] While this design was used specifically for FIB CVD patterning, an analogous system could be applied to an EBID setup.

More recently, prototype multi-beam systems have been investigated for use in depositing several EBID features in parallel.[12] This system utilized a single Schottky thermal field emission (FE) flood electron source. The single beam was split by irradiation of an array of 100 apertures, resulting in 100 electron sources, each of which

were used to perform EBID. Initial results have indicated that the system can perform parallel, unfocused EBID. Focus grids and beam blanking capabilities to allow for high resolution, controlled EBID have been scheduled for future integration with the multi-beam system.

1.3 EBID Materials, Precursors, and Nanostructures

Probably the most important single factor in the EBID process is the chemistry of the deposition precursor. The precursor must produce a solid deposit and volatile byproducts as a result of an electron-stimulated dissociation reaction. A wide array of precursor materials that meet these criteria have already been investigated and found to be useful in the study of EBID. For ease of reference, Table 1 summarizes many of the materials that have been successfully deposited by EBID and their corresponding precursors, and other important experimental parameters.

Perhaps the most well studied EBID deposition material is tungsten, for which there are two main precursors: $W(CO)_6$[13] and WF_6[2]. While both precursors are useful, there is evidence to suggest that WF_6 results in a higher purity tungsten deposit.[14] The lack of carbon in WF_6 results in less carbon incorporation into the deposit than occurs with $W(CO)_6$. In addition, the high vapor pressure of WF_6 is more accommodating than that of $W(CO)_6$, which is a solid at room temperature and must be heated to maintain adequate flow into the EBID chamber. The high vapor pressure of WF_6 also allows for EBID to be performed at higher operating pressures; recent evidence indicates that higher

Table 1: Reported EBID Materials and Precursors

Reference Number	Material	Precursor	EBID System	Comments
[15]	Al	$Al(CH_3)_3$	SEM	-
[13]	Au	$Me_2Au(tfac)$ *	E-Beam Lithography	Dimethyl-gold-trifluoro-acetylacetonate
[16]	C	$C_{14}H_{10}$ *	SEM	Phenanthrene
[17]	Co	$Co_2(CO)_8$	ESEM	-
[2]	Cr	$Cr(C_6H_6)_2$	SEM	-
[18]	Cu	hfac-Cu-TMVS*	SEM	Hexafluoroacetylacetonato-Cu(I)-trimethylvinyl-silane
[19]	Fe	$Fe(CO)_5$	SEM	-
[20]	GaAs	TMG and AsH_3*	SEM	tri-methyl-gallium; AsH_3 cracked at 1273 K
[3]	GaN	D_2GaN_3 *	TEM	Perdeuterated gallium azide
[21]	Mo	$Mo(CO)_6$	SEM	-
[5]	Ni	$Ni(CO)_4$	STM	-
[22]	Os	$Os_3(CO)_{12}$	-	-
[23,24]	Pd	$Pd(OOCCH_3)_2$*	SEM	Palladium acetate
[25]	Pt	$Pt(PF_3)_4$	Auger	-
[26]	Rh	$[RhCl(PF_3)_2]_2$	SEM	-
[22]	Ru	$Ru_3(CO)_{12}$	-	-
[27]	Re	$Re_2(CO)_{10}$	TEM	-
[28]	Si	SiH_2Cl_2	Auger	-
[29]	Si_3N_4	N_2 *	Auger	Nitrogen on Si (100)
[30]	SiO_x	TEOS *	Ion/Electron Source	Tetraethoxysilane
[31]	TiO_x	$Ti(-OC_3H_7)_4$	Auger	-
[13]	W	$W(CO)_6$	E-Beam Lithography	-
[2]	W	WF_6	SEM	-

partial pressures of precursor during deposition results in higher purity deposits.[32]

While tungsten is certainly a technologically useful material, it is vital to the success of EBID as a nanofabrication technique to be able to deposit a wide range of materials. For instance, EBID has been used to deposit metals such as chromium[2], rhodium[26], iron[19], cobalt[17], platinum[25], copper[18], palladium[23], aluminum[15], molybdenum[21], osmium[22], nickel[5], rhenium[27], and ruthenium[22].

In addition to the aforementioned metals, certain non-metals, semiconductors, and insulators may also be deposited by EBID. For instance, Fujita *et al*. reported deposition of carbon from a phenanthrene precursor[16] as opposed to residual gases in the vacuum chamber. Other non-metals such as gallium arsenide[20], gallium nitride[3], silicon[28], silicon nitride[29], silicon oxide (SiO_x)[30], and titanium oxide (TiO_x)[31] have also been reported.

1.4 EBID Applications and Nanostructures

The wide array of materials that can be deposited and the potential for high-resolution processing make EBID an attractive tool for many nanoscale fabrication applications. The ability to deposit metallic lines with EBID has proven useful for direct-write wire and interconnect fabrication. Silvis-Cividjian *et al*. demonstrated the deposition of ~ 10-nm carbon nanowires (and dots) by using a STEM and a C_2H_5 precursor.[4] In addition to carbon, wires and interconnects have been fabricated from a variety of materials including nickel[5], cobalt[17], platinum[33], rhodium[34], gold[35], and tungsten[36]. Gold deposited by EBID has been used to form interconnects between

electrodes and carbon nanotubes (CNT)[37] and single-walled carbon nanotubes (SWNT)[38].

An emerging application for which EBID has shown great promise is in the field of photolithographic mask repair. The high cost of mask sets have required that masks containing defects be repaired, rather than re-written. Clear defect repair of an extreme ultraviolet (EUV) mask can currently be performed using FIB techniques.[39] However, the ion implantation inherent to FIB mask repair can disrupt the highly sensitive optical properties of the transparent region.[40] Electron bombardment is less likely to have these adverse effects; therefore, EBID can be used as a damage-free clear defect repair technique using opaque EBID materials.[41]

The individual capabilities of some EBID systems may allow for the generation of complex two-dimensional or three-dimensional features. Utke *et al*. reported the deposition of three-dimensional copper nanostructures that consisted of a vertical fiber deposited on the flanks of a horizontal fiber as shown in Figure 1-3.[18] The horizontal fibers shown in Figure 1-3 were grown using an EBID growth technique that utilizes a slow linear scan where there is overlap between adjacent pixels, so that features may be deposited over free space. Detailed explanations of the horizontal growth effect as observed in EBID[16] and in the analogous FIB[42] process have been published. Two-dimensional rastering via a pattern generator during EBID can also yield dimensionally higher-order features. Koops *et al*. produced leaning nanofibers and a helix using a pattern generator[9] and Ueda *et al*.[10] produced bent carbon nanowires and a mesh pattern with a pitch of approximately 250 nm.

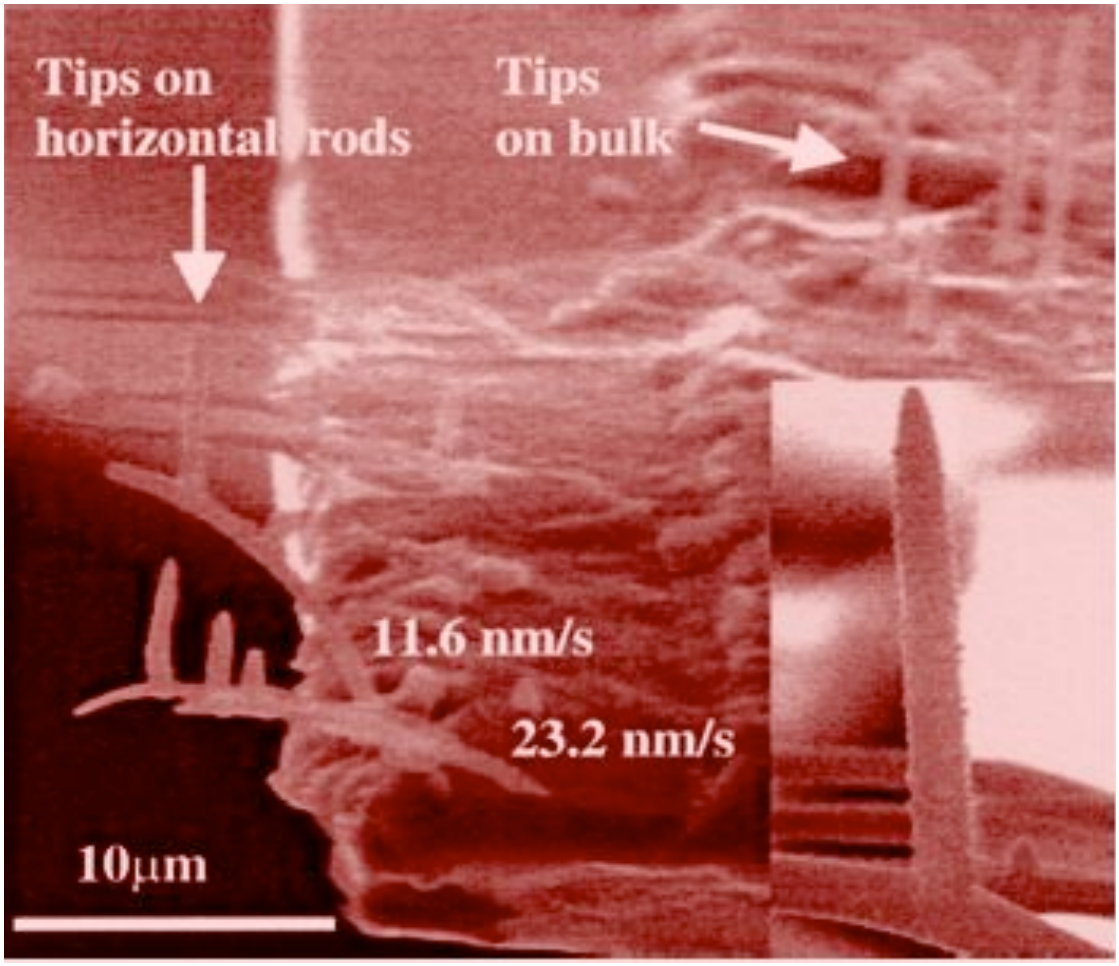

Figure 1-3: Three-dimensional copper nanostructures deposited by EBID

An electron micrograph of copper nanostructures fabricated by depositing a horizontal fiber followed by the deposition of a vertical fiber on the side of the horizontal fiber. The beam scan rates are noted on the micrograph.

Fiber-like nanostructures can be deposited by EBID by placement of a focused electron beam at a single pixel for an extended time. Similar to the vertical fibers shown in Figure 1-3, high aspect ratio fiber structures have been deposited for a wide array of materials such as cobalt[17], carbon[34], and tungsten[43]. The precise placement of high aspect ratio, sharp, metallic tips have resulted in the popularization of EBID for use in FE devices. Koops *et al*. reported the deposition and FE characterization of gold "supertips" with tip radii of less than 7 nm. Some of these tips showed stable emission at an extraction voltage of 210 V (cathode to anode distance was not reported), and the confined emission pattern for the gold supertip exhibited an angle of ± 7.2^{o}, whereas that of a tungsten etched FE tip was ± 30^{o}.[44]

As opposed to only depositing field emission cathodes, EBID has also been used to rapidly fabricate FE device prototypes. Murakami *et al.* fabricated an entire platinum nanofiber-based FE device using EBID. In this work, EBID was used to deposit an insulating SiO_2 aperture, followed by EBID deposition of a platinum gate. A platinum nanofiber emitter was then deposited in the aperture and the gate was connected to an electrical lead by means of an EBID platinum wire. The resulting devices exhibited Fowler-Nordheim behavior indicating field emission from the platinum tip.[45] An electron micrograph of the completed FE device is shown in Figure 1-4. More recently, platinum EBID nanostructures were used as FE cathodes for planar microtriode arrays.[46]

EBID has also been used to integrate FE devices with scanning probes for purposes of localized electron delivery in scanning probe microscopes. Lehrer *et al*. replaced the apex of a standard silicon probe with a flat "mesa". The probe was then

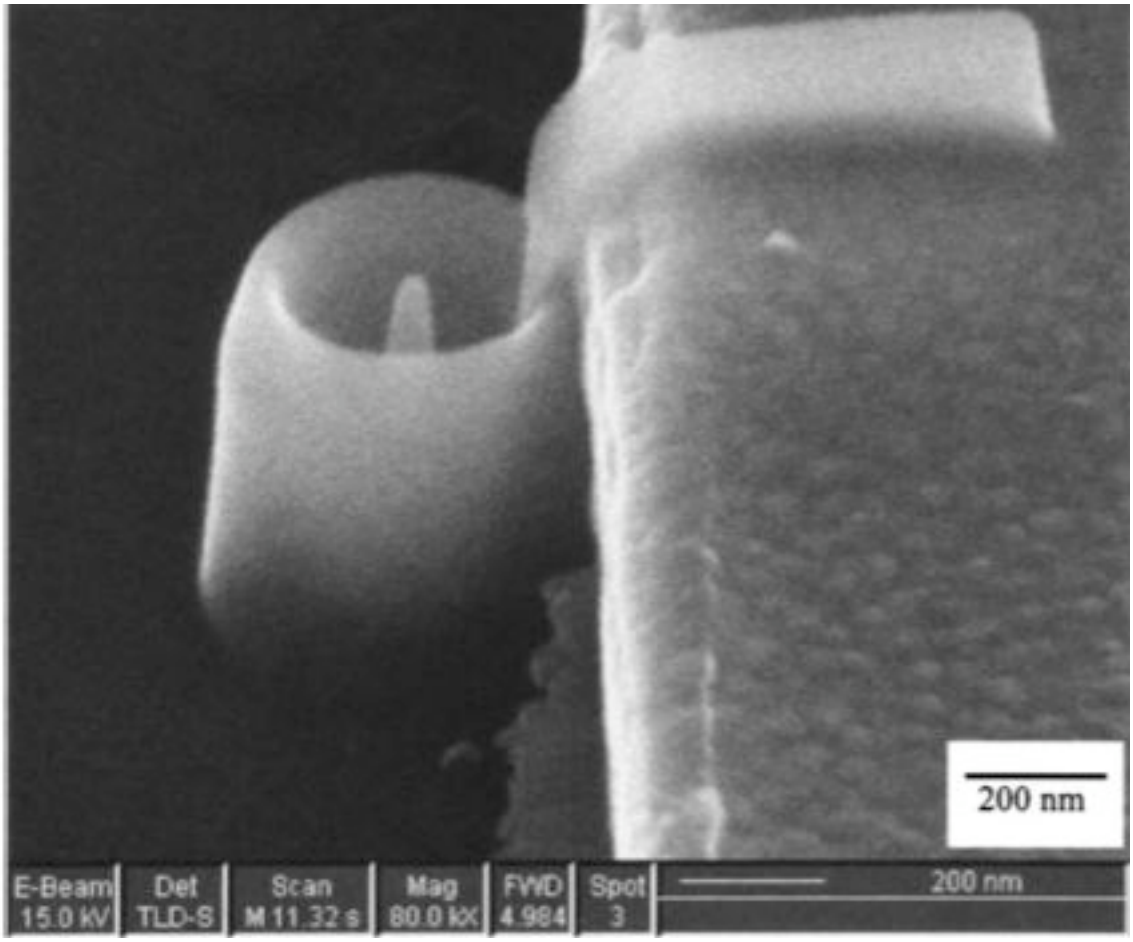

Figure 1-4: SEM Micrograph of EBID-Fabricated FE Device

An electron micrograph of a FE device fabricated entirely by EBID. An insulating SiO_2 cylinder was topped with a platinum gate, followed by platinum nanofiber deposition and deposition of a platinum interconnect.

thermally oxidized and coated with a platinum film. FIB was used to define an aperture in the platinum-silicon dioxide layers in which a platinum nanofiber was deposited as an electron source. It was found that the FIB process was not suitable for this application and for various reasons led to high leakage currents. A combination of FIB and wet etching to define the aperture was found to mitigate the problem.[47]

Unconventional electron sources have also been shown to be compatible with the EBID process. For instance, nanostructures have even been fabricated by using multiwalled CNT as electron sources, as opposed to the usual use of an electron microscope. Dong *et al*. used a biased CNT-tipped atomic force microscope (AFM) cantilever to deliver electrons to a silicon substrate in order to deposit carbon from residual chamber contamination.[48] In a similar effort, Arai *et al*. used CNT functionalized with ruthenium dioxide nanoparticles as an electron source for depositing tungsten.[49] These types of applications tend to suggest that EBID could offer the potential of being a type of "self-sustaining" technology for FE source fabrication, where EBID electron source arrays are used to perform EBID and create more massive arrays.

EBID deposition has also been used in applications that require deterministic catalyst material growth. For instance, EBID has been used as a means for direct-write deposition of cobalt catalyst for CNT growth[17] and ferrous catalyst for SWNT growth[50]. A similar effort was reported by Lee *et al*. in which a palladium catalyst was deposited by EBID as a catalyst for selective electroless plating of copper and nickel.[51] Djenizian *et al*. used EBID to deposit carbon patterns as a mask for selective electrochemical deposition of gold on silicon. Using this technique, sub-100 nm lines of gold were

fabricated on a silicon substrate.[52]

Optical applications utilizing EBID have also been reported, such as fabrication of a periodic transparent nano-optic pattern. For this application, an array of SiO_2 nanofibers was deposited on the edge of a transparent SiO_2 prism in such a manner as to trap light of 632 nm wavelength.[53] Additionally, Sánchez *et al*. deposited conformal Si_mO_{2n} on a metal tip of complex geometry for use in apertureless near-field optical probes.[54]

1.5 Fundamental Studies of EBID

The preceding sections have assessed much of the experimental work performed since the late 1970s in the field of EBID. While EBID may be used to deposit a variety of materials for many applications, EBID process predictability is still lacking. Therefore, it is necessary to obtain a greater fundamental understanding of EBID, so that the technique can be optimized for more advanced applications requiring greater dimensional, compositional, and morphological control. Widely used fabrication techniques such as reactive ion etching and various forms of physical and chemical vapor deposition have been studied for decades. As such, there is a good physical and empirical understanding of the processes involved in these fabrication techniques, which has continuously resulted in a higher degree of control and predictability.

In order for EBID to be accepted into the mainstream of nanofabrication, the same levels of control and predictability are essential. Consequently, a number of physical and

empirical investigations have been performed, the results of which are reviewed in the remainder of this section.

Acquiring *in-situ* control of the EBID process is probably one of the most elusive objectives in the study of EBID. Consequently, considerable effort has been given to increasing process control. Rack *et al*. used an energy dispersive x-ray spectrometer (EDS) attached to a Hitachi S-3500N ESEM providing real-time, *in-situ* compositional measurements during tungsten EBID.[55]

Bret *et al*. proposed an *in-situ* method for controlling EBID nanofiber growth by monitoring the current flow through the substrate during deposition, i_s. They showed that the current decrease during deposition due to electron scattering outside of the nanofiber ultimately reaches a material-dependent plateau value, $i_{plateau}$. The change in current as a function of time (or growth height) was empirically shown to follow a first order decay given by Eq. (1.1),

$$\Delta i(t) = \left(i_s - i_{plateau}\right)\left[1 - \exp\left(\frac{-t}{\tau}\right)\right] \qquad \text{Eq. (1.1)}$$

where the decay constant, τ, was shown to be a strong indicator of defocus or precursor deficiency.[56]

Other *in-situ* rate monitoring strategies have been employed for transparent EBID materials. The combination of a photodiode, a silicon mirror, and a 514-nm wavelength laser was used to monitor the growth rate and optical properties of transparent EBID deposits during deposition.[57] The resultant reflectivity measurements were used to characterize the deposit thickness, as well as the complex and real parts of the refractive indices of carbon, SiO_x, and TiO_x.

One of the most critical aspects of nanofabrication process control is the minimum attainable feature size. In efforts to establish EBID as a formidable nanofabrication technique, there has been a push to demonstrate the high-resolution potential of EBID. However, to make informed, and at least qualitative, predictions of feature size, it is necessary to have a firm grasp of the physics of EBID. Consequently, there is a considerable effort directed at determining the physical processes that determine the minimum feature size attainable by EBID. To date, the complexity introduced by the numerous variables such as electron-solid interactions, vapor-surface interactions, electron-vapor interactions, as well as a plethora of EBID system variables has limited our understanding of feature size from a physical standpoint.

EBID resolution is actually dependent upon a combination of system variables and physics. For instance, the spot size of an electron probe and, subsequently, the EBID feature size are highly dependent on the beam energy. Higher beam energies result in smaller electron probe sizes and thus result in smaller features as observed by Djenizian et al. [58] In the case of the beam energy dependence, an increase of a system variable (the accelerating voltage) produces smaller beam diameters, and the resultant feature is smaller. EBID feature sizes in the sub-10 nm regime have been reported recently by using high-energy electron beams. Tungsten dots of 3.5 nm diameter[59] and 1 nm diameter[60] have been fabricated using 200 keV electron beams in a TEM. Recently, an array of tungsten EBID dots of having diameters of ~ 1.2-nm were deposited on a 4-nm pitch were successfully deposited and imaged in a STEM.[61]

While extraordinary lateral resolution is attainable at high energies (small spot sizes), it is important to note that the smallest of features are also very thin (on the order of a few nanometers). This is not a problem for some applications, however for applications requiring standard microfabrication processing subsequent to EBID (i.e. reactive ion etching, etc.), the thickness may be inadequate to survive post-EBID processing. Unfortunately, if the deposition time is increased to increase the deposit thickness, the physics of electron-solid interactions begin to dominate (as opposed to the system variable), and the lateral dimension increases. It is a well-documented phenomenon in EBID processing that there is a lateral broadening of the feature as the deposition time or thickness is increased. Figure 1-5 shows a curve representing the base broadening as a function of time as determined by Kohlmann-von Platen *et al*. Since the secondary electron (SE) yield approximately increases as a secant function with the angle of beam incidence, the thickening of the nanofiber base was attributed to the topographic SE yield increase.[62]

The resolution-limiting role of SE in long timescale EBID has made it a focal point of numerous investigations. Silvis-Cividjian *et al*. used computer simulations to predict the profiles and ultimate resolution of the EBID process. These simulations confirmed their hypothesis that SE were the root cause of base broadening.[63] However, the simulation neglected the effects of the primary (PE), backscattered (BSE) and forwardscattered (FSE) electrons due to their high energies relative to SE. Since typical dissociation cross-sections peak at energies comparable to that of SE energies, the model assumed that only SE could induce deposition events. However, the governing

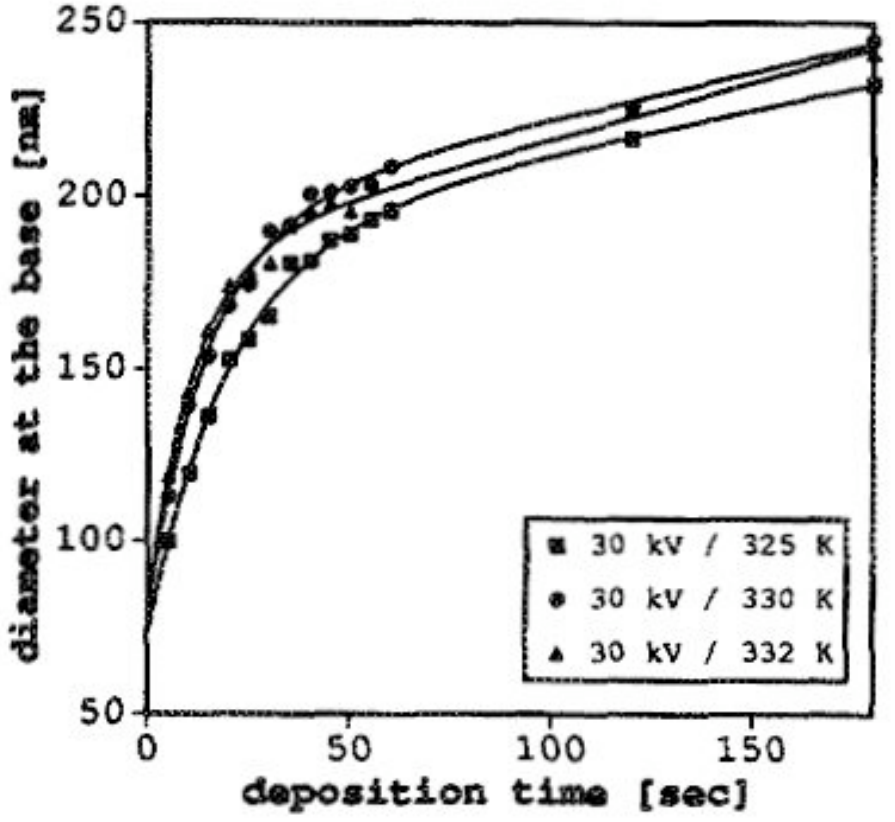

Figure 1-5: Time Evolution of Tungsten Nanofiber Base Diameter

A plot obtained showing the increase in the diameter of a tungsten nanofiber at its base with increased deposition time. This effect was attributed to enhanced secondary electron emission from the deposit.

assumption in any EBID simulation is the form and magnitude of the electron impact dissociation cross-section of the precursor molecule. As this quantity—which is a strong function of electron energy—is usually not readily available in the literature, it is necessary to make assumptions and approximations. The model of the dissociation cross-section assumed in the simulation by Silvis-Cividjian *et al*.[63] grossly underestimates the probability of high energy dissociation events.[64] Using a modified model of the dissociation cross-section that more accurately represents the high energy dissociation regime, Fowlkes *et al*. provided evidence that PE, BSE, and FSE also contribute significantly to EBID, depending on the conditions of the experiment.[64]

Fujita *et al*. suggested that in perpendicular nanofiber deposition, BSE contribute to the base-broadening phenomena. They also determined that FSE as well as SE emitted from the nanofiber flanks resulted in a change in nanofiber shape during growth.[16] More recently, Fowlkes *et al*. developed a Monte-Carlo-based computer simulation of EBID that included contributions from all types of electrons, as well as incorporated the effects of vapor dynamics. This work showed that indeed SE, BSE, and FSE all contribute to some degree in the base-broadening phenomenon. An interesting result was that the PE-induced vertical deposition rate could be high enough to "outrun" the base-broadening effect. Even though the high energy of the PE make them less likely to induce a dissociation event (based on the dissociation cross-section), the disproportionately high flux of PE relative to all other electrons results in significant PE-induced contributions.[64]

In addition to the studies regarding optimization of the process resolution, a great deal of effort has been concentrated on determining the factors affecting the deposition

rate of EBID. This has significant practical implications for EBID; regardless of the resolution, the rate of deposition must be high in order to maximize the usefulness of the technique. Several investigations of growth rate enhancement have shown that a variety of parameters influence the growth rate including the nanostructure geometry, precursor flux, beam energy, beam current, temperature, and the scanning parameters.

Kohlmann-von Platen *et al*. investigated the effects of the scan rate on the EBID deposition rate. Their results indicated that during a dwell time, the electron beam is continuously decomposing the adsorbate; therefore, the deposition rate continuously decreases during the dwell time. The pixel becomes repopulated with precursor during the remainder of the loop time (when the beam is not irradiating the pixel of interest) resulting in high efficiency deposition at long loop times. They concluded that long loop times coupled with short dwell times resulted in high growth rates.[65] However, it is important to note that this result is highly dependent upon the current density and precursor flux, as well as the beam energy. Fujioka *et al*. showed, in agreement with the decreasing dissociation cross-section, that the deposition rate of iron decreased with increasing beam energy when the beam was rastered over a 5,000-μm^2 area.[66]

Other studies have been directed at determining additional parameters in EBID and their effects on resolution, growth rate, morphology, etc. The work of Bret *et al*. revealed the importance of vapor dynamics on the EBID process. They determined that there was a strong correlation between the scan direction relative to the vapor flow and the growth rate, and that higher deposition rates could be obtained with higher scan rates. As is demonstrated in Figure 1-6, the growth rate increased as the scan progressed

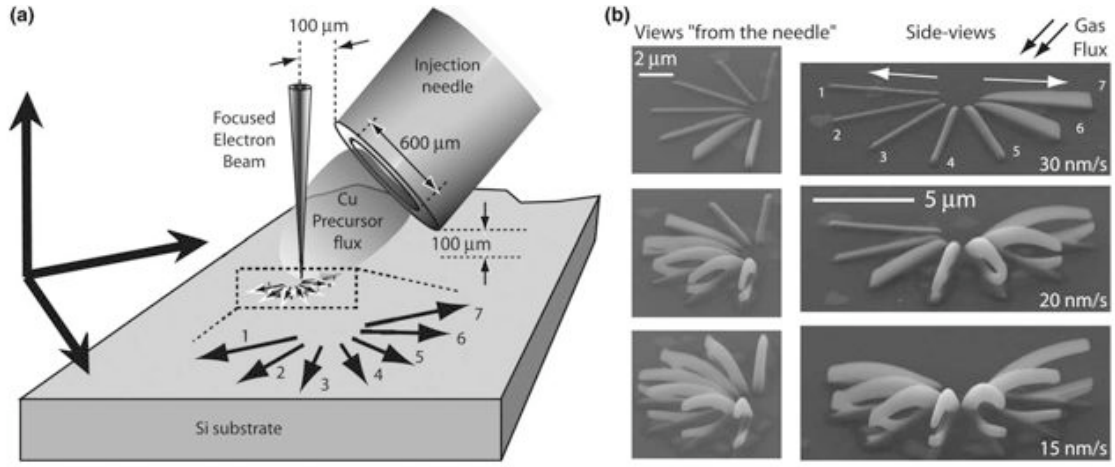

Figure 1-6: Effects of Scan Direction of EBID

A figure showing (a.) a schematic of the experimental setup used by Bret *et al*. the study the effects of scan direction, and (b.) electron micrographs of the results of the scan direction experiments.

Reprinted from Microelectron. Eng. **78-79**, T. Bret, I. Utke, and P. Hoffmann, Influence of the beam scan direction during focused electron beam induced deposition of 3D nanostructures, Page 308, 2004, with permission from Elsevier.

towards the injection needle indicating the sensitivity of EBID to vapor flow conditions.[67] As expected, the EBID process is also very sensitive to the focus conditions of the electron beam. Liu *et al*. systematically studied the effects of focus change on EBID deposited tungsten lines. As the beam was scanned, the focus was reduced, resulting in a spreading over a large area. Using incremental defocus, they were able to fabricate broken lines and self-supporting nanowires.[68]

Xie *et al*. showed that a flood exposure of electrons could be used to selectively perform EBID under certain circumstances. A porous alumina substrate consisting of an array of nanoholes was irradiated in the presence of tungsten hexacarbonyl and deposition occurred only in the bottom of the holes. The precursor was delivered below the specimen, so only the electrons that could penetrate the substrate caused deposition. Only the very thin layer of alumina at the bottom of the holes allowed transmission of electrons, therefore the holes were selectively filled with tungsten. Calculations showed that the level of deposition was in direct correlation to the electron intensity.[69]

Another important fundamental parameter in EBID is the effectiveness of the precursor to cleanly deposit the material of interest. For applications with stringent materials requirements, the compositional and microstructural properties of EBID deposits are of utmost importance. While there have only been a limited number of studies of this nature, a few key works have begun to address these issues. Luisier *et al*. studied and compared four copper precursors and found that the deposition rate of all precursors followed the familiar Langmuir adsorption isotherm with each exhibiting a different thermodynamic parameter. The most thermodynamically unstable of these

precursors—(hfac)Cu(I)(VTMS) and (hfac)Cu(I)(DMB)—produced deposits with the highest copper content and the highest conductivity.[70]

Carbon is the most common deposit contaminant in EBID due to the fact that many of the precursors are organics or organometallics. These carbon-containing precursors are more likely to introduce contamination into the deposit, as is illustrated by the difference between deposition of tungsten from $W(CO)_6$ and WF_6. Deposition of tungsten from the fluorine-based precursor can result in high purity tungsten deposits.[14,32] Recent evidence has suggested that deposition conditions such as pressure, beam current and energy can also have an effect on the composition and microstructure of tungsten deposits.[32] In addition, hydrocarbons from pump oils constitute a large fraction of the contamination in a vacuum chamber and result in deposition of carbon.[48]

Bret *et al*. studied a variety of organic precursors for deposition of carbon.[71] They determined that higher deposition rates could be obtained by using short-chained carboxylic acid precursors. The composition of deposits from all precursors contained only oxygen, hydrogen, and amorphous carbon. All of the characterized deposits were found to contain a high percentage of carbon, with 90% being sp^2-hybridized.

Post-EBID processing, such as heat treatment, has profound effects on deposit micro-/nanostructure. Shimojo *et al*. used electron diffraction and electron energy loss spectroscopy to determine the effects of vacuum annealing on the nanostructure of EBID iron. Iron pentacarbonyl was used to deposit a series of dots and rods. The as-deposited structures consisted of amorphous carbon and iron. A one-hour heat treatment at 873 K in ultrahigh vacuum resulted in the formation of several crystalline phases including α-

Fe, Fe_5C_2, Fe_7C_3, and Fe_2C. All of these phases are magnetic which showed that magnetic iron-based nanostructures could be deposited by EBID.[72]

Chapter 2—Experimental Setup and Procedure

2.1 Introduction

The work to be presented in this dissertation was performed on the same EBID system using many common experimental techniques. To avoid redundancy, this chapter represents a broad description of the experimental setup and techniques that are applicable to all subsequent work throughout this dissertation. The second section of this chapter describes the EBID system used for all the experiments, as well as the methods used to control the process variables. Focus will be placed on the SEM adjustment techniques used to obtain the non-standard SEM conditions necessary for EBID. The third and final section focuses on the vapor injection system and its proper adjustment. The result of this chapter is a stand-alone general overview and experimental guide to EBID as used in this body of work.

2.2 EBID System

All experimental work discussed in the subsequent chapters was carried out in a variable pressure scanning electron microscope (VPSEM) equipped with a thermal field emission electron source. The particular VPSEM used for the experiments detailed in chapters 3, 4, and 5 was a Hitachi model S-4300SE/N. A digital photograph of the microscope setup is shown in Figure 2-1.

Figure 2-1: Experimental EBID System—Modified Hitachi S-4300SE/N

Digital photographs of the Hitachi S-4300SE/N variable pressure scanning electron microscope (upper image) used to perform EBID experiments. The SEM was equipped with a vapor injection system (lower image) to allow for localized precursor vapor delivery. The injection system consists of a three-dimensional wobble stick positioner fitted with a hypodermic needle for highly localized and directional vapor delivery.

The use of a field emission VPSEM offers many advantages over other types of SEMs, especially for EBID applications. The stable emission current of thermal field emission SEMs allow for greater control and reproducibly of experiments. Thermionic filament-based SEMs typically require filament saturation due to continuous performance degradation. This leads to differences in the probe geometry from experiment to experiment, making controlled experiments more difficult. Additionally, the precursor vapors used for EBID are typically corrosive to thermionic emitter filaments and normally accelerate emitter degradation and loss of emission current.

The column of the Hitachi S-4300SE/N is equipped with a vacuum-interlocked gun valve that ensures that the electron source is not exposed to damaging levels of precursor gases. A combination Penning/Pirani vacuum gauge measures the chamber pressure, which controls the position of the gun valve. The chamber vacuum level is divided into three pressure regions: high pressure (atmosphere - 10 Pa), low vacuum (10 Pa – 10^{-3} Pa), and high vacuum (< 10^{-3} Pa). During pumpdown, when the pressure reaches 10^{-3} Pa, the system crosses over to high vacuum mode, which opens the gun valve and allows the SEM to be operated. For EBID purposes, it is desirable to operate at pressures greater than this lower limit, but still not damaging to the electron source. Fortunately, the SEM is capable of maintaining high vacuum status for an order of magnitude above this lower limit. For example, if a high pressure of gas is introduced into the system, the interlock will cause the microscope to enter low vacuum state and the gun valve will subsequently close. High vacuum state will only be achieved when the pressure returns to 10^{-3} Pa. At this point, a low gas flow may be introduced and the

interlock will not trip until the pressure exceeds 10^{-2} Pa. In this way, the interlock may be partially bypassed and the operating pressure of the SEM increased to ten times the interlock setpoint.

The Hitachi S-4300SE/N is equipped with a variety of controls that allow for manipulation of variables of interest in EBID studies. One such variable is the incident beam current, which is affected by a number of variables such as the beam energy, gas pressure, and the extraction voltage on the electron source. However, the most direct method of controlling the incident beam current is by changing the condenser lens setting. The condenser lens is adjusted by a parameter known as the "coarse" and "fine" settings on the Hitachi S-4300SE/N. The beam current may also be adjusted by changing the gun brightness, which is controlled by extraction voltage applied to the emitter. The incident current was measured by focusing the beam in a Faraday cup and recording the current collected at the sample with a picoammeter.

2.3 Vapor Injection System Description

In order to deliver a high, localized vapor flux, the SEM was fitted with a gas injection system. The injection system consisted of a wobble stick capable of three-dimensional positioning inside the chamber. A digital photograph of the mounted vapor injection system is included as an inset in the previously referenced Figure 2-1. A hypodermic needle was attached to the end of the wobble stick so that the vapor flow could be localized and directed to the desired deposition point. A close-up photograph

and an illustration are shown in Figure 2-2 to provide a more detailed look at the vapor injection system.

Accurate positioning of the needle at the point of irradiation was obtained by bringing the needle tip into the field of view of the SEM at low magnification. While imaging the needle tip, the wobble stick was positioned such that the direction of flow would pass directly over the region to be irradiated. The distance between the needle and the substrate was determined by focusing on the needle tip and recording the working distance, followed by the same procedure for the surface. The difference between the two working distances represents the height of the tip above the surface. Typically, the needle was first adjusted to the desired working distance (usually 7-10 mm). The sample was then moved closer to the needle until they come in contact as evidenced by movement of the needle. The sample was then lowered slightly so that the needle and surface were no longer in contact. This final lowering is done to prevent movement of the needle when the stage is moved between deposition experiments. The result of this positioning is that the needle is as close to the irradiated region as possible without actually contacting the surface.

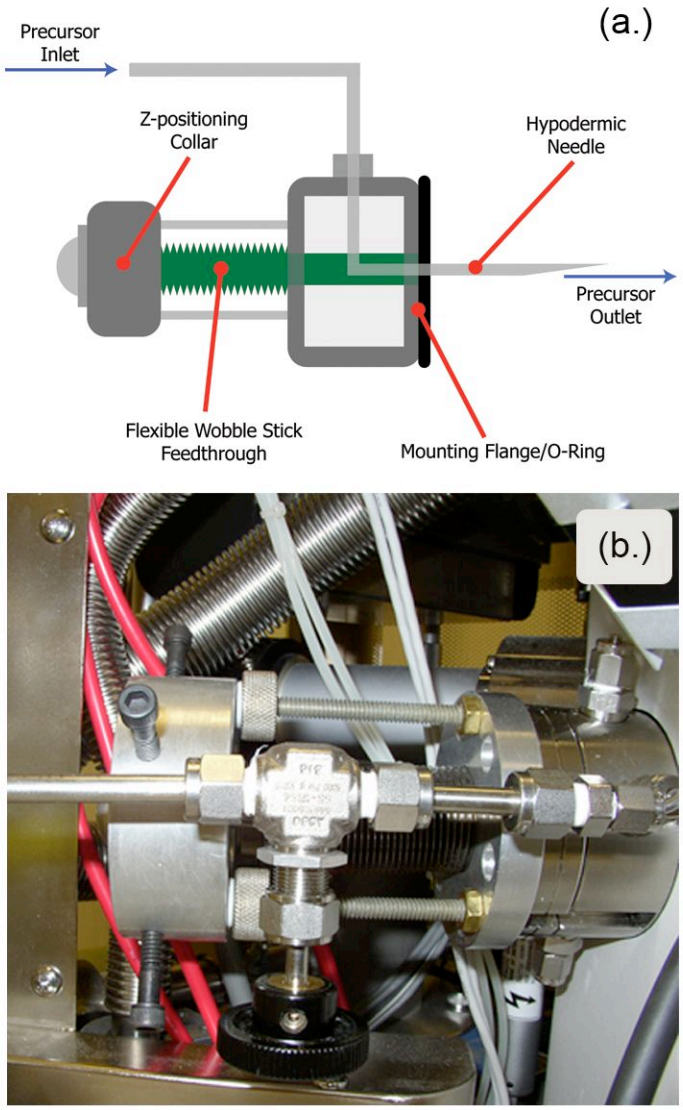

Figure 2-2: Vapor Injection System Details

Detailed (a.) illustration and (b.) digital photograph of the vapor injection system mounted on the Hitachi S-4300SE/N. The vapor injection system consists of a collar to maintain the z-position of the wobble stick, and a flexible feedthrough that allows the needle to be positioned off-axis as needed. Precursor vapor may be directionally applied to the point of interest by placing the hypodermic needle in the field of view of the SEM.

Chapter 3—Fundamentals of EBID: Thermal Limitations

3.1 Introduction and Motivation

The ongoing nanotechnology revolution is fueled by a desire to manipulate matter and energy on a size scale that falls into a "physical gray area" between classical and quantum physics. In this regime, the behavior of materials is not well understood as of yet, making predictability and repeatability of nanoscale experiments challenging. In addition, random and systematic experimental errors become increasingly critical at these small dimensions. For these reasons, nanofabrication process control is becoming increasingly important. Such is the case with EBID.

The ability to deposit nanoscale features with a high degree of precision and minimal substrate damage is the key attribute of EBID. However, one of the major drawbacks to using EBID is that, currently, process control is somewhat limited; this alone can offset any advantage that EBID has to offer. For the capabilities of EBID to be fully realized, a greater understanding of the fundamental mechanisms is necessary. Despite the numerous EBID studies reported in the literature, there is still only a limited understanding of the physical phenomena that dominate the EBID process. Therefore, there is strong motivation to determine how to achieve a greater level of process control, and increasing the fundamental understanding of the EBID process is a necessary step toward this end.

Perhaps the most critical aspect of EBID processing is obtaining optimum mass transport of precursor species to the substrate and ensuring efficient adsorption to the surface. Unfortunately, the energetic nature of EBID adds complexity to the problem beyond that of simple gas flow dynamics. The interaction of the beam with the surface results in energy deposition, which may subsequently affect the process in a variety of ways. One such effect is heat generation in the substrate or the deposited nanostructure. This generated heat can have a localized effect on the precursor adsorption properties, which may lead to unanticipated EBID results. For instance, several seemingly anomalous observations of EBID nanofiber growth have prompted speculation about the role of beam heating during deposition. However, comprehensive simulation and experimentation on these effects is lacking.

The purpose of this work is to provide an understanding of the role of beam heating during EBID and to help explain some of the common observations reported in the literature. The method by which these issues will be investigated utilizes a Monte Carlo simulation that is coupled with a finite element model (FEM) to simulate the local temperature rise that occurs when a nanostructure is irradiated by an electron beam. Additionally, correlation between simulated and experimental results will be made.

3.2 Background and Relevant Literature

As with any additive micro-/nanofabrication technique, one of the most critical EBID process characteristics is the deposition rate (and its repeatability). Since this is a

simple result to measure, much of the fundamental work in EBID has focused on the response of the deposition rate to changes in current density, beam energy, gas flux, etc. Among these studies, there is typically good qualitative agreement of results, especially for scanning mode experiments where the beam is rastered over an area or in a line as opposed to point mode operation.

Fujioka *et al*. have previously investigated the energy dependence of EBID. [66] They deposited iron (using an $Fe(CO)_5$ precursor) on a SiO_2 substrate in order to study the influence of primary beam energy on the deposition process in the energy regime of 1 keV to 15 keV. They determined that the deposition rate was higher at lower beam energy by scanning a 50 × 100 μm^2 area for 60 minutes. The flow rate of $Fe(CO)_5$ precursor vapor used for this study was $\sim 2\times10^{-2}$ $Pa\cdot l\cdot s^{-1}$ and the incident beam current was 5 nA. While not specifically discussed in the work of Fujioka *et al*., their result is consistent with an EBID model in which deposition is governed by the precursor reaction cross-section.

In order to understand these beam energy results, it is necessary to discuss the concept of a reaction cross-section. The probability of interaction of energetic particles with matter is sometimes described by the physical quantity known as a cross-section. There exist a wide variety of cross-sections used to describe many types of interactions. For some time, it has been assumed that neutral dissociation events dominate the EBID process.[63] However, it is reasonable to suggest that ionization events may also play a role in EBID. In general, ionization and dissociation cross-sections have similar functionality and shape[73,74], but may differ in magnitude, peak energy, and threshold energy.

Unfortunately, dissociation cross-sections are difficult to measure; therefore, ionization data is more readily available. As a result, mathematical combinations of dissociation and ionization data has been used to approximate the dissociation cross-section for the purpose of understanding the complex energy dependence of EBID.[64] Figure 3-1 is a plot of the normalized ionization cross-section[75] for sulfur hexafluoride, SF_6, which is included to illustrate the typical behavior of the cross-section energy dependence.

The response of the EBID deposition rate to changes in beam energy is actually a function of the reaction probability. To understand the beam energy results, it is therefore necessary to consider the relation between reaction probability per incident electron and the cross-section. The probability of dissociation (or other cross-section-governed physical processes) involves not only the cross-section, but also the surface coverage of the dissociating species and the electron distribution at the surface. There are several ways of defining this relationship including in integral form for continuum distributions of electron flux as given by Eq. (3.1),

$$Q = \frac{N}{n_{PE}} \int_{E_o}^{E_f} n(r,E)\sigma(E)dE \qquad \text{Eq. (3.1)}$$

where Q is the dissociation probability per incident electron, $n(r,E)$ is the energy- and spatially-dependent electron flux (current density), $\sigma(E)$ is the dissociation cross-section, N is the surface density of adsorbed precursor, and n_{PE} is the number of incident primary electrons.[76]

From Eq. (3.1), it is evident that in the most simplistic case of a uniform, monochromatic beam, the dissociation cross-section is proportional to the dissociation

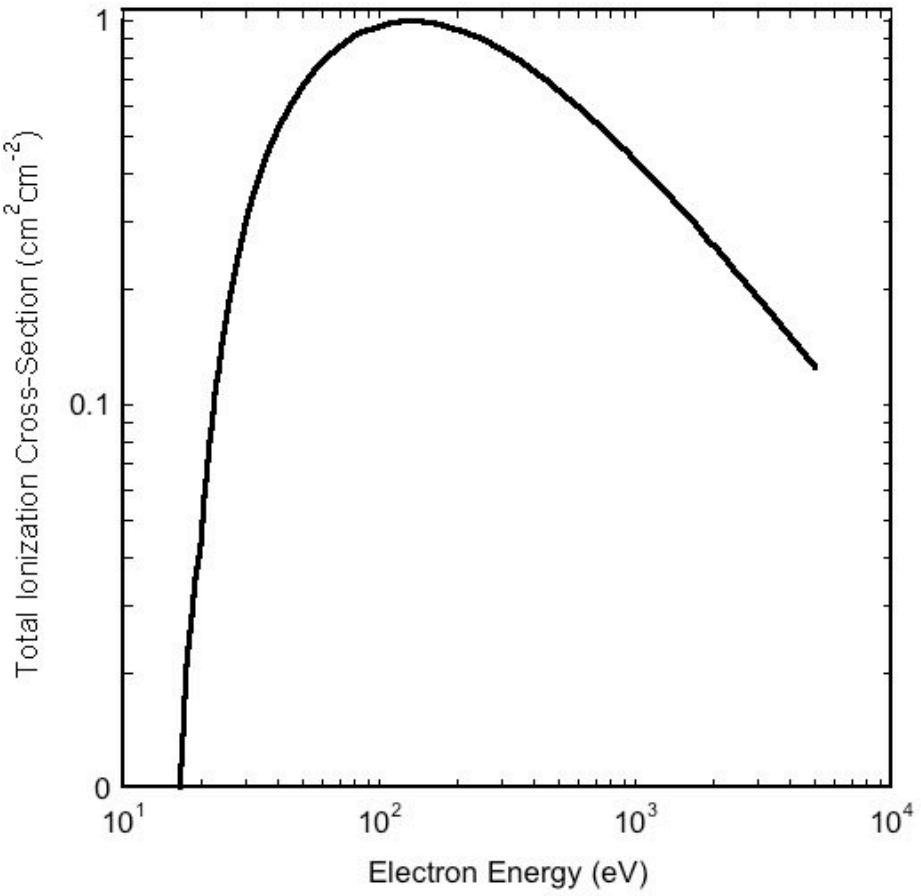

Figure 3-1: Normalized Ionization Cross-Section for SF_6

A normalized plot of the ionization cross-section[75] for SF_6 as a function of electron energy. Initially, the cross-section increases with energy up to a maximum at approximately 150 eV.

probability. This type of situation or a case where the current density distribution is nearly uniform could be responsible for the previously discussed[66] energy dependence observed by Fujioka. Based on the energy dependence of the ionization and dissociation cross-sections, it is therefore reasonable to suggest that the result obtained by Fujioka may be due to decreasing dissociation cross-section with increasing beam energy from 1 keV to 15 keV. Another possible contribution to the higher growth rate at lower energy is the higher secondary electron coefficient at lower beam energy. As described previously[64], the total deposition rate is a very complicated function of the energy distribution of all of the electrons.

While the results of beam energy experiments help to elucidate EBID mechanistic information, additional effects such as electron flux are also important. Beam current, electron dose, and deposition time play a vital role in EBID processing. In a series of scanning mode experiments, Hiroshima and Komuro deposited tungsten wires showing that the height increased with electron dose.[77] In these experiments, the beam current was maintained at 100 pA and the dose was controlled by increasing the time duration of the line scan. Similar results have been observed for tungsten deposition from $W(CO)_6$ in which the dose was increased by increasing the deposition time.[55]

As scanning mode experiments involve a dynamic beam raster, the EBID process is usually not in steady-state (except at long dwell times). While the preceding results can be explained by employing the current understanding of electron/adsorbate interactions, there are several EBID observations that are not easily understandable. In particular, ambiguous growth rate behavior is typically observed during point mode

deposition—a technique that is usually employed for nanofiber growth that represents the extreme case of steady-state EBID. Point mode EBID simply refers to a non-rastered electron beam, which is fixed on a single pixel. In the ideal case, deposition occurs only at the irradiated pixel, and the rate becomes limited by adsorption of precursor at the irradiated pixel at sufficient currents and typical localized pressures.

Common observations in point mode EBID nanofiber growth are that the deposit diameter increases for low energy and high current, in agreement with the increased beam diameter.[62] Other frequent observations are that the deposit height and diameter initially increase rapidly followed by a transition into lower growth rate regimes.[62] The two-regime growth behavior is illustrated in Figure 1-5 of Chapter 1.

The lateral broadening of the nanofiber base has been attributed to secondary electrons[63], backscattered and forwardscattered electrons[16], or all scattered electrons[64], but the temporal behavior of the vertical growth rate is not well understood. One potential phenomenon that could play a role in limiting EBID rates by reducing precursor availability is known as electron-stimulated desorption (ESD). ESD is the means by which incident electrons excite the bound species to a higher energy state. This additional energy supplied to the adsorbate may be manifested as higher vibrational, or kinetic energy and result in species desorption.[78] In this way, it is possible that ESD could result in lower surface concentrations of precursor in the area of irradiation, thus reducing the deposition rate. However, the continuous decrease in growth rate cannot be readily explained by an ESD-limited mechanism.

Other phenomena such as beam-induced thermal effects may control the seemingly anomalous results obtained for vertical fiber growth. Some of the existing literature implies that electron beam heating (EBH) may cause a reduction in the vertical growth rate for longer deposition times. For instance, Kohlmann-von Platen *et al*. suggest that a beam-induced surface temperature increase could be responsible for reducing the precursor sticking coefficient, thereby limiting the deposition rate.[62] Since ESD experiments are typically carried out with low power density (10^{-3}-10^{-5} W/cm^2) beams, thermal effects of electron irradiation can be considered negligible.[78] However, substantially higher power densities may be employed in EBID experiments, meaning that thermal effects may be significant and thus warrant investigation.

Crucial to the study of thermal effects on EBID is an understanding of vapor-solid adsorption/desorption kinetics. Several variables may be used to characterize the vapor-solid interaction, such as the sticking coefficient and residence time. The sticking coefficient is the fraction of impinging vapor atoms or molecules that adsorb to a surface, whereas the residence time is the average time an atom/molecule remains adsorbed before desorbing.[79] Both the sticking coefficient and residence time are dependent on the properties of the adsorbate and the surface, as well as surface temperature. Since the sticking coefficient and the residence time decrease with increasing temperature, it is reasonable to suggest that the deposition rate could be decreased due to EBH, assuming a mass-transport-limited EBID reaction.

When the equilibrium case is considered, the kinetic theory of gases can be employed to describe adsorption-/desorption-related quantities in terms of the state of the

system. A particular mass-transport quantity of importance to EBID is the steady-state adsorbate surface population, n_a, given by Eq. (3.2),

$$n_a = \left[\frac{p}{\sqrt{2\pi MRT}}\right]\tau_0 e^{\Delta H_{des}/RT} \qquad \text{Eq. (3.2)}$$

where p is the pressure, M is the molecular mass of the precursor, R is the universal gas constant, τ_o is the inverse of the attempt frequency, and ΔH_{des} is the enthalpy of desorption.[80] According to this expression, the adsorbate surface density for a given system is a function of only two state variables—temperature and pressure—both of which may be readily controlled and measured. Therefore, in mass-transport-limited EBID, the deposition rate should indeed be highly dependent on pressure and temperature.

Whereas surface temperature and/or precursor pressure will almost certainly affect EBID rates, it is not known if typical beam conditions actually generate temperature rises high enough to impact the deposition rate. In order to determine the thermal effects of electron bombardment, it is necessary to either model or experimentally confirm the local temperature profile at the point of irradiation.

Various approaches have been taken to simulate and quantify EBH for bulk (i.e. large and flat) substrates. The most flexible and widely used method of quantification is by means of numerical analysis. Mirkarimi *et al*. used finite element modeling (FEM) to study electron beam-induced heating on a planar Mo/Si multilayer film.[81] This model utilized a mathematical function to describe the energy deposition profile as a function of the radial position, current, voltage and material parameters. They found that at high current density (2.2 MA/m^2), a 10 keV beam induced a surface temperature of 833 K.

However, private communications with the authors revealed that their commercial software package had mishandled the thermal conductivity data leading to an artificially high temperature (the actual temperature rise was on the order of 15 K). Hau-Riege *et al*. used FEM and determined that 10 keV electron beams could increase the surface temperature of a silicon/molybdenum multilayer approximately 420 K assuming a beam current of 160-200 nA.[82]

In addition to numerical techniques, analytical solutions to the heat equation have also been used to show that significant heating occurs on bulk silicon and silicon dioxide, as well.[83] The solutions indicated that 45-85 K temperature increases during quartz mask pattering are possible using a 30 A/cm^2, and 50 keV beam. For silicon irradiation, a 50 A/cm^2 and 100 keV beam could produce temperature rises from 0.4-48 K.

As well as simulation, experimental evidence of beam-induced heating has been reported by Chu *et al*.[84] In this study, a thermocouple device was fabricated on-chip and was used to determine the temperature rise of a photoresist under electron bombardment. Their measurements were carried out on microfabricated, nickel/gold, thin film thermocouples. They reported that a 70 K increase in surface temperature occurred for a 15 keV electron beam and a current density of 0.5 MA/m^2.

As previously stated, these studies have assumed planar surfaces under electron bombardment. To be directly applicable to EBID, it is also necessary to consider surface nanostructure and topology as well as bulk materials. Monte Carlo simulation of electron scattering in an EBID tip (or fiber) structure and the subsequent energy deposition has been investigated, but was not integrated into a thermal model.[85] Utke *et al*. used an

analytical approximation of the temperature rise at the nanofiber apex to estimate the local temperature rise of cobalt nanostructures. Based on this information, they concluded that the high cobalt compositions obtained for high beam currents was a result of thermal decomposition of the precursor at the tip.[86] These studies are instructive and their results suggest that the thermal response of nanostructures is quite different from bulk substrates. However, there is still a need for a more general and flexible model that simulates electron trajectories in a nanostructure and is capable of integration with a thermal predictor model.

3.3 Experimental Methods

The experimental work to be discussed in the following sections was focused on the use of a tetraethoxysilane (TEOS) precursor vapor to deposit SiO_x nanofibers. This precursor was chosen because the resultant SiO_x has a low thermal conductivity (approximated by the thermal conductivity of SiO_2) and should be more susceptible to beam-induced heating. Therefore, if EBH has an effect, it should be more pronounced than in the case of a good thermal conductor.

The nanofibers were deposited on a silicon substrate coated with a 2-μm layer of SiO_2 topped by a 500-nm sputtered tungsten film. The tungsten film was photolithographically patterned in order to easily locate the experimental region for post-deposition characterization. In order to deposit nanofiber structures, the SEM was operated in point analysis mode, which fixes the beam in a stationary position. Typically,

the main chamber ambient TEOS pressure was ~1.8×10^{-3} Pa during the deposition process. It has been estimated that the localized vapor flux is on the order of 100 times greater than that specified by the ambient pressure based on capillary flow equations[8] and our own simulations. Detailed discussions of experimental techniques and the SEM setup can be found in Chapter 2.

A study of thermal effects during EBID necessitated temperature-dependent measurements. These experiments were performed using an Emitech K25X Peltier Cooled Stage. The stage is comprised of a copper block through which circulated water (heated or cooled) flows. A feedthrough is mounted on the SEM allowing the water lines to run from outside of the SEM to the stage. The stage is capable of stable operation in a temperature range of 243 K to 348 K. Digital photographs of the hot/cold stage apparatus are shown in Figure 3-2.

3.4 Simulation Methods

A Monte Carlo-based electron trajectory simulation was developed in the MATLAB® computing environment. The code was based on a single-scattering electron interaction model as introduced by D.C. Joy.[87] In this model, electron-solid collisions are governed by the Rutherford screened cross-section, which is given in units of cm^2 by

$$\sigma_E = 5.21\times10^{-21}\frac{Z^2}{E^2}\frac{4\pi}{\alpha(1+\alpha)}\left(\frac{E+511}{E+1024}\right)^2 \qquad \text{Eq. (3.3)}$$

where Z is the substrate atomic number, E is the electron energy, and α is given by

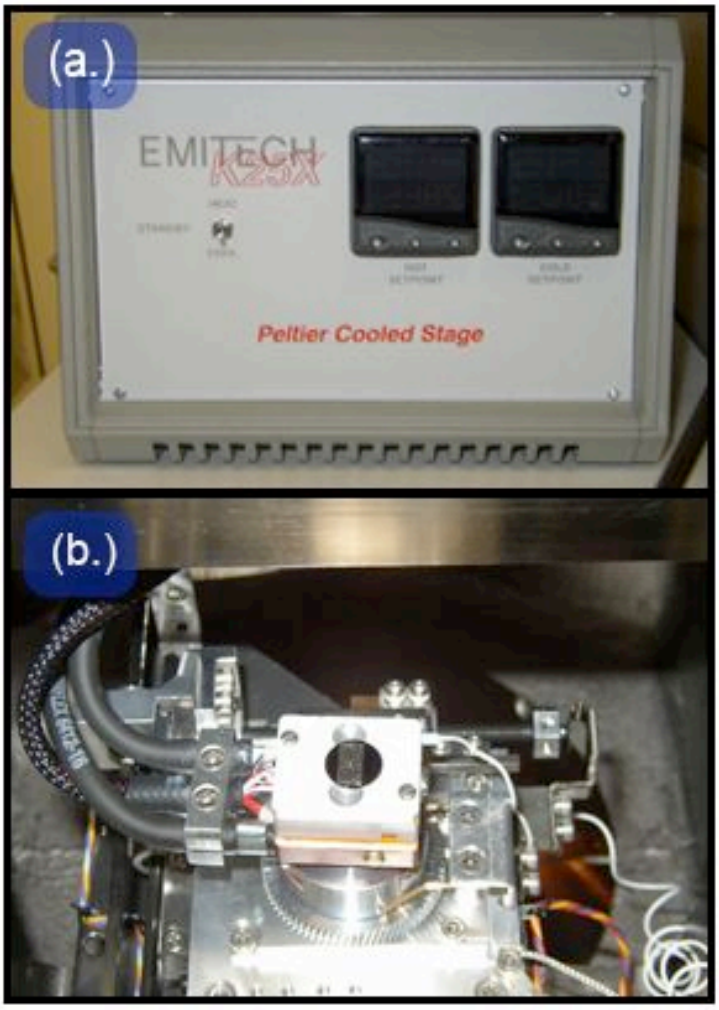

Figure 3-2: Peltier Cooled Stage

Digital photographs showing (a.) the control box for the Emitech K25X Peltier Cooled Stage and (b.) the stage as mounted in the SEM. Image (b.) shows the water lines entering and exiting the stage on the left side of the apparatus.

$$\alpha = 3.4\times10^{-3}\,\frac{Z^{0.67}}{E}. \qquad \text{Eq. (3.4)}$$

The amount of energy the electron loses when traversing a distance in the solid (keV/cm) is given in differential form by

$$\frac{dE}{dS} = -78500\,\frac{\rho Z}{AE}\log\left(\frac{1.166E}{J}+1\right) \qquad \text{Eq. (3.5)}$$

where S is distance, ρ is density, A is the atomic weight, and J is the mean ionization potential (keV), which is given by

$$J = \left(9.76Z + \frac{58.5}{Z^{0.19}}\right)10^{-3}. \qquad \text{Eq. (3.6)}$$

Each electron path is altered in direction by virtual collisions with the solid as it traverses the material. The direction and length of the post-collision path is a function of material parameters and electron energy, and is calculated for each collision. After calculating the scattering angles and path length for a collision, a series of geometric relationships may be applied in order the trace the trajectory in Cartesian space. A general algorithm for calculating the trajectories using the above equations and the aforementioned geometric relationships has been given by D.C. Joy.[87]

Given that the path of an electron in a solid is a function of the electron's energy, the single-scattering Monte Carlo (MCSS) simulation of electron trajectories inherently contains the energy deposition profile. Obtaining this energy deposition information is a matter of discretizing the spatial distribution of electrons and determining the amount of energy lost in a given volume element contained in the total volume. By storing the energy loss for each collision and its position, it is therefore possible calculate the

deposited energy density, which can be used to determine the temperature increase of the substrate.

For simplicity in calculation, the electron spatial and energy distributions were converted to cylindrical coordinates under the assumption of radial symmetry (no angular dependence). The spatial distribution of electrons was then discretized into a uniform grid of 3-nm units in the axial and radial directions. Figure 3-3 contains representative illustrations of the spatial discretization method used to calculate the energy density. The upper image of Figure 3-3 shows the radial symmetry about the *Z*-axis and the radial grid units (Δr). The lower image in Figure 3-3 shows an expanded view of an electron losing energy while passing through a grid segment. The energy lost by this electron, (ΔE), divided by the volume of the grid element yields the energy density (J/m^3). Summation of the total energy lost per volume element for multiple trajectories was then normalized to provide the energy density distribution on a per-electron basis. In this way, the distribution may be multiplied by the incident current to give the power density (W/m^3). The result of the simulation is a two-dimensional array of power density as a function of radial and axial position as given in cylindrical coordinates. The MATLAB® algorithm for the MCSS simulation and the energy density sort routine are included as Appendix A. This matrix of energy deposition data was then converted to a text format compatible with the FlexPDE® FEM software package, which is capable of accepting the data as input and using it as an energy source term in the heat equation, which is given by

$$\kappa\left(\frac{\partial^2 T}{\partial r^2}+\frac{1}{r}\frac{\partial T}{\partial r}+\frac{\partial^2 T}{\partial z^2}\right)+H(r,z)=0 \qquad \text{Eq. (3.7)}$$

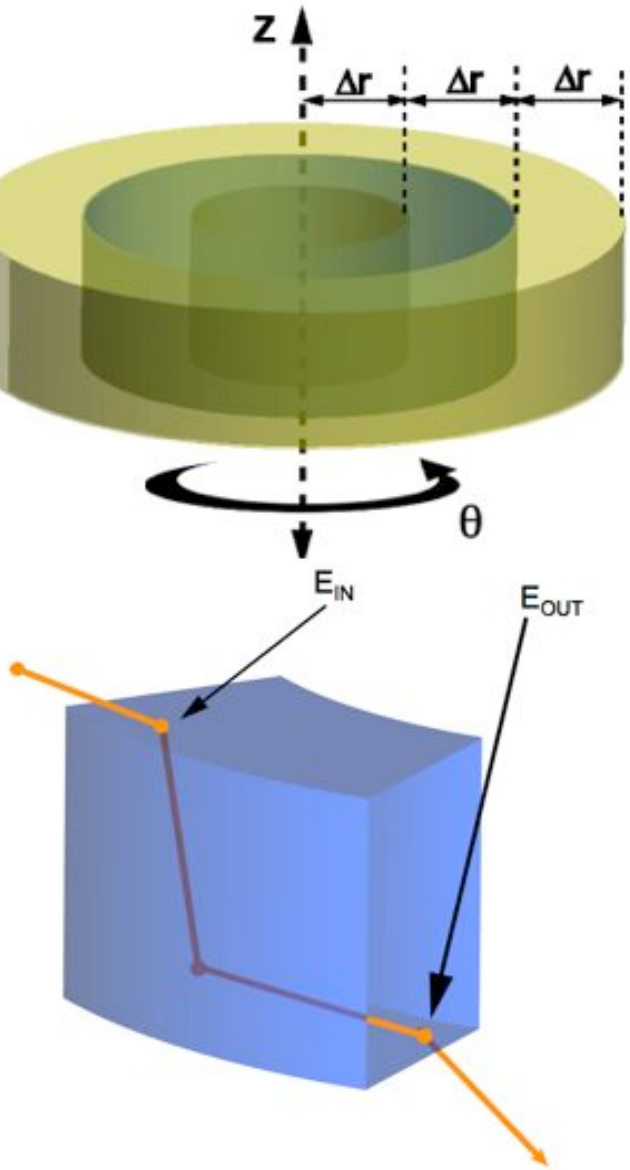

Figure 3-3: Illustration of the Electron Energy Distribution Discretization Method

Illustrations of the spatial discretization technique used to determine the power density of the irradiated nanofiber. Cylindrical symmetry was assumed, and the differential elements in the radial and axial positions were taken to be 3 nm in each direction. An energy balance over each volume element for each trajectory yields the energy density for a given volume element.

where κ is the thermal conductivity, r is the radial position, z is the axial position, $H(r,z)$ is the power density, and T is the absolute temperature. It is important to note that this is the steady-state form of the heat equation, in which there is no time dependence. The small size of the affected spot in the simulation ensures that the time to reach steady state is in the range of nanoseconds—a fact that was confirmed by earlier time-dependent simulations. Therefore, the solution of the steady-state heat equation employed in this work adequately mimics typical EBID experimental conditions where exposure times may vary from microseconds to minutes or longer.

The application of boundary conditions to a partial differential equation strongly affects the obtained solution. Therefore, the choice of boundary conditions is critical in determining the temperature profile of an irradiated nanofiber. Figure 3-4 is a cross-sectional illustration of the cylindrical models used to approximate experimental EBID geometries. The boundary condition for surfaces (1.) and (3.) as shown in Figure 3-4 was $\partial T/\partial z = 0$. The boundary condition applied to the symmetry axis, (6.), and the nanofiber radial boundary, (2.), was $\partial T/\partial r = 0$. The outer radial, (4.), and axial, (5.), boundaries of the substrate were assumed to be semi-infinite and constant at $T = 300$ K. The thermal conductivities of SiO_2 and tungsten used in the FEM simulation were 1.4 W/m/K and 174 W/m/K, respectively.

It is also important to note that the electrons used in the simulation were assumed to impinge at a point source at the center of the nanofiber tip. This is a reasonable approximation because the 3-nm grid radial dimension is on the order of the achievable beam diameter in the SEM. The use of a Gaussian-shaped spot is necessary only in the

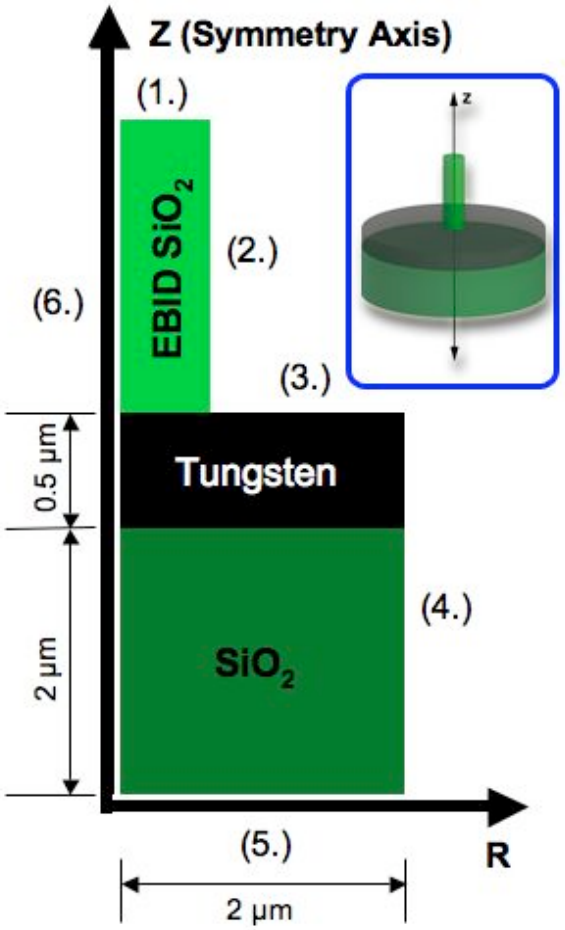

Figure 3-4: Simulated Nanofiber Geometry and Boundary Conditions

Illustration of the nanofiber geometry used in the Monte Carlo and FEM simulations. By symmetry, boundary condition (6.) was $\partial T/\partial r = 0$. Surfaces (1.), (2.), and (3.) are all Neumann boundary conditions with $\partial T/\partial z = 0$ for (1.) and (3.), and $\partial T/\partial r = 0$ for (2.). Dirichlet boundary conditions of T=300 K were applied to (4.) and (5.).

case of a large spot size (> 3 nm) or if a finer grid size is used. Therefore, the simulation may become inaccurate at the extremes of high current and low energy due to the large probe sizes inherent to these conditions. In order to precisely determine the magnitude of the temperature rise, it would be necessary to know the beam diameter and its functionality with condenser lens setting and beam energy.

3.5 Experimental Results and Analysis

Several experiments were performed in which silicon dioxide nanofibers were deposited from a TEOS precursor. Figure 3-5 is an electron micrograph of typical nanofiber structures that result from operation of the SEM in point analysis mode during EBID. Similar nanofibers were grown in a series of experiments in which the deposition time was varied in order to determine the transient behavior of the growth rate. This experiment was performed with a 20 keV electron beam, and beam currents of 107 pA and 530 pA. These results, which show an interesting transient behavior of the EBID vertical growth rate, are displayed in Figure 3-6. The data presented in Figure 3-6 shows that while the nanofiber height increases with time, the rate of the increase (as depicted by the Figure 3-6 inset plot) in height actually decays. Therefore, as the nanofiber becomes taller, the growth rate decreases and eventually the height saturates, which is in agreement with previous observations[62] of nanofiber growth. Another interesting result from Figure 3-6 is the observation that the initial and steady state vertical growth rates are higher for lower incident beam current. For instance, it can be seen at 10 minutes,

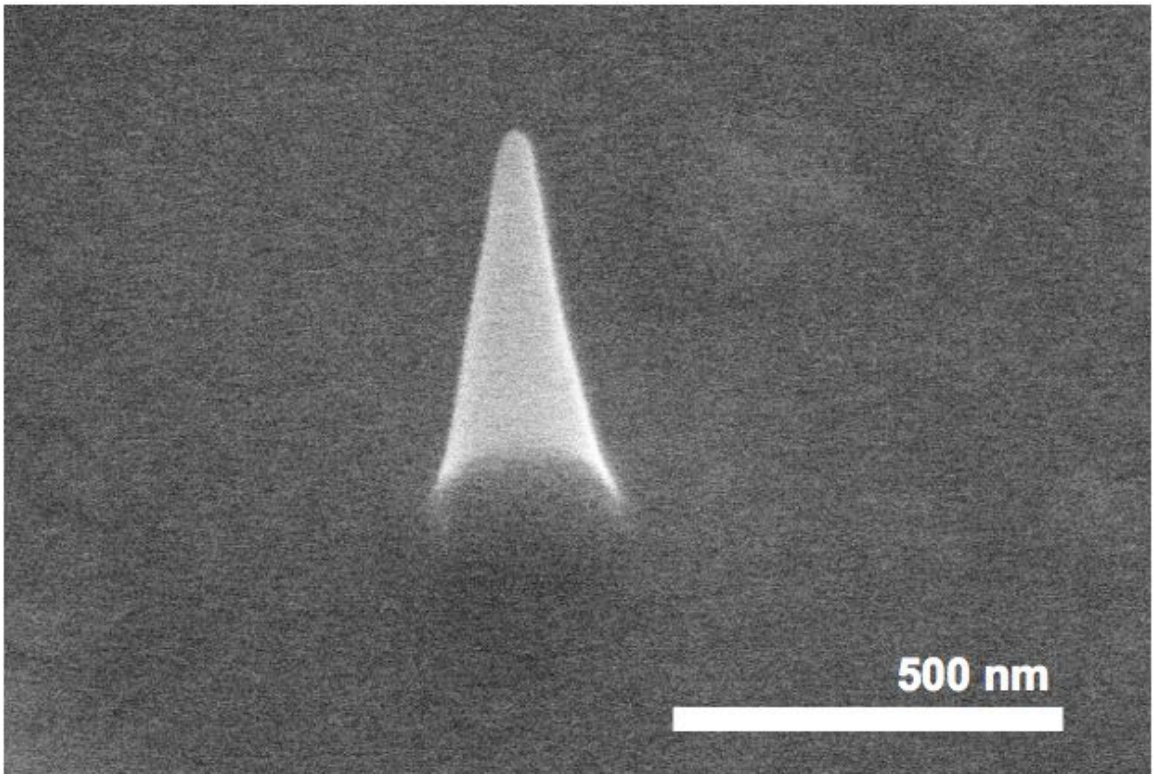

Figure 3-5: Electron Micrograph of EBID SiO_x Nanofiber

Scanning electron micrograph of a typical SiO_x nanofiber grown by EBID from a TEOS precursor.

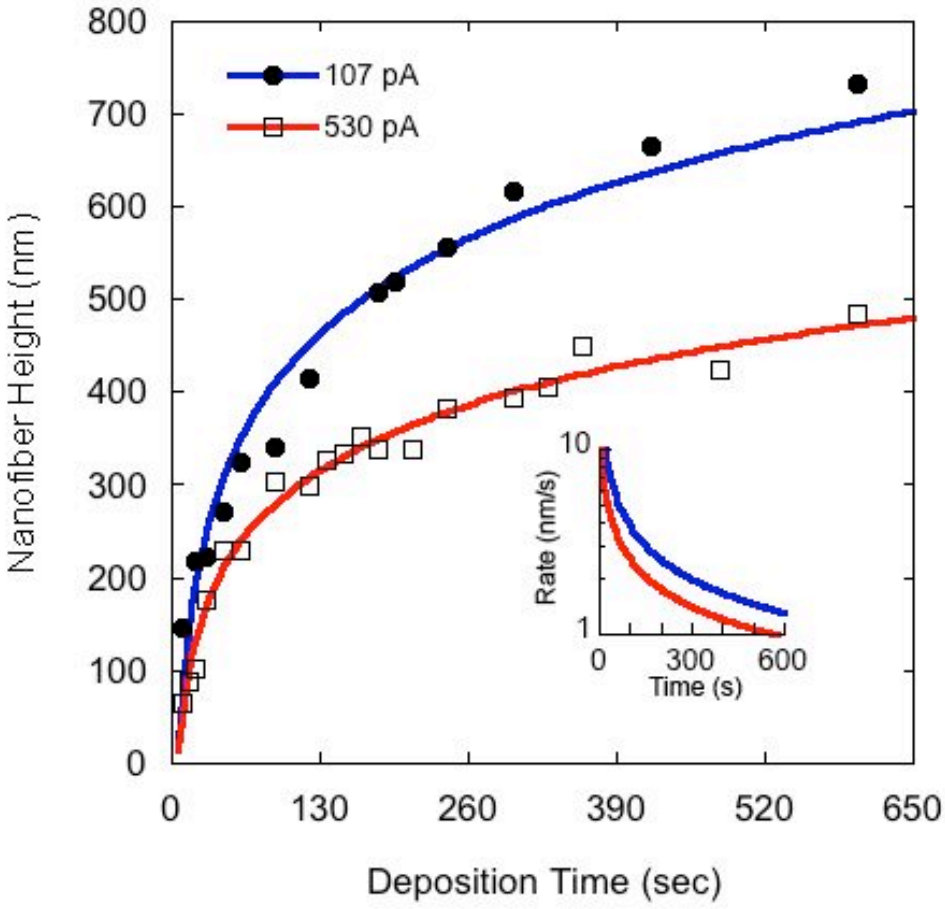

Figure 3-6: Time Dependence of the Growth Height of EBID SiO_x Nanofibers

Plot showing the time dependence of the height of nanofibers deposited by EBID. Higher beam current results in low vertical growth rates. The growth height is observed to saturate at long times. The inset figure is the data re-plotted as the average growth rate as a function of time.

a 107 pA beam current yields a ~750 nm-tall nanofiber, while at 530 pA the height is less than 500 nm. Figure 3-7 is a plot of the growth rate at 30 keV as a function of incident current that further shows the inverse relationship between growth rate and current. The response of the deposition rate to increased current is peculiar in that there are limited explanations for this behavior. In an electron-limited case, it would be expected that increased current would cause an increase in the deposition rate. At the other extreme of mass-transport limitation, it might be expected that an increase in current would have little or no effect on deposition rate. This result seems to suggest that electron- and mass-transport may be coupled through some beam-induced phenomenon, such as EBH. In such a case, a beam-induced reduction in the availability of adsorbed TEOS precursor could decrease the overall deposition rate. Increased current would result in higher energy density in the fiber, and would further reduce the precursor surface coverage.

Tedder *et al*. studied the surface population of TEOS interacting with a SiO_2 surface[88]and reported that at temperatures above 100 K, a large portion of the bound TEOS enters a physisorbed state, which reaches a maximum surface density at approximately 250 K. Molecular desorption of TEOS was found to be enhanced by increased surface temperature in the range of 250-450 K, above which decomposition from TEOS to siloxane species occurred. Therefore, if electron bombardment induces any surface temperature increase for room temperature experiments, it is expected that higher currents—which result in higher surface temperature—will in fact reduce the TEOS surface coverage and thus reduce the deposition rate. Therefore, the reduced deposition rate observed at higher beam current as shown in Figure 3-6 and Figure 3-7

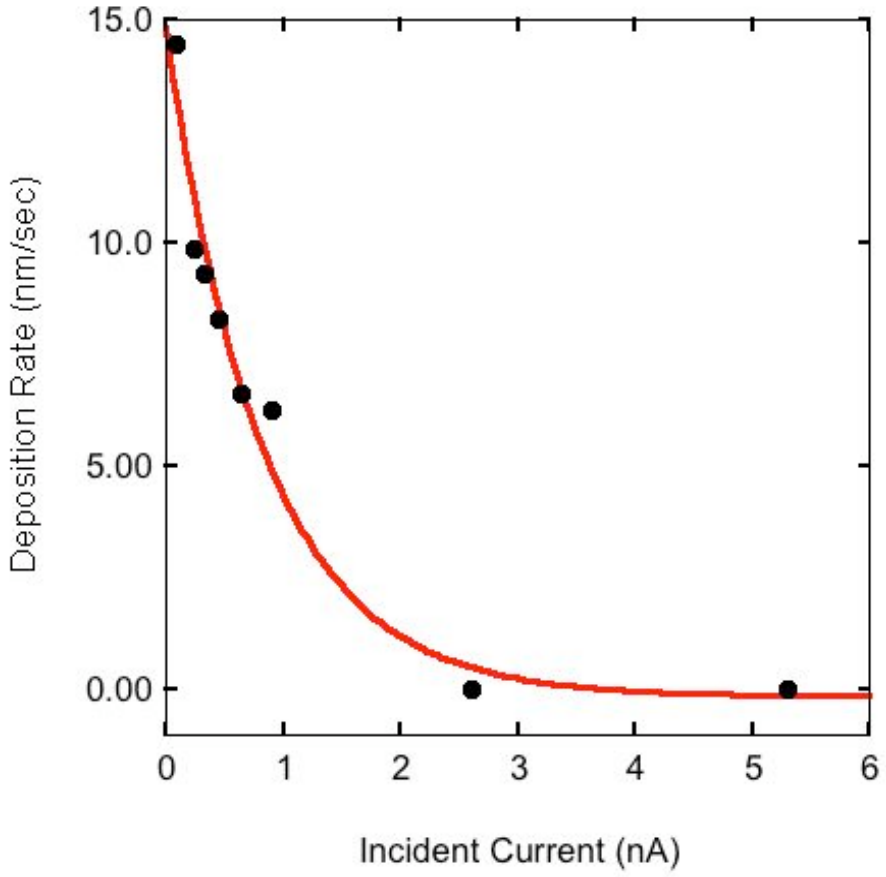

Figure 3-7: Current Dependence of the Growth Height of EBID SiO_x Nanofibers

Plot showing the time dependence of the deposition rate of nanofibers deposited by EBID. Higher beam current results in low vertical growth rates. The growth height is observed to saturate at long times.

is in agreement with the idea of EBH-limited TEOS surface population.

To experimentally verify that increased surface temperatures reduce the deposition rate, additional experiments investigating the effects of substrate temperature on the EBID process were performed. A hot/cold stage (Figure 3-2) was installed in the SEM in order to perform temperature dependent EBID growth experiments using the TEOS precursor. Deposition of SiO_x nanofibers was performed using 20 keV beam energy, 120-second deposition time, and a pressure of 1.7×10^{-3} Pa. The exact beam current was not specifically recorded as the hot/cold stage is not electrically connected to our metering port, but the condenser lens and aperture settings were consistent with a previously measured ~ 200 pA beam. For this experiment, deposition was performed in the temperature range of 295 K to 345 K. For each temperature adjustment, there was a necessary sample stabilization time of ~5 minutes in order for the specimen to reach thermal equilibrium after which no noticeable beam drift occurred. Figure 3-8 is an Arrhenius plot of the natural logarithm of the deposition rate versus the inverse of the substrate temperature. This plot illustrates that the growth rate is a strong function of substrate temperature and that higher rates occur at lower surface temperatures. This observation confirms that for these experimental conditions, the surface population of TEOS plays a limiting role in the deposition process.

From the Arrhenius plot in Figure 3-8, the measured activation energy of the process was determined to be ~ 0.23 eV. While the desorption energy for TEOS on SiO_2 was not reported in the work by Tedder *et al*., desorption energies typically vary from 0.15 eV for physisorbed species to 0.65 eV for weak chemisorption and physisorbed

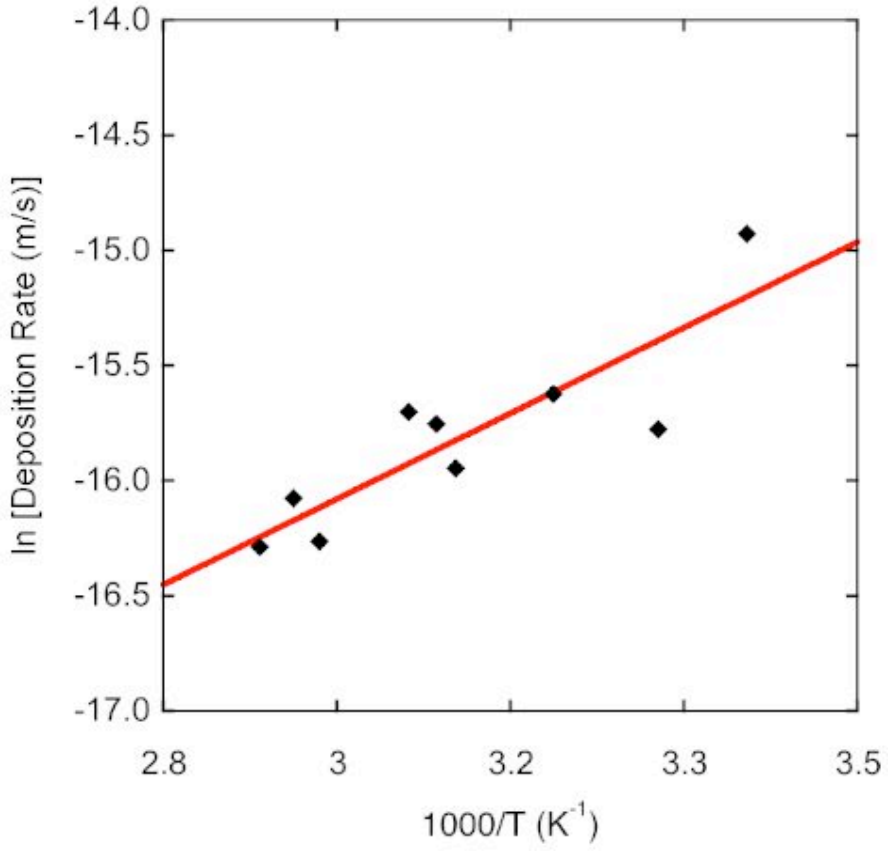

Figure 3-8: Temperature Dependence of the Vertical Nanofiber Growth Rate

An Arrhenius plot showing the temperature dependence of the vertical growth rate of EBID SiO_x nanofibers. The process showed an activation energy of ~ 0.23 eV, which is in agreement with the values for thermal desorption of similar molecules.

organic species.[26] Additionally, Wise *et al*. determined that the thermal activation barrier for deposition of SiO_2 from diethyldiethoxysilane (DEDEOS)—a species similar to TEOS that may also be used as a precursor for high pressure chemical vapor deposition (HPCVD) of SiO_2 deposition—was approximately 0.5 eV, and noted that this was similar to the reported value for TEOS.[89] These reported values provide indirect evidence that under the aforementioned experimental conditions, the surface population of TEOS controls the vertical deposition rate of SiO_2.

In addition to exposure time and beam current, the incident beam energy was also expected to play a significant role in the SiO_2 deposition process due to changes in reaction probability (as governed by the precursor vapor dissociation cross-section), the volume over which energy is deposited, and the secondary and the backscattered electron distributions and yields. The effects of beam energy were examined using 80-pA incident beam current, a 60 second deposition time, and an ambient chamber pressure of 1.8×10^{-3} Pa. Figure 3-9 depicts the results from this experiment and illustrates that the deposition rate increases with increased energy up to a maximum at 20 keV. Beyond 20 keV, an increase in energy decreased the deposition rate.

Since the dissociation cross-section decreases with increasing energy in this energy regime (greater than 3 keV), this result was not necessarily anticipated. In a process governed by the electron-mediated dissociation of TEOS, it would be expected that the deposition rate would continuously decrease with increased beam energy due to the reduced dissociation probability. However, the electron flux is also a factor in the dissociation probability. This presents the possibility that the observed current and beam

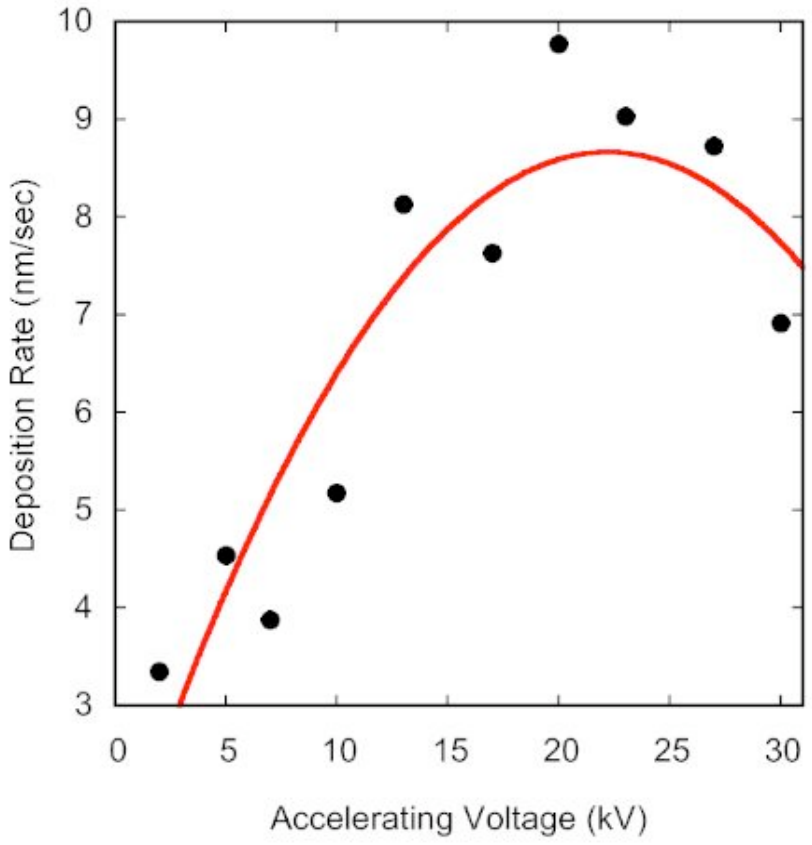

Figure 3-9: Beam Energy Dependence of Nanofiber Deposition Rate

Plot showing the effects of electron beam energy on the vertical deposition rate of EBID nanofibers. High deposition rates occur at higher energies, indicating that dissociation probability is unlikely rate-limiting.

energy effects are a product of smaller probe sizes, which lead to higher current density. While this is certainly true for the beam energy study, this is not the case with the beam current study. Private communications with Hitachi engineers have indicated that while increasing the beam current increases the spot size, the effect is not great enough to result in a net decrease in current density. Therefore, it is unlikely that the results presented in Figure 3-6 and Figure 3-9 are due to spot size effects. Again, this indicates that a phenomenon other than dissociation controls the deposition rate for the given experimental conditions.

To further illustrate the effects of beam current and energy, an additional set of time-dependent experiments were performed. Based on the previous observations, high current and low energy result in low nanofiber deposition rates. Thus, two sets of "opposite" conditions were used in order to further validate this observation. The results of the experiments are plotted in Figure 3-10 and clearly show the stark difference in growth rates while still maintaining the saturation behavior as shown in Figure 3-6.

Since it was previously shown (Figure 3-8) that in this pressure-current regime, the surface population of TEOS controls the deposition rate, the lower beam energies and high beam currents must lead to a reduction in precursor surface coverage in some manner, thus limiting the deposition rate. While this result is not fully understood, it may be partially explained by simulating the effects of EBH as a function of beam energy.

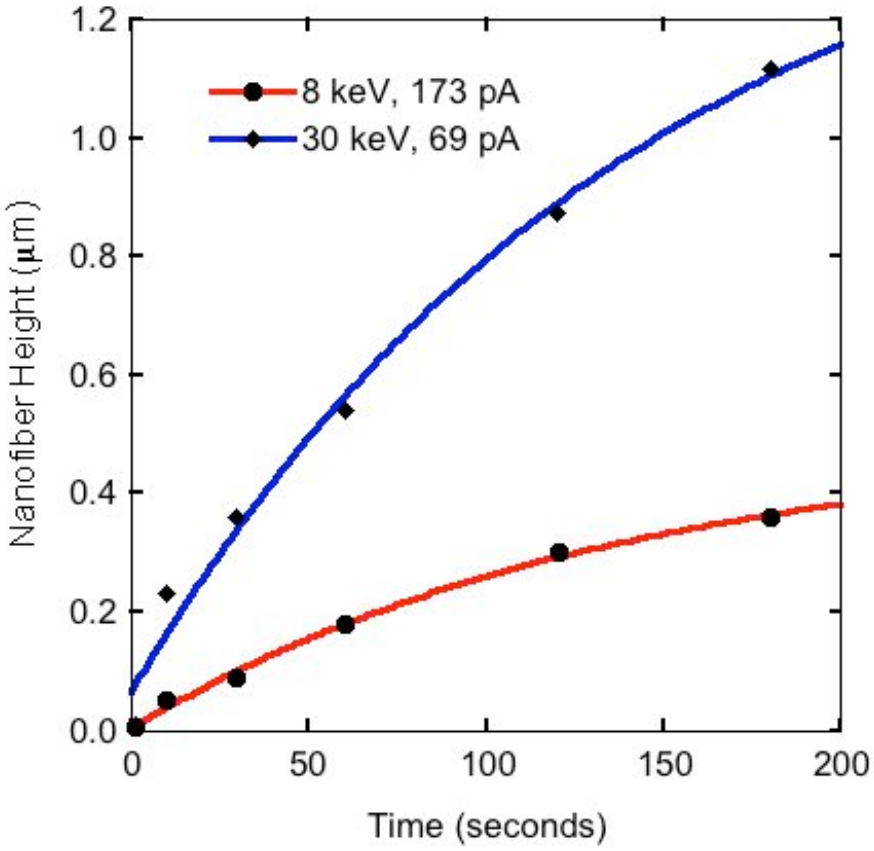

Figure 3-10: Combined Effect of Beam Energy and Current

Plot showing the effects of electron beam energy on the vertical deposition rate of EBID nanofibers. High deposition rates occur at higher energies, indicating that dissociation probability is unlikely rate-limiting.

3.6 Simulation Results and Analysis

Experimentally, it was found that increased surface temperature resulted in reduced deposition rates (Figure 3-8) due to reduced precursor coverage. In addition, the growth rate was shown to decrease at higher current, which may be due to higher nanofiber tip temperatures produced via EBH. In order to verify that the EBH can result in sufficient nanofiber tip heating to produce these results, a simulation was developed to determine the magnitude of EBH.

The initial simulations were used to investigate the effects of increased current on the nanofiber tip temperature. Since the magnitude of heat generation is proportional to the incident current, the change in nanofiber tip temperature, ΔT, for constant energy, radial position, and nanofiber geometry is linear with increased current. The results of a series of simulations are shown plotted in Figure 3-11. A 500 nm tall nanofiber with 100 nm diameter was used in the simulation with beam energy of 20 keV and variable beam current. Figure 3-11 shows that the tip temperature of the nanofiber increases linearly with increased current as expected. Therefore, the experimentally observed decrease in growth rate at high currents can be attributed to higher tip temperatures (lower surface population of precursor). For visualization purposes, Figure 3-12 is an example contour plot solution of the heat equation used to determine these and all subsequent temperature simulations. A 500 nm tall and 100 nm diameter nanofiber geometry was assumed for the simulation in Figure 3-12. The beam energy used was 1.5 keV, and the beam current was 500 pA.

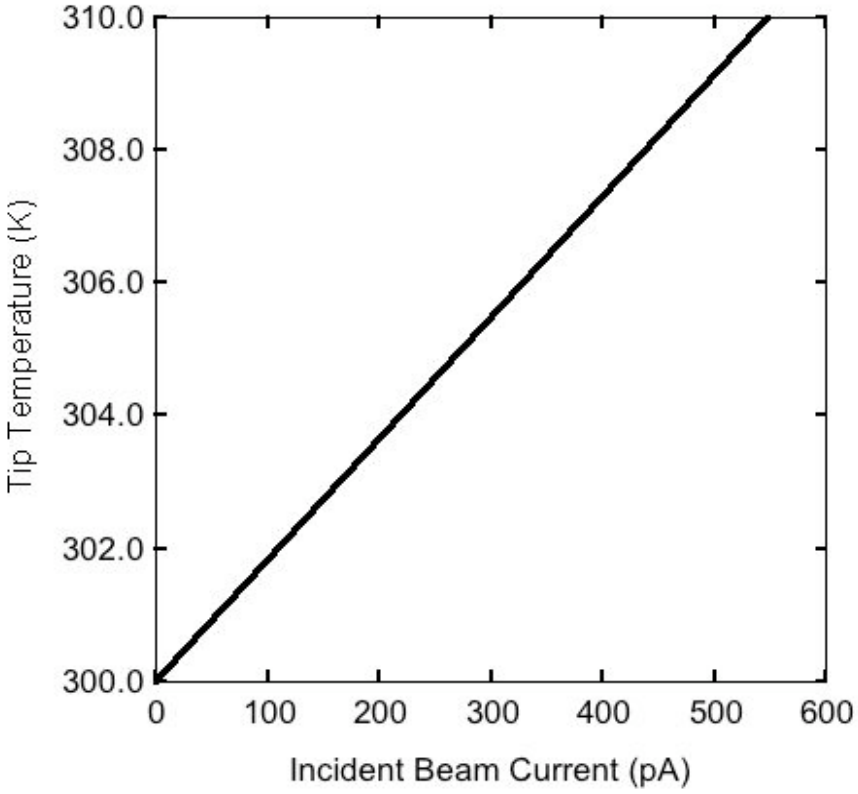

Figure 3-11: Simulated Nanofiber Temperature with Beam Current

Plot showing the simulated effects of incident beam current on the nanofiber tip temperature. The tip temperature increases linearly with beam current, which results in lower surface population of precursor, and subsequently reduces the deposition rate.

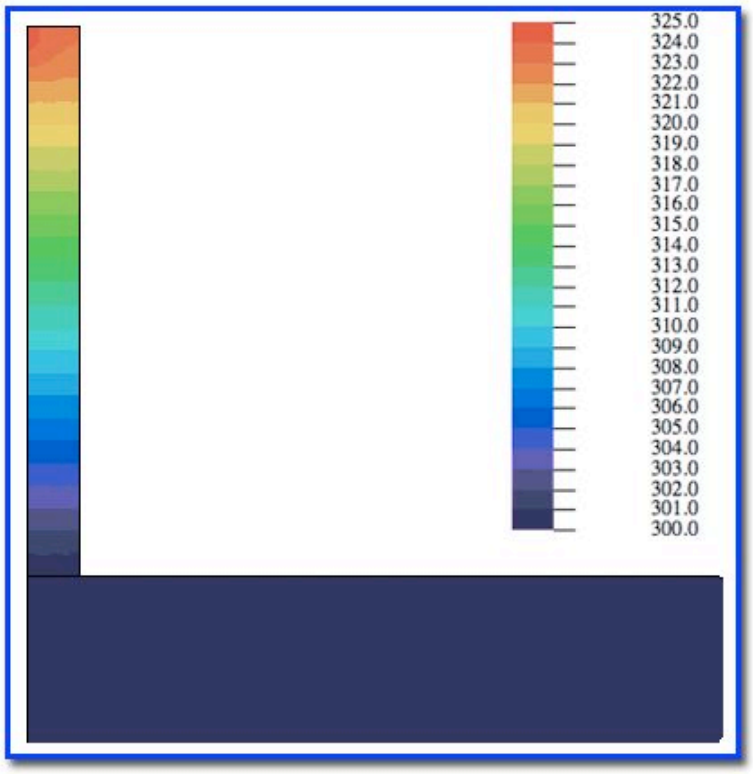

Figure 3-12: Simulated Temperature Contour of Irradiated Nanofiber

Contour plot showing the simulated temperature distribution of an irradiated nanofiber. The nanofiber was taken to be 500 nm tall and 100 nm in diameter. The beam energy used was 1.5 keV, and the beam current was 500 pA. The maximum temperature is observed at the tip of the nanofiber.

After determining the effects of beam current, the effects of beam energy on nanofiber tip temperature were simulated. The results of this simulation are shown in Figure 3-13. A beam current of 500 pA and variable beam energy were used for the simulation. In addition, in Figure 3-13, the differences between a SiO_2 thin film (500 nm thick) and a 500 nm tall nanofiber under electron bombardment are illustrated. In the simulation, the SiO_2 film was considered to be deposited on an effectively semi-infinite silicon layer, while the nanofiber was deposited on an effectively semi-infinite slab of tungsten on SiO_2 (used to mimic experimental conditions) as shown in Figure 3-4. Importantly, it was determined that the thermal conductivity of the semi-infinite substrate has very little effect on the nanofiber tip temperature as the heat generation is localized in the region of irradiation. In contrast, the thermal conductivity of the nanofiber has a profound effect on the steady-state nanofiber tip temperature.

For the thin film, the maximum surface temperature of 304 K is realized at 1 keV (the lowest energy simulated). As the energy is increased to 30 keV, the film surface temperature decreases to a value just slightly above room temperature. Higher temperatures are observed at low energy because of the inherent reduction in the electron interaction volume. While the total energy deposited by the low energy electrons is of course smaller, it is distributed over a much smaller volume. Consequently, the energy density and power density for low beam energies is much higher, and leads to higher localized temperatures in the case of irradiating a thin film.

Figure 3-13 shows that the temperature response of an irradiated nanofiber is, in many ways, quite different from that of the irradiated thin film. For the same incident

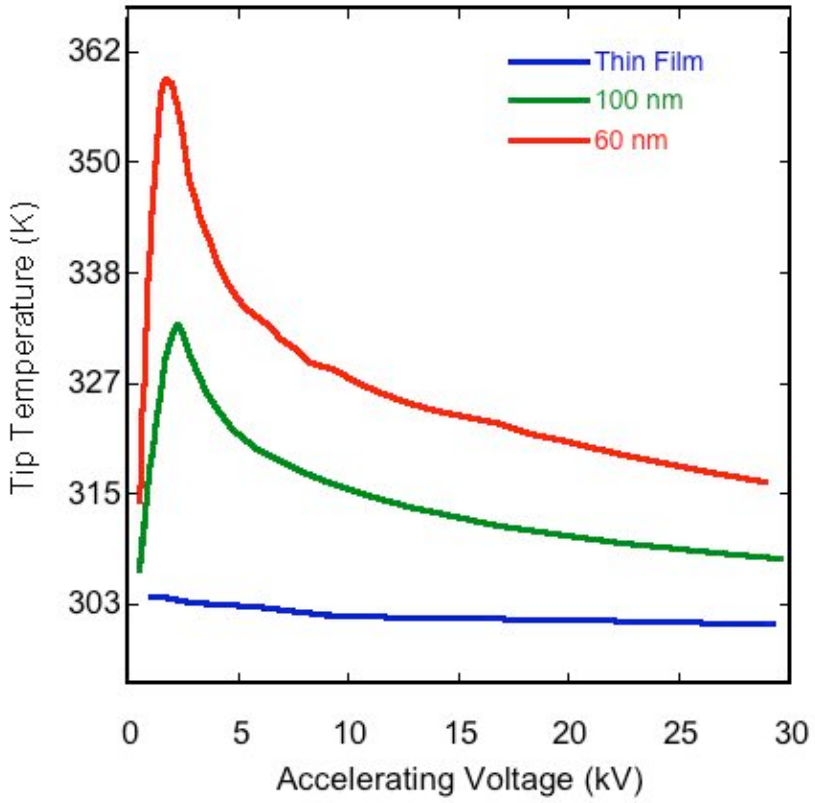

Figure 3-13: Simulated Nanofiber Temperature with Beam Energy

Plot showing the simulated effects of incident beam energy on the nanofiber tip temperature. Also shown is the temperature profile of a bulk substrate. The location of the energy source relative to the outer diameter of the nanofiber controls the maximum temperature increase for a given energy and nanofiber geometry.

current, the tip temperature of a nanofiber can be substantially higher than the surface of the thin film. This difference is due to the geometry of the nanofiber itself. Because the nanofiber is a raised feature, it represents the creation of a new surface with effectively insulating boundary conditions as shown in Figure 3-4 (convection and radiation through the vacuum is neglected in the thermal finite element model). In contrast to the thin film simulation, there exists only a narrow path for thermal diffusion, as heat must travel the length of the nanofiber before it can be dissipated into the bulk material. Therefore, the nanofiber effectively becomes a quasi one-dimensional structure in terms of heat conduction—an effect that results in increased tip temperatures relative to a flat surface. This one-dimensional heat conduction is responsible for the seemingly anomalous vertical growth rate behavior observed specifically in the growth of EBID nanofibers.

Upon further inspection of Figure 3-13, another noteworthy trend is observed to occur as a function of energy. In the nanofiber, the tip temperature initially increases in the low energy regime, reaches a maximum, and then steadily decreases with higher energy. This trend is due to the location of the energy source in relation to the nanofiber sidewall surface. At very low energy, the energy source is located well inside of the nanofiber boundary, so that the energy source is small compared to the volume of the nanofiber. In this case, there is semi-two-dimensional heat conduction as there is space in the radial direction for heat to flow. As the energy increases, the energy deposition volume increases and approaches the insulating boundary, which leads to higher temperatures as the nanofiber approaches one-dimensional heat conduction.

As illustrated in Figure 3-13, smaller diameter nanofibers will have a tip temperature maximum at lower beam energies. As the energy (and interaction volume) is increased, the structure does not behave as one-dimensional until the beam interaction radius is comparable to the fiber radius. Beyond this maximum, the energy deposition decreases because a large portion of the electrons are scattered out of the nanofiber and the resultant loss of energy yields lower nanofiber temperatures. Therefore, the tip temperature of a nanofiber is primarily dictated by the location of the energy source relative to the outer nanofiber boundary as well as the height of the nanofiber (as will be discussed later).

This effect is clearly observed in Figure 3-14 in which the power density at the near-tip region of the nanofiber is plotted as a function of radial position. It can be seen that at the lowest energy (1.5 kV), the majority of the energy density is located inside of the nanofiber. At higher energies, the energy source spans the full radius, but because of scattering out of the fiber, significant energy is lost and the overall energy deposition rate decreases. Therefore, the power density at the insulated nanofiber boundary is the controlling factor in the magnitude of the temperature increase at the tip. In order to further demonstrate the effect of nanofiber diameter on the tip temperature, additional simulations with variable radius were performed. Figure 3-15 further demonstrates the effect of radius on the tip temperature for a 100 nm tall nanofiber with a 5 keV beam and 500 pA of incident beam current. Clearly, the tip temperature decays rapidly as the nanofiber diameter increases. In Figure 3-12, it can be seen from the isothermal contour that, except for the near-tip region, there is essentially no radial temperature gradient.

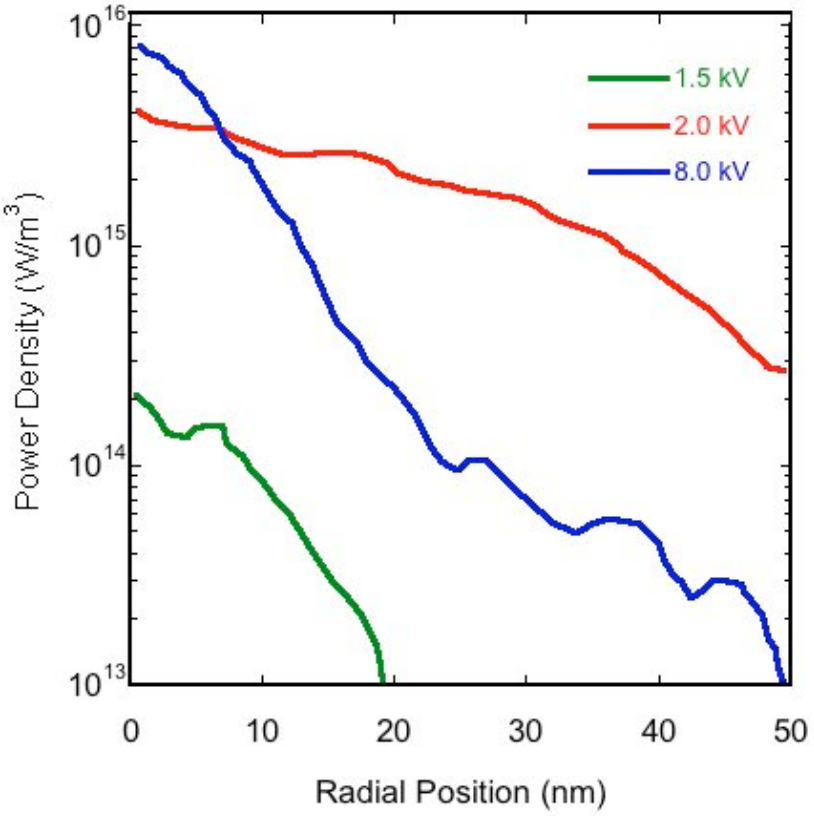

Figure 3-14: Simulated Power Density in the Nanofiber Near-Tip Region

Plot showing the simulated power density at the near-tip region of nanofibers as a function of nanofiber radial position. Low beam energies have a well-contained power density, while high beam energies result in high levels of scattering and lower power density at the nanofiber boundary.

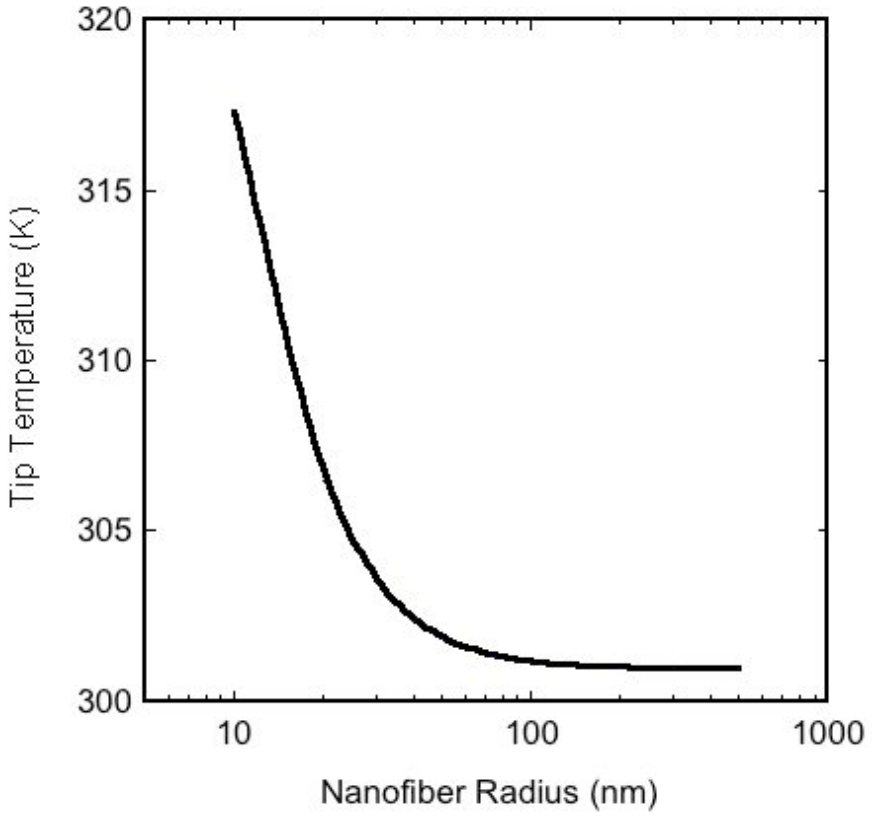

Figure 3-15: Simulated Effect of Nanofiber Radius on Tip Temperature

Plot showing the simulated tip temperature as a function of the nanofiber radius. For constant beam energy, beam current, and nanofiber height, increases in nanofiber radius result in lower tip temperatures.

Therefore, the nanofiber in Figure 3-12 is represents the case in which the structure is approaching quasi-one-dimensional heat flow. Again, this is in contrast to the bulk (or thin film) heating situation in which there exists a radial and axial temperature gradient. While the trends of the simulation at low energy are interesting, it is important to note that all of the experiments described in the previous section were carried out at 3 keV or higher energy. Therefore, the spike in nanofiber tip temperature shown in Figure 3-13 would not be reflected in any of the experimental data presented, as this phenomenon only occurs at these lower energies. Future experiments are planned to explore this region of beam energy.

Experimental evidence was presented that showed the nanofiber growth rate increasing up to a maximum at 20 keV as in Figure 3-9. According to the simulation results in Figure 3-13, the nanofiber tip temperature should decrease with increasing energy in the energy regime from 3 keV to 30 keV. It was observed that the deposition rate increased with increasing energy from 3 keV to 20 keV as in Figure 3-9. Therefore, this result is consistent with the correlation between high beam energy and low nanofiber temperatures from 3 keV to 20 keV, where the low growth rates at low energy can be attributed to reduced surface coverage of TEOS as induced by higher nanofiber tip temperatures.

While the model provides an adequate explanation of the observed energy dependence in the 3 keV-20 keV range, the turnover in growth rate from 20 keV to 30 keV as shown in Figure 3-9 cannot be explained by the EBH model. While further experiments are needed to confirm this behavior, it is possible that at these high energies,

the EBID process transitions to a process governed by the dissociation cross-section or electron flux, as opposed to the surface coverage of TEOS. As discussed in Section 3.1, the reaction probability is a complex function of the dissociation cross-section, electron energy-flux distribution, and the surface coverage. As any one of these parameters becomes dominant (either very small or very large), the reaction probability, and thus the deposition rate may transition to a different growth regime.

The EBH model describes relatively well the results of the previously described beam energy experiments and beam current experiments. However, the most compelling experimental observation is the temporal growth rate behavior for EBID nanofibers. As in Figure 3-6 and Figure 3-10, the growth height of nanofibers increases with time, but the growth rate actually decreases so that the nanofiber height approaches a saturation value. The simulations of tip temperature have already shown a strong geometric dependence as observed in Figure 3-13 and Figure 3-15, so the effect of nanofiber height on the tip temperature was also simulated.

To attempt to understand the time dependent growth rate behavior shown in Figure 3-6 and Figure 3-10, a 20 keV, 500-pA beam was used to simulate the tip temperature of a 100 nm diameter nanofiber with varying nanofiber height. Figure 3-16 shows that as the nanofiber height increases, the tip temperature increases sharply. Therefore, as the nanofiber grows, the surface population of TEOS is continually reduced, resulting in the reduced growth rates that are observed for long deposition times (or tall nanofibers) as in Figure 3-6 and Figure 3-10. As the energy source becomes further removed from the substrate (which acts as an infinite heat sink), the thermal

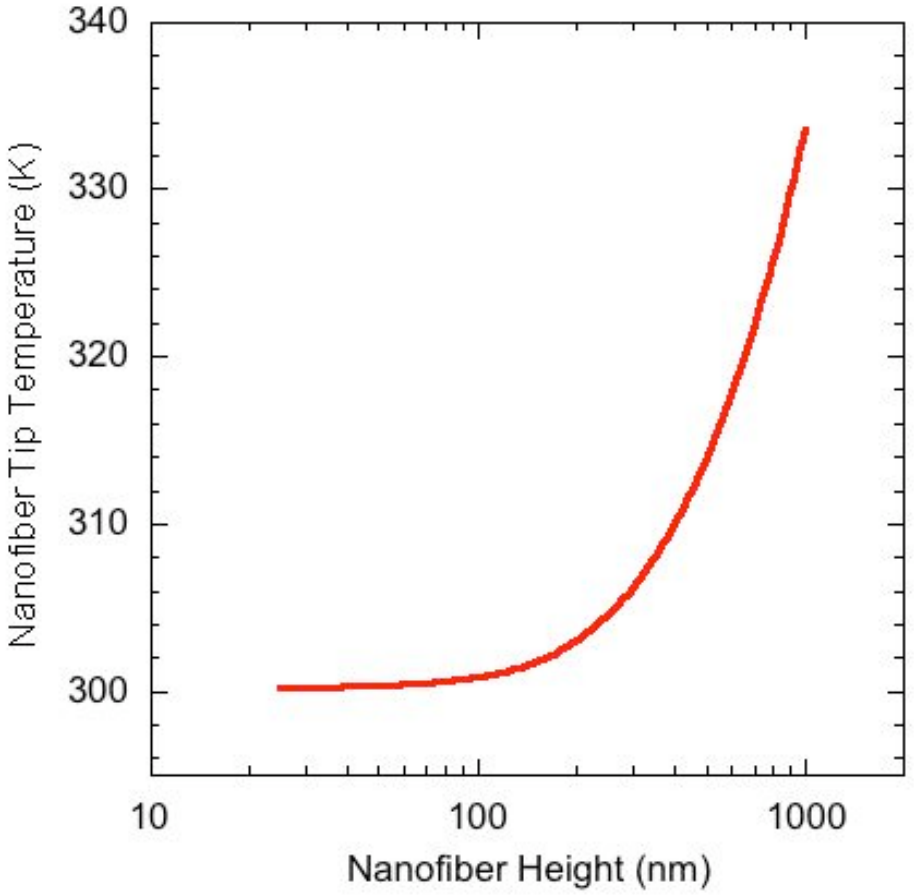

Figure 3-16: Simulated Effect of Nanofiber Height on Tip Temperature

Plot showing the simulated tip temperature as a function of the nanofiber height. A 20 keV, 500-pA beam was used to simulate the tip temperature of a 100 nm diameter nanofiber. As a nanofiber grows taller, the tip temperature increases, thus reducing the precursor surface population.

gradient is reduced, so that the rate of heat dissipation is continually decreased.

The results shown in Figure 3-16 can certainly be attributed to the above physical explanation, however, as the solution of a partial differential equation is significantly influenced by the boundary conditions, it was necessary to perform diagnostics to verify that the model did not produce erroneous results due to boundary condition placement. For instance, if the constant temperature Dirichlet boundary conditions given by surfaces (4) and (5) of Figure 3-4 were placed too close to the energy source, the boundary might become an artificial heat sink if the result of Figure 3-16 was not real. This could potentially result in simulation error due to the unrealistic boundary condition and artificially high thermal gradient that would result. In reality, a 1-cm^2 chip was used in experiments, but this dimension must be reduced for the FEM package to achieve adequate mesh density, as the nanofiber is orders of magnitude smaller. Therefore, it was necessary to place the boundary at a distance great enough to approximate an infinitely large substrate. This necessitated the use of diagnostic simulations to demonstrate the effect of boundary condition placement on the resulting solution.

A series of simulations was performed to confirm that the location of the constant 300 K boundaries, as shown in Figure 3-4, had no impact on the temperature profile solution, thus ensuring the simulated geometric effects shown in Figure 3-16 are indeed real. Figure 3-16 is a plot showing the tip temperature as a function of boundary condition placement. Also shown is the percent deviation in surface temperature from the value given by the 5000 nm placement that was used in all simulations. Movement of the boundary from 5000 nm to 1000 nm produced only a 0.5 K decrease in the tip

temperature, which validated that the temperature increase with height was not an artifact of the increasing distance between the energy source and these outer 300 K boundaries. Figure 3-17 is a plot of the diagnostic results, showing the minor effects of boundary condition placement. It is important to note that while there is a general slight increase in temperature as the boundary is moved away from the energy source, a continuous trend is not observed. The inflections in Figure 3-17 are within the predefined error limits of the simulation, which was set to be 10^{-3} K per node.

Figure 3-16 and Figure 3-17 show that taller nanofibers indeed result in higher tip temperatures, but the functionality of Figure 3-16 is not necessarily reflected in the observed temporal growth rate behavior. Figure 3-16 suggests that the nanofiber tip temperature continuously increases with increased height. If this were the case, it would be expected that the growth rate would also continuously decrease if limited by TEOS coverage. Figure 3-6 shows that there is not an experimentally observed continuous decrease in the deposition rate, but rather saturation to a steady-state value. We presume that the tip temperature and hence the TEOS coverage reach a steady-state value which leads to the observed steady-state deposition rate. The attainment of a steady-state tip temperature as opposed to a continuous increase with nanofiber height may be due to either the neglect of radiative heat losses (which are proportional to T^4) or convective heat losses that become significant at higher temperature. This behavior may also be partially attributed to the simplified nature of the cylindrical model of the nanofiber used in the simulation. Based on the sensitivity of the tip temperature to nanofiber geometry, it is anticipated that more rigorous models may be useful in resolving this discrepancy.

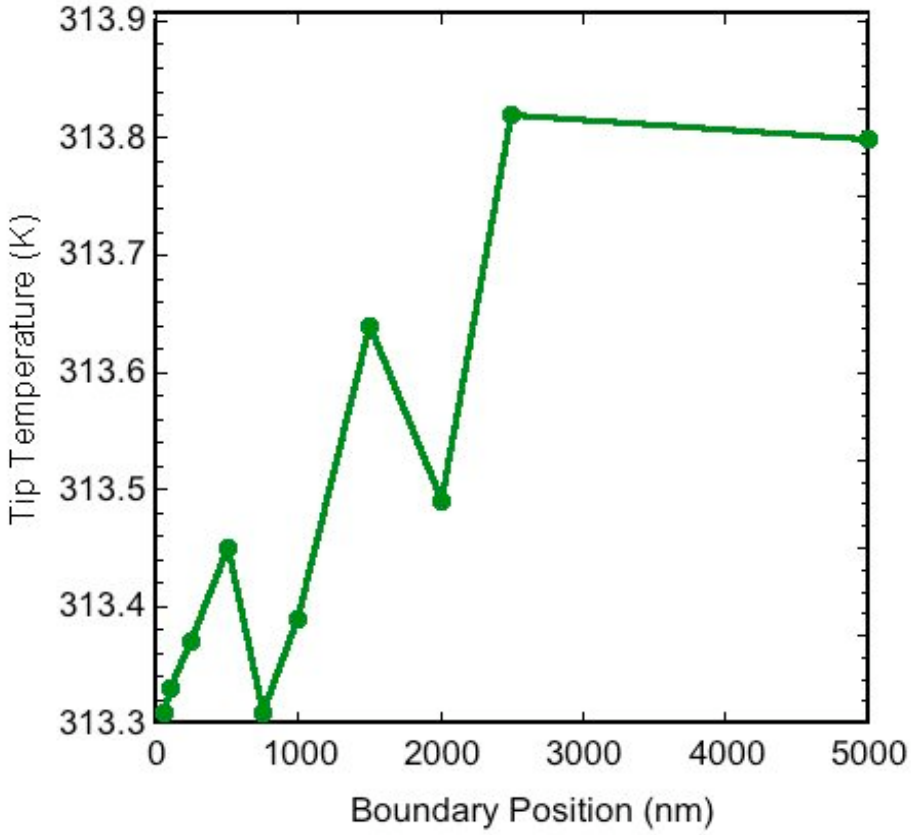

Figure 3-17: Simulated Boundary Condition Placement Diagnostic

Plot showing the simulated tip temperature as a function of the boundary condition placement for a 50 nm diameter, 100 nm tall nanofiber, with 5 keV beam energy, and 500 pA beam current. A 5000 nm change in the boundary condition placement relative to the energy source only results in a 0.5 K difference in the solution. Inflections in this plot are within the predefined error limits for the simulation (10^{-3} K).

3.7 Summary and Future Work

The phenomenon of electron beam heating (EBH) was used to explain several otherwise anomalous experimental observations associated with electron beam-induced deposition. It was shown that a reduction in surface coverage of TEOS as controlled by elevated substrate temperatures reduces the EBID deposition rate. A Monte Carlo electron-solid interaction model integrated with a finite element model was used to simulate the tip temperature of a nanofiber as a function of current, beam energy, and nanofiber geometry. For typical experimental conditions, the simulation suggests that the nanofiber tip temperature decreases with increasing beam energy. Simulation results suggest that the nanofiber tip temperature depends strongly on the position of the electron interaction volume relative the radius of the nanofiber, with the maximum temperature occurring when the interaction volume radius is equal to the nanofiber radius. It was also determined by simulation that the tip temperature increases as the nanofiber height increases. According to the model, typical experimental EBID conditions are capable of generating tip temperature increases of 30 K—a temperature that was shown experimentally capable of dramatically reducing the deposition rate. The reduced deposition rate of the nanofibers at longer times and higher currents was correlated with the increased nanofiber tip temperature inherent to these conditions. These conditions result in reduced surface coverage of the TEOS precursor, which limits the growth in a mass transport limited regime. The observed energy dependence of the deposition rate was partially correlated to thermal effects, but the turn-over in the growth rate at high-

energy is not consistent with this model and may be due to a transition to a reaction rate limited process.

Based on experimental observations and simulated results—low current, high energy, and short nanostructures are conducive to low temperature and high deposition rates. Fortunately, these conditions are also favorable for high resolution EBID processing. Therefore, the thermal effects should only be significant when depositing high aspect ratio nanostructures. The strong geometric dependence of the temperature rise indicates that future EBH models should involve realistic physical representations, and future simulations of bulk heating by irradiation should incorporate surface roughness. In addition, radiative and convective heat losses should be taken into account in further EBH simulations.

Chapter 4—EBID Application Development: Direct-Write Lithography

4.1 Introduction and Motivation

The focus of the previous chapter was the study of some of the controlling mechanisms of EBID, while this chapter (and the following chapter) is dedicated to applying the some of the knowledge gained from these theoretical studies to further the application development of EBID. In particular, the goal of this chapter is to describe methods used to develop a direct-write lithography technique using EBID. The following paragraphs explain why such a technique is desirable and necessary.

For decades, mass production microfabrication technology has relied mainly on a process known as photolithography for defining and patterning features on a variety of materials in order to create semiconductor devices. Photolithography is a highly robust, and well-developed fabrication process with high wafer throughput. Photolithography is the process of creating patterns on a substrate by means of spatially selective irradiation of a photosensitive polymer coating, which masks the underlying material. Following the photochemical reaction, the resulting polymer film becomes differentially soluble in a solution known as developer. The tone of the photoresist determines which region becomes soluble; positive tone means that the irradiated region becomes soluble, whereas negative tone resists become insoluble after exposure.[90] A standard photolithographic process using both positive and negative tone resists is shown in Figure 4-1. The lithographic process in Figure 4-1 is followed by an etch process and

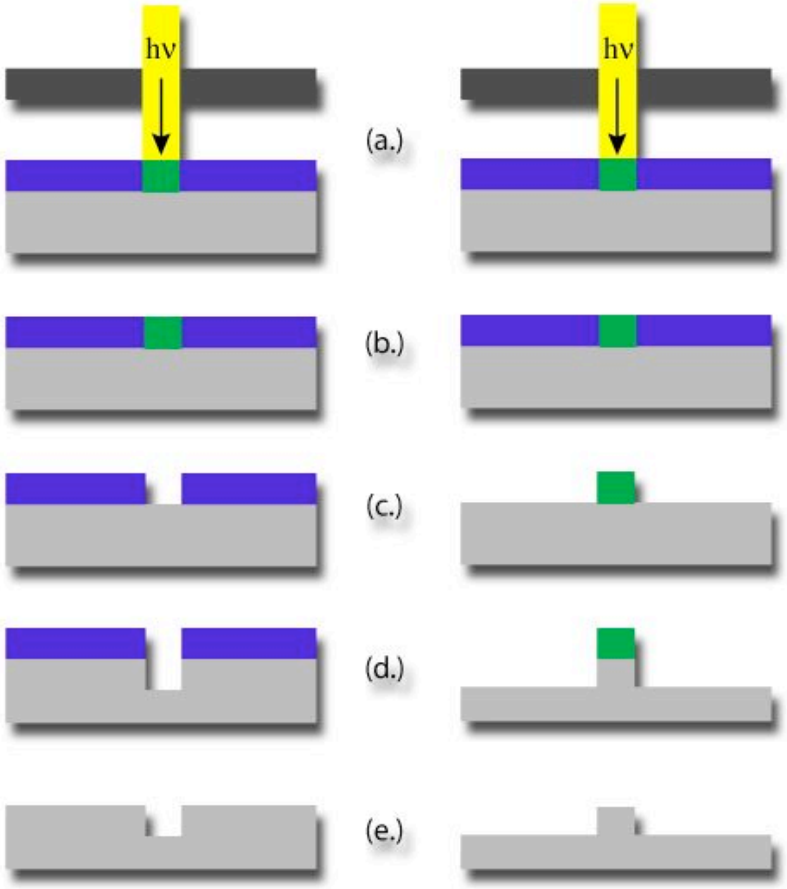

Figure 4-1: Photolithography Process Schematic

Standard photolithography using positive (left) and negative (right) tone resist involves (a.) irradiation of a photosensitive polymer through a photomask, (b.) creating differential solubility. The development solution dissolves the soluble polymer regions (c.), so that the cleared regions are susceptible to subsequent processing such as etching (d.). As a final step, the resist is removed following successful pattern transfer (e.).

resist removal in order to illustrate a simple pattern definition.

One of the primary disadvantages to standard photolithography is that the wave nature of light imposes resolution limitations. As the semiconductor industry moves forward according to Moore's Law[91] with increasing component density, standard photolithography is approaching its fundamental limit due to small feature size requirements. The feature size resolution is given by the diffraction-limited Rayleigh criterion, which is given as,

$$resolution = k_1 \frac{\lambda}{NA} \qquad \text{Eq. (4.1)}$$

where k_1 is a resist-dependent parameter, λ is the light wavelength, and NA is the numerical aperture of the lens system.[92] The current 90 nm node uses a 193 nm wavelength exposure, which is already pushing the limit for this exposure wavelength. Smaller feature sizes require advanced lithography solutions, which are addressed in the following section.

4.2 Background and Relevant Literature

The high throughput capability of photolithography has given the technique extraordinary industrial longevity. The desire of maintaining this level of throughput has fueled optical lithography research in many directions, in hopes of extending the process into future generations of semiconductor devices. According to Eq. (4.1) one way of achieving better resolution is by decreasing the wavelength of incident light from the UV range to higher energies. What initially seems like a simple solution is complicated by

the fact that lithography systems must be designed for a specific wavelength. Complicating this is the fact that the depth of focus is proportional to λ/NA^2. The depth of focus significantly affects the process latitude. As a result, decreasing the wavelength and increasing the numerical aperture decreases the already stringent process latitude. Additionally, new photoresists are necessary, as UV resists may not respond appropriately to higher energy light. For instance, x-ray lithography uses shorter wavelength light than UV, and thus provides greater feature resolution. Typically, x-ray lithography systems have operated in the 4-10 Å wavelength range.[93] However, one of the main barriers to the proliferation of x-ray lithography is the limited availability of low-cost, high-intensity radiation sources.[94]

Another optical technique aimed at extending the usefulness of current photolithography systems utilizes a special mask known as a phase-shift mask (PSM) to improve resolution. As the resolution limit of a lithographic process is approached, diffraction results in loss of contrast in the patterned resist. PSM makes use of transparent mask regions of a fixed thickness, such that the transmitted light is shifted 180^o in phase. The intensity profile at the resist results in destructive interference between adjacent features, thereby increasing the contrast for high spatial density patterns.[94] While PSM technology is very promising for extending the life of optical lithography, the resolution enhancement is not without penalty. The additional step required for patterning the phase-shifting layer significantly increases the mask fabrication complexity. This additional complexity results in lower mask fabrication throughput and higher mask cost.[95]

The resolution of optical techniques can also be increased by increasing the numerical aperture of the lens system. Liquid immersion lithography takes advantage of this fact by immersing the lens and wafer in a high refractive index liquid, resulting in improved resolution by increasing the numerical aperture in Eq. (4.1). Immersion lithography offers substantial promise, but the technology is still in its infancy. Tremendous engineering challenges must be overcome before it will be available for mass production. Issues regarding resist-liquid interactions, liquid-lens interactions, liquid dispensing, and liquid removal must be addressed before the technique's viability can be truly evaluated.[95]

While great efforts are being put into extending optical lithography to its limits, other lithographic approaches are being investigated in parallel. Standard electron beam lithography (EBL) processes can already achieve the desired resolution for near future applications. EBL is capable of producing patterns with much higher resolution than UV optical lithography due to the nanometer-sized probes that can be formed with current electron optics. While EBL is capable of producing feature sizes on the order of what is required for the coming years, the technique is not likely to overtake optical lithography due to low throughput. In photolithography, single levels of patterns are defined by one flood exposure through a photomask as shown in Figure 4-1(a). With EBL, the same pattern would have to be scanned by a single electron source, which takes considerably longer. Therefore, as a matter of practicality, standard EBL is not truly an option for mass production. Even as EBL has throughput limitations, it is still an invaluable tool for nanofabrication. One of the main advantages of direct patterning is that expensive mask

sets are not required for pattern generation.[96] This alone makes exploration of maskless, direct-write lithography (MDL)-based technologies a worthwhile venture.

Perhaps the most common and highest resolution EBL positive-tone resist is polymethyl-methacrylate (PMMA). Excellent pattern definition is possible with PMMA, but one of its limitations is that it has little resistance to subsequent plasma processing.[97] As a result of this and other problems—such as loss of contrast due proximity effects from electron scattering in the resist—alternative MDL techniques have been developed. The complexity and speed of ion beam lithography is comparable to EBL, but proximity effects are mitigated by the use of massive ions as opposed to electrons. Ion bombardment, however, can result in substrate damage, which may be unacceptable in some cases.[97]

One potential solution to some of these problems facing MDL involves research into alternative resist schemes. Electron beam-induced pattern formation using alternative resist schemes has been shown by a variety of different methods. For instance, direct writing into a resist layer is essentially a one-step positive-tone exposure/develop process by which a pattern is selectively etched into the resist by an electron-induced reaction. Matsui has demonstrated direct PMMA pattern and develop by using a focused electron beam (FEB) in the presence of ClF_3 vapor to etch feature into the resist. Using this technique, an array of 500-nm-wide lines was patterned in PMMA, but was not transferred to the substrate.[98] Using an analogous direct-write technique, amorphous, hydrogenated carbon films were used as a resist material for etching underlying gold substrates. FEB-induced etching with oxygen was used to selectively

remove sub-micron lines in the carbon film. A subsequent wet etch was performed to transfer the pattern into the underlying gold film prior to carbon resist removal in an oxygen plasma.[99]

Electron-induced differential selectivity has also been successfully used as a MDL process. Most of the work in this type of direct-write patterning has been performed with SiO_2 films. It has long been known that electron irradiation can be used to modify the structure and composition of SiO_2 films.[100,101] This type of phenomenon was later exploited in order to perform direct-write patterning of SiO_2 films. Allen *et al*. described a process in which SiO_2 films were irradiated with a 1-10 keV electron beam, followed by a wet etch process. They showed that the etch rate of the irradiated region was higher than that of the unexposed portion, resulting in pattern formation in the oxide film.[102] Their later work focused on determining the mechanism by which the selectivity arises. The selectivity differences depended highly on the type of oxide—thermal oxide etch rates were increased by irradiation, while other oxide etch rates decreased with irradiation. The resulting selectivity differences gave rise to a positive-tone process for thermal oxide, and a negative-tone process for other oxides. These observations were partially correlated to a beam-induced change in density; irradiated thermal oxides were shown to have a lower density, while other oxides increased in density following electron bombardment.[103]

Self-assembled monolayers (SAMs) have also been investigated in electron-stimulated lithographic processes. Whidden and colleagues electron-irradiated a SAM of 10-decenoic acid on SiO_2 and found that the resultant cross-linking of the surface species

yielded enhanced oxide etch rates.[104] Therefore, this represented another positive-tone direct-write lithographic process for silicon dioxide.

Direct-write pattering of silicon has also been reported. A novel electron beam-based technique for selectively growing epitaxial silicon on sapphire was introduced by Sawada *et al*.[105] This process involved electron irradiation of the regions in which no epitaxial silicon growth was desired. Irradiation followed by a molecular beam epitaxy process showed that the electron beam did prohibit silicon growth, resulting in direct-write pattern definition. Additionally, Yasuda *et al*. reported selective deposition of silicon by electron irradiation of a $SiCl_4$-treated, thin SiO_2 film, where ESD of chlorine-species was found to locally enhance the silicon deposition rate.[106]

Although many of these MDL techniques are quite promising, there are some limitations. Many of the processes are material-specific, and as such cannot be broadly applied for the wide array of materials used in the semiconductor industry. Therefore, there is still a need for more generally applicable direct-write lithographic procedures. One such approach is to employ a massively parallel array of electron FE sources, thereby alleviating the inherent throughput limitations of EBL. This so-called Digital Electrostatically focused e-beam Array Lithography (DEAL) concept aims to use multiple electron sources, as opposed to standard, single-source EBL systems.[107] The low energy electrons used to perform lithography with DEAL devices[108] requires that ultra-thin alternative resist schemes be developed. Thin resists must be especially resistant to post-development processing, due to the small amount of material present.

EBID-based MDL ultra-thin resist schemes may potentially offer a more general approach to direct-write pattering, which may be especially useful for the DEAL concept. As discussed in previous chapters, EBID is a versatile direct-write deposition technique that can be used to deposit a variety of materials with nanoscale precision. These nanoscopic EBID deposits can then be used to shield underlying materials from subsequent processing, so that the direct-write material functions as a resist layer. In the case of post-EBID etching, the result is analogous to a negative resist scheme in which the exposed feature is protected from removal.

Such a process has been briefly reported by Kohlmann-von Platen *et al*. in 1992.[65] In this work, which focused on general tungsten EBID, tungsten lines were written on a photoresist by a 7 keV electron beam with 50 pA of incident current. The patterned substrate was then exposed to oxygen plasma in order to remove the unprotected photoresist. The resultant structure was a 500 nm linewidth photoresist etch mask that could potentially be used in subsequent processing.

The purpose of the remainder of this chapter is to present the results pertaining to the further development of EBID-based MDL techniques. Two MDL resist schemes employing EBID will be discussed—a bilayer process, and a single layer process. The single layer process uses the EBID layer as the only masking material, while the bilayer process utilizes a standard photoresist as an additional etch mask as previously[65] reported.

4.3 Experimental Methods

The general experimental parameters and techniques used for the following experiments are covered in Chapter 2. Therefore, this section only outlines the experimental details specific to this chapter such as choice of precursor, substrates, and SEM operating modes.

The single layer MDL experiments were performed using a precursor for SiO_x deposition by EBID. This material was chosen as the masking material for the bilayer process for a number of reasons. First, the precursor is widely available and relatively inexpensive. Secondly, experiments discussed in the previous chapter gave a solid theoretical foundation to understanding some of the controlling phenomena in SiO_x EBID, so that additional process development was unnecessary. Lastly, the ability to fine tune the etch selectivity of silicon dioxide and the ability to readily remove the material in an HF-based wet etch were instrumental in material selection. The specific precursor chosen was tetraethoxysilane (TEOS), which results in the formation of a SiO_x deposit in the presence of electron irradiation.

One of the most important experimental parameters that must be considered is the substrate material to be patterned. For the single layer MDL experiments, the substrate chosen was amorphous silicon (a-Si), due to its abundant industrial use. A 50 nm film of amorphous silicon was deposited on a SiO_2-coated silicon wafer by means of radio frequency magnetron sputtering. Sputtering conditions were 25-sccm argon, 25-mtorr-chamber pressure, 200 W rf power, and a substrate temperature of 773 K. The a-Si films

were photolithographically patterned and etched to allow for easy location of experimental sites.

The bilayer MDL process was developed using a combination of photoresist and EBID tungsten. Tungsten hexafluoride was used as the EBID precursor due to its high vapor pressure and its capacity to produce high purity tungsten deposits. In addition, the high etch resistance of tungsten to oxygen plasma ensures that minimal deposit material is required to mask the resist during development. Shipley SPR 955 CM-2.1 resist was spun at a variety of speeds (thicknesses) on bare silicon and photolithographically patterned to identify experimental sites.

Three different EBID deposit geometries were investigated—rectangular/square, nanofibers, and lines. These three geometries were created using standard operating modes in the Hitachi S-4300SE/N VPSEM. Point analysis mode was used to grow nanofibers, line scan mode was used to deposit lines, and area analysis mode was used to deposit squares and rectangles of variable size. As determined by the studies discussed in the previous chapter, the deposition rate is highly dependent upon the surface coverage of precursor. As a result, high precursor pressures were chosen for all MDL deposition experiments. The ambient chamber precursor pressure for all trials was maintained in the range of ~5 mPa to ~9 mPa, though the localized pressure is significantly higher based on the localized injection of the precursor species.

Post-deposition processing was carried out in a Trion Technologies Oracle fluorine-based etch chamber. The system is capable of reactive ion etching, as well as inductively coupled plasma (ICP) etching. A variety of etch gases were used in the

following experiments, including oxygen, CF_4, and SF_6.

4.4 Results and Analysis—Single Layer Process

Prior to presenting and discussing the experimental results and observations, it is important to conceptually demonstrate the ideal process flow of EBID-based MDL. Such a process should obviously use a direct-write EBID approach to patterning features. For the single layer case, the pattern is written directly to the substrate so that no intermediate transfer steps are necessary. Figure 4-2 is a process flow schematic of the single layer, negative-tone process that was developed in this work. Initially, a feature is patterned on a substrate by EBID (Figure 4-2a) resulting in a direct-write etch mask (Figure 4-2b). The deposit is then used to mask the underlying material during a plasma etch, resulting in the desired pattern being transferred to the substrate (Figure 4-2c). The final step is a removal of the deposited masking layer (Figure 4-2d).

The goal of single layer EBID MDL is to deposit ultra-thin, nanoscale etch mask features. The thin etch mask requires high selectivity during the etch process; otherwise, the feature geometry may be significantly altered during etching. This could become critical at longer etch times where the etch mask could sustain significantly more damage. Consequently, it was initially thought to be critical to develop anisotropic and highly selective plasma etching processes. Any amount of lateral etching could drastically compromise the size of the transferred pattern. Therefore, a series of experiments were performed on photolithographically patterned substrates in an attempt to obtain vertical

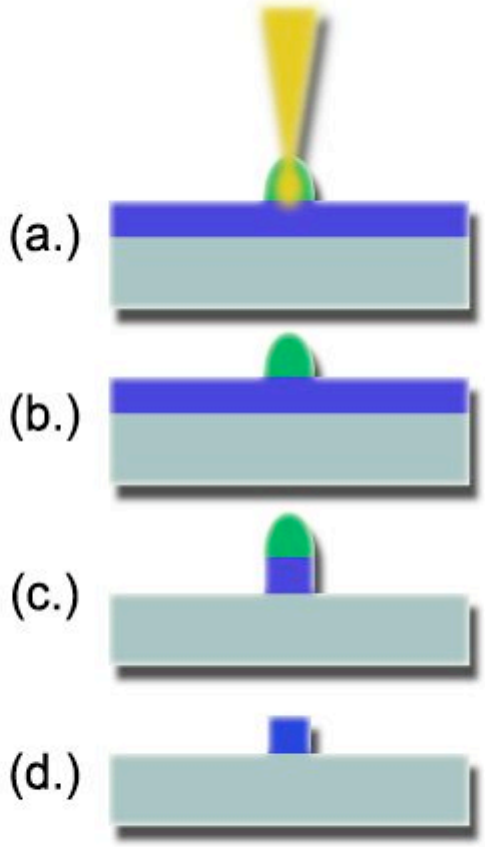

Figure 4-2: Single Layer EBID-Based MDL Process Flow Schematic

Process flow schematic for the single layer EBID MDL technique. The process involves (a.) EBID deposition resulting in (b.) a masking layer. The masking layer is used to protect the underlying substrate from a plasma etch (c.). Finally, the masking material is removed (d.).

etch profiles in a-Si films similar to those to be used in subsequent MDL experiments. The first process investigated was a standard RIE using a CF_4/O_2 plasma. The fraction of oxygen in a silicon reactive ion etch can be used to control the etch profile.[109] For this reason, the effects of CF_4/O_2 ratio on the a-Si etch profile were investigated. Figure 4-3 is a series of electron micrographs showing the silicon etch profile for four different flow ratios. The common conditions for etching were 150 mtorr, 150 W rf power, and three minutes etch duration. It can be seen from Figure 4-3b that the etch profile obtained for using a 25:1 CF_4/O_2 ratio produced the most desirable etch profile. While the profile was not vertical, this ratio produced the least variation from top to bottom, whereas all other flow ratios produced curved profiles. Therefore, the 25:1 CF_4/O_2 mixture was chosen for single layer MDL etch experiments.

Single layer MDL was carried out with standard EBID parameters as outlined previously by using point mode to pattern nanofibers, and line scan to pattern lines. Both SiO_x lines and nanofibers were deposited on an amorphous silicon film, followed by a CF_4/O_2 reactive ion etch (RIE). The conditions for the RIE were 150 mtorr, 150 W rf power, CF_4 flow rate of 75 sccm, and an oxygen flow rate of three sccm. The etch time was 15 seconds—intentionally short to minimize damage to the etch mask.

Figure 4-4 illustrates the before and after electron micrographs of the dot lithography nanofiber deposit and subsequent etch. The nanofiber was deposited with a 20 keV beam energy, 4 pA of incident beam current, for 60 seconds, and an ambient chamber pressure of 7 mPa. From comparison of two images shown in Figure 4-4, it is evident that the EBID nanofibers did provide a mask for the underlying a-Si film. The

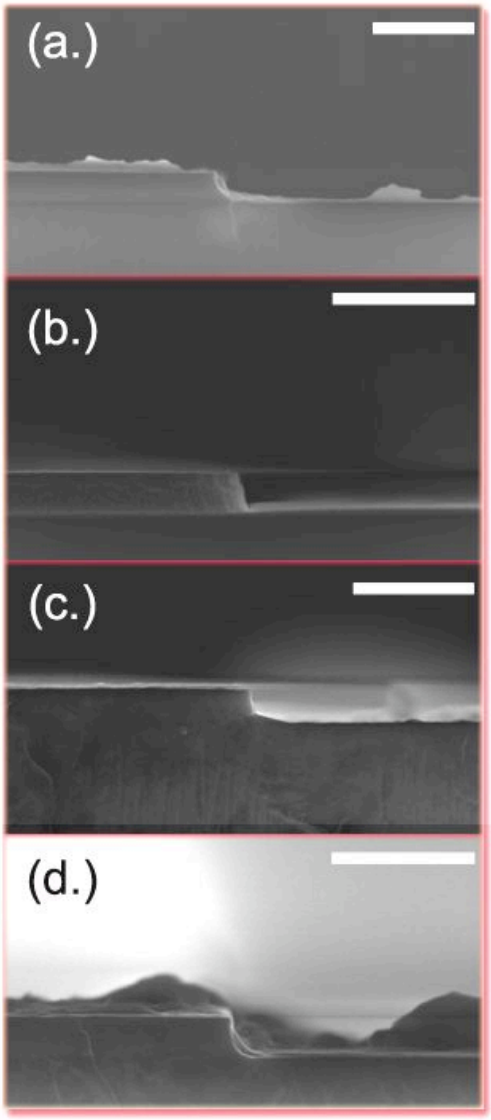

Figure 4-3: Silicon RIE Profile Control Experiments

Electron micrographs showing the effect of CF_4/O_2 ratio on the etch profile of amorphous silicon thin films. The ratios used were (a.) 75:1, (b.) 25:1, (c.) 15:1, and (d.) 7.5:1. The scale bars are one micron in length.

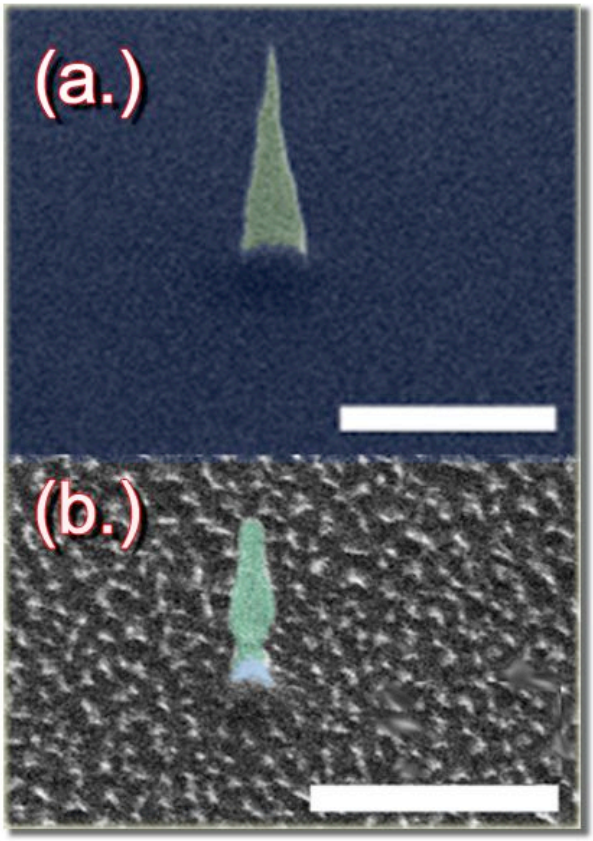

Figure 4-4: Electron Micrograph—Single Layer Dot Lithography

An electron micrograph of (a.) before, and (b.) after of the single layer lithography process for patterning dots by using EBID SiO_x nanofibers as an etch mask. The scale bars are one micron in length. Images were color modified to aid visualization. SiO_x is tinted green, while a-Si is tinted blue.

result of the process is a patterned a-Si dot of ~ 200 nm in diameter, which is represented by the blue-tinted region of the electron micrograph of Figure 4-4b. However, it is also clear that the geometry of the deposit was substantially altered by RIE damage to the etch mask. Comparison of the nanofiber base before and after etch images shows that the etch mask was undercut at the a-Si/SiO_x interface.

The results of the line scan single layer process are shown in Figure 4-5. The same deposition conditions were used as in Figure 4-4 with the exception of the scanning mode. The scan rate chosen was ~32 frames/second. The high frame rate scans in the Hitachi SEM include a "settle time" where the beam rests on the first pixel after each frame. As a result, the first pixel receives a much higher dose that the remainder of the line and an EBID nanofiber forms at this position (Figure 4-5). As the frame rate decreases, the settle time approaches the dwell time so that there is little disparity between pixels, and a uniform line (without nanofiber) is deposited.

From Figure 4-5, the same etch mask degradation is observed for the line scan as seen in Figure 4-4. The initial linewidth of ~ 200 nm was reduced to ~ 140 nm after the etch process. While not investigated in this study, this reduction in linewidth may be advantageous if properly controlled. A standard "trimming" process could be used prior to pattern transfer to reduce the feature sizes to the desired geometry. However, the pattern density is likely to remain limited by the initial etch mask size.

These single layer MDL results are promising and show proof of concept, but, unfortunately also represent the best observations. Initially, a significant amount of time was devoted to the development of an anisotropic silicon etch. Following several trials in

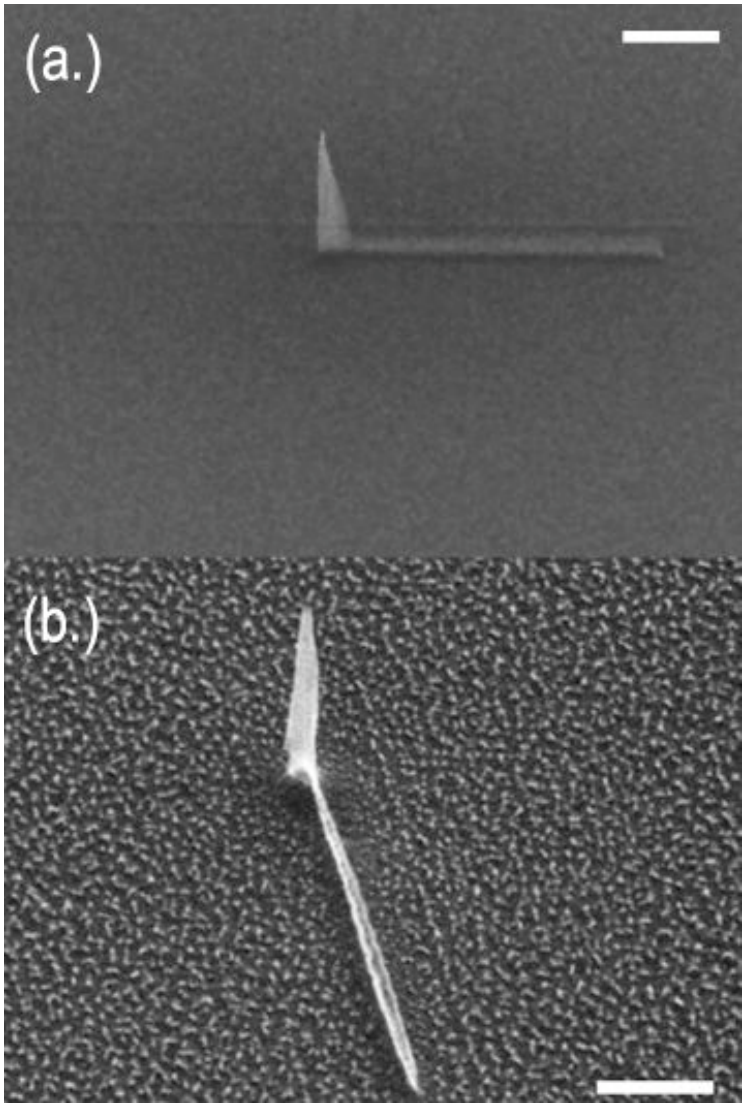

Figure 4-5: Electron Micrograph—Single Layer Line Scan Lithography

An electron micrograph of (a.) a SiO_x line deposited by EBID on an amorphous silicon thin film. The substrate was exposed to a silicon plasma etch to transfer the pattern into the underlying film (b.). The scale bars are one micron in length.

which larger amounts of SiO_x were used, it became clear that the etch mask always sustained unacceptable levels of damage. Therefore, selectivity to the etch mask is a much higher priority than anisotropy. Several experiments were performed in an attempt to characterize the SiO_x etch resistance under a variety of etch conditions. For example, alternative etchant gases such as SF_6/O_2 were tested, as well as the addition of ICP power. While these process modifications somewhat improve selectivity, the required etch conditions (highly anisotropic and highly selective to SiO_2) were not obtained. Chlorine-based silicon etching, as well as variable substrate temperature may be able to provide the required selectivity. For these reasons, experimental emphasis was shifted to a bilayer MDL process, which uses a secondary etch mask of photoresist, which results in higher etch mask selectivity. The next section details the development of the bilayer MDL technique.

4.5 Results and Analysis—Bilayer Process

In an attempt to tailor the selectivity of the etch mask to the attainable conditions in the available RIE system, research focus was shifted to a bilayer MDL process. The envisioned bilayer technique involves the use of an EBID etch mask to pattern a photoresist layer. The purpose of the photoresist layer is to provide a secondary etch mask for the actual pattern transfer into the underlying thin film. Since there is a very high selectivity between tungsten and resist in an oxygen plasma, the problems with the single layer process can be alleviated. The envisioned bilayer process and a subsequent

pattern transfer etch are illustrated in Figure 4-6. Initially, EBID is used to deposit tungsten on a photoresist-coated substrate (Figure 4-6a) resulting in a metallic etch mask for the resist (Figure 4-6b). A dry-develop in an oxygen plasma is used to selectively remove the "unexposed" resist, so that the remainder serves as the final etch mask (Figure 4-6c). The resist/tungsten structure shields the underlying substrate to plasma etching of the substrate (Figure 4-6d). Finally, a solvent soak is used to remove the etch mask and the resulting pattern has been transferred to the substrate in a negative-tone process (Figure 4-6e).

The first step in the experimentation with bilayer MDL was to improve upon existing plasma resist removal processes, so that the dry development could be done quickly and anisotropically. The most effective ways to increase the etch rate of resist was to increase the RIE power and to add ICP power to the oxygen plasma. Figure 4-7 is a bar graph showing the response of the resist etch rate to changes in RIE and ICP power for an oxygen flow rate of 75 sccm and chamber pressure of 75 mtorr for a duration of 90 seconds. The characterization was performed for Shipley SPR 955 CM-2.1 photoresist spun at 250 rpm for 4 seconds, followed by 4000 rpm for 30 seconds. A softbake of 90 seconds at 363 K on a digital hotplate was performed subsequent to spin coating. According to Figure 4-7, increased RIE and ICP power result in higher etch rates. Since there are no selectivity concerns for the tungsten/photoresist system, 500 watts ICP, and 150 watts RIE, were chosen for the baseline dry-develop conditions in subsequent experiments.

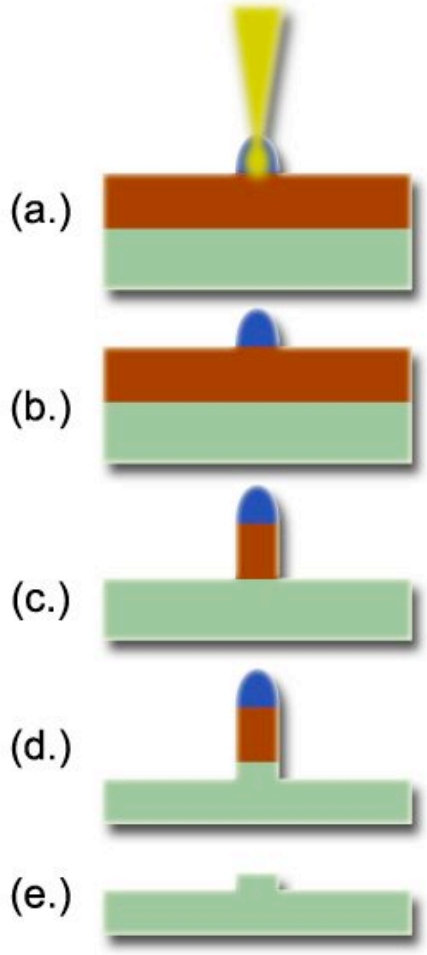

Figure 4-6: Bilayer EBID-Based MDL Process Flow Schematic

Process flow schematic for the bilayer EBID MDL technique. The process involves (a.) EBID tungsten deposition on a resist-coated substrate resulting in (b.) a masking layer. The masking layer is used to protect the underlying photoresist from an oxygen plasma dry develop (c.). The pattern is transferred to the substrate by plasma etching (d.). The masking layer can be removed by solvent stripping (e.).

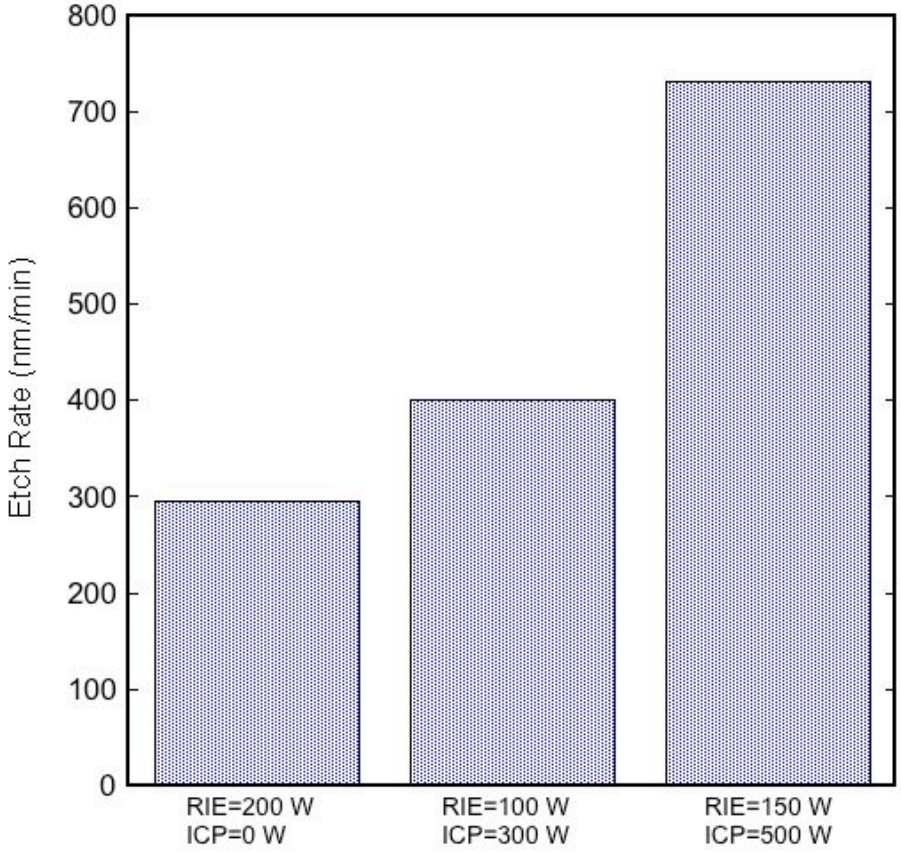

Figure 4-7: Dry-Develop Photoresist Etch Characterization

Bar graph illustrating the effects of RIE and ICP power on the etch rate of Shipley SPR 955 CM-2.1 photoresist. The conditions of the resist etch experiments were 75 sccm oxygen, and 75 mtorr chamber pressure.

One of the first bilayer MDL experiments was performed to determine the feasibility of the process, as well as to examine the effects of deposition conditions. In order to see the effect of dose and scan rate, a series of tungsten EBID lines were deposited on resist using two scan rates and two beam currents. The scan rates used in the experiments were the Hitachi pre-programmed *TV1* and *Slow 3* modes. The *TV1* mode corresponds to ~32 frames per second (0.031 seconds per frame), while *Slow 3* mode corresponds to 7.63×10^{-3} frames per second (131 seconds per frame). Other EBID deposition conditions were 8 mPa chamber pressure, maximum gun brightness (extraction voltage), magnification of ×35,000, and 0.5 nA or 5.5 nA beam current. Figure 4-8 shows SEM micrographs of three of these lines as deposited on a 1.2 μm photoresist both before and after the development process. Charging of the resist while imaging is responsible for the low quality of the images. The lines shown in Figure 4-8a and Figure 4-8b were deposited using 0.5 nA and *Slow 3* scan mode, and received one scan (131 s) and two scans (262 s), respectively. The line in Figure 4-8c was deposited using *TV1* mode, and 5.5 nA beam current for 180 seconds. The resist etch process was applied for 2 minutes to develop the samples.

These initial experiments revealed several issues that would have to be resolved with the bilayer MDL process. First is the obvious problem with peripheral contamination. The excellent etch resistance of tungsten to the oxygen plasma was evident in the fact that even trace amounts of peripheral contamination masked the underlying resist. Therefore, considerable residual resist remained on "unexposed" regions, thus compromising the feature geometry. This effect is most pronounced in the

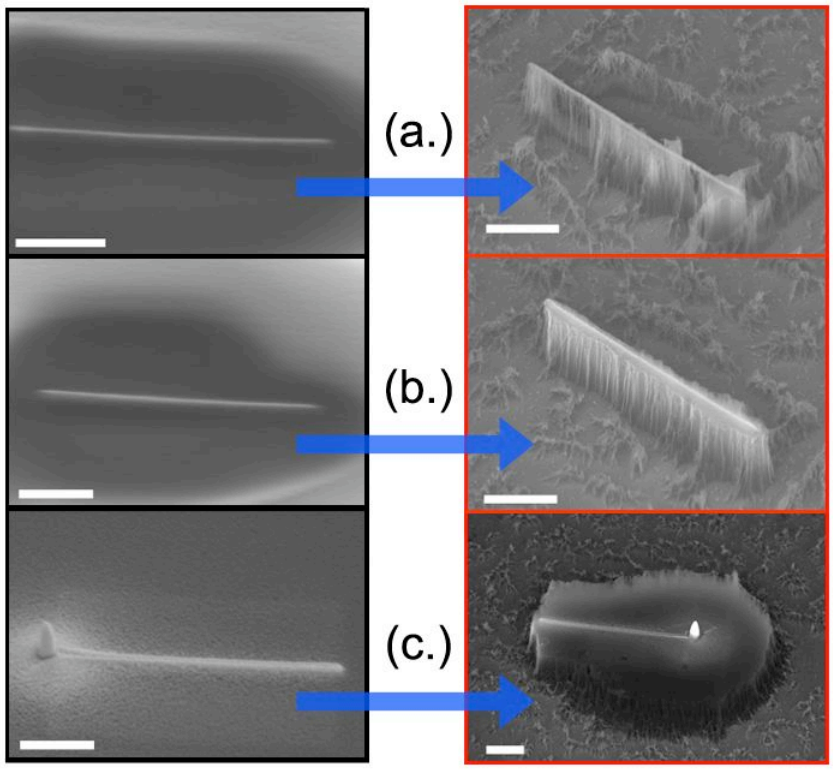

Figure 4-8: Initial Bilayer MDL Exposure and Develop

Electron micrographs of three initial experiments in bilayer MDL showing post-deposition (left) and post-develop (right). The beam current for (a.) and (b.) was 0.5 nA, and 5.5 nA for (c.). The lines (a.) and (b.) were performed with scan mode *Slow 3* with (a.) receiving one scan and (b.) receiving two scans. All scale bars are one micron and image tilt is 46^{o}.

high current case shown in Figure 4-8c. This situation is analogous to a very high sensitivity resist, in that the dose required for exposure is very small. One of the problems that this presents is that the sample must be imaged prior to deposition, since experiments are being carried out in an SEM. This means that for every experiment, regions that should not have been exposed received a finite dose, and therefore became partially masked during development.

The unwanted masking of regions occurs in an analogous manner in standard photolithography. After exposure and development, a very small amount of resist may remain in the exposed and developed region. As this will cause unwanted masking, a process known as a "descum" is usually performed to eliminate the residual resist or "scum". The substrate is briefly exposed to an oxygen plasma, which aggressively attacks resist. Since the amount of scum is very small, it is etched away very quickly, while the bulk of the intentional resist remains (because it is much thicker).

Since the same type of problem occurred in the bilayer MDL process, it was determined that a refractory metal descum process was necessary. As the unwanted etch mask in this case was tungsten, a fluorine-based plasma descum was performed on the same samples shown in Figure 4-8. The conditions of the descum etch were 50 W RIE power, 150 mtorr chamber pressure, 45 sccm SF_6, 5 sccm O_2, and 15 seconds of etch time. The descum was followed by another 120 second oxygen plasma dry development. One of the results of this process is shown in Figure 4-9. Clearly, the descum removed a large portion of the contamination, thus allowing the underlying resist to be removed. This result showed that features could possibly be trimmed to reduce feature dimensions.

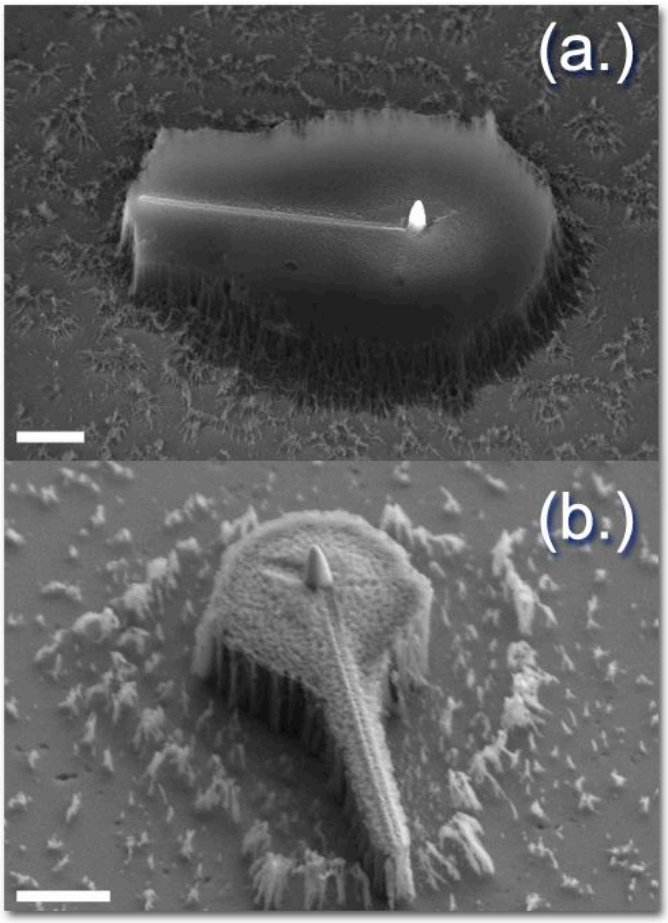

Figure 4-9: Effect of Refractory Descum

Electron micrographs of bilayer MDL experiments where (a.) dry development was performed on line deposit. After a refractory descum and a second dry development (b.), much of the peripheral contamination was removed. Scale bars are one micron and image tilt is 46^{o}.

Another interesting observation from Figure 4-9 is that following descum and development, the outline of the original contaminated region was still visible, but highly damaged (Figure 4-9b). It was originally thought that the dry development process might not be quite effective as necessary. However, a series of experiments with increasingly aggressive oxygen plasma conditions revealed that these conditions had little effect on the amount of residual resist. While this is not fully understood, possible explanations will be presented in the context of other experiments to be discussed below.

A noteworthy observation from Figure 4-8 is that dose and scan rates only seem to affect the levels of contamination and the ultimate linewidth. In accordance with electron scattering in a nanostructure, the two-scan line is wider than the one-scan line shown in Figure 4-8. Again, this is promising for bilayer MDL because high-resolution and high-throughput are the ultimate goals. High sensitivity resist schemes such as this process require lower doses, which can be controlled by lower exposure times. Therefore, process resolution and exposure time are coupled in a desirable fashion. The slow scan rates do not produce the nanofiber at the settle spot, therefore the lines have better uniformity than those produced by high scan rates.

The next bilayer MDL experiments were performed in order to determine the effects of both beam current and beam energy during EBID. Two beam currents were chosen (2.38 nA and 0.11 nA) to investigate the beam current effects on line patterning as well as two beam energies (20 keV and 10 keV). The deposition conditions were a chamber pressure of 7.8 mPa, maximum gun brightness, *Slow 3* scan rate, and 3 scans per deposited line (393 seconds). In an attempt to take the bilayer process to completion, a

silicon plasma etch was performed following the dry development step.

Figure 4-10 shows electron micrographs of the two lines deposited at 20 keV. These images include a normal view of the post-EBID lines, a tilted view of the lines post-development, and a tilted view of the lines post-etch. To reduce the damage to the etch mask, the refractory descum was changed from RIE power to ICP power. As evident from the images in Figure 4-10, the ICP-based descum was more effective at cleanly removing the EBID contamination resulting in better pattern definition and significantly less residual resist. The descum process is very helpful for reducing the amount of peripheral contamination but, unfortunately, the desired etch mask is also attacked. For high resolution, which requires low dose, the amount of etch mask material is very small, and thus susceptible to damage from even mild descum procedures. This type of damage is shown in the post-development image of Figure 4-10 in which the line is not only broken, but also non-uniform. In contrast, the high dose line in Figure 4-10 is minimally impacted by the descum process.

Another significant observation regarding Figure 4-10 is the poor quality of pattern transfer by etching for both low and high doses. The low dose etch mask was destroyed by the subsequent silicon etch, while the high dose etch remained, but collapsed. In both cases, the transferred feature was much larger than the etch mask. This indicates that regardless of the size of the patterned etch mask, additional masking still occurs at the silicon surface. Since the beam diameter is on the order of nanometers, the broadening of the feature must be an artifact of electron scattering in the resist layer.

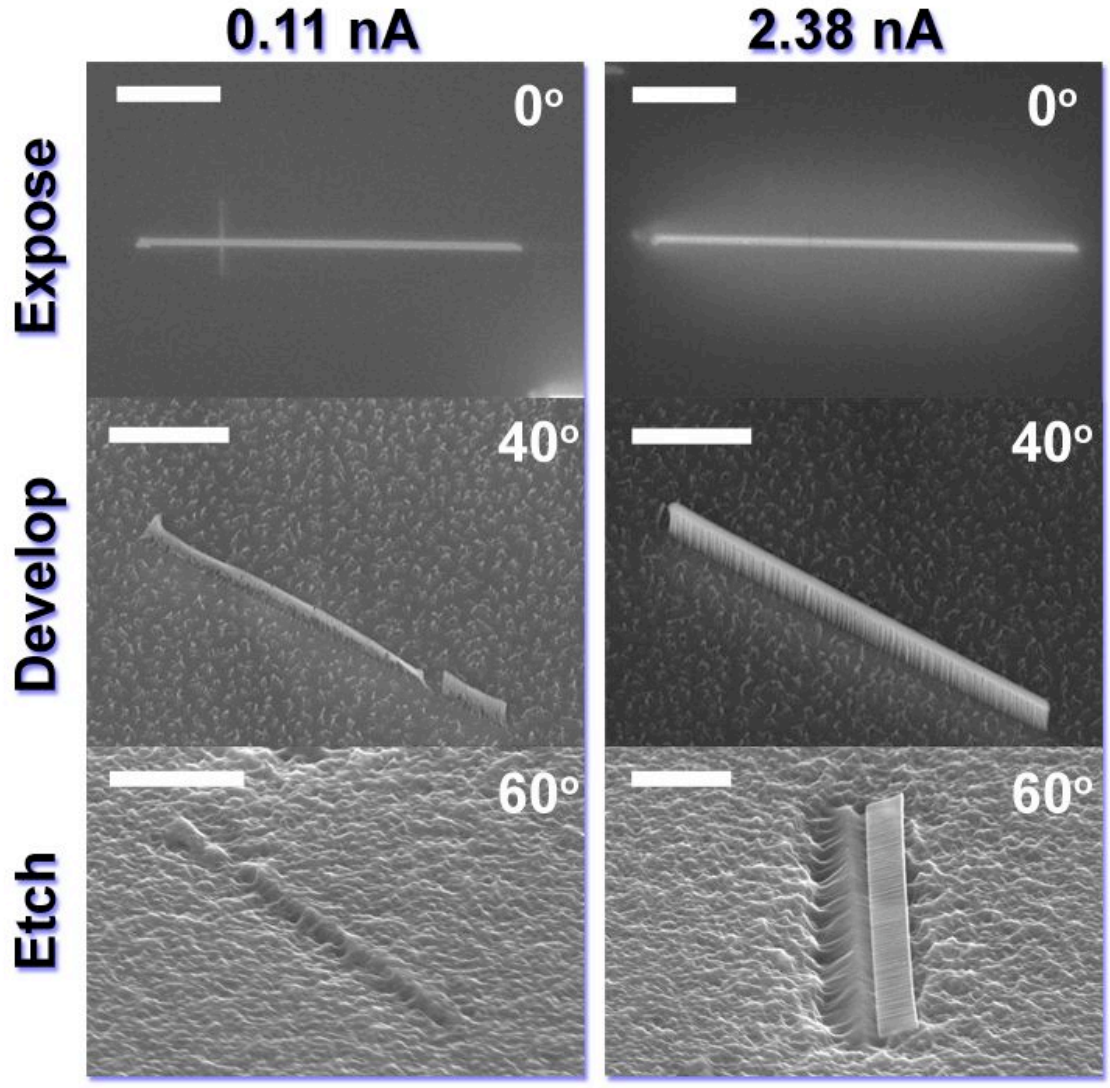

Figure 4-10: Beam Current Effects on 20 keV Deposition

Electron micrographs of bilayer MDL experiments where two beam currents were used to deposit identical lines. The top images are as-deposited EBID tungsten lines. The middle images are following a refractory descum and dry develop. The bottom images are following a silicon plasma etch. Scale bars are three microns.

In order to investigate this assumption, several Monte-Carlo electron scattering simulations were performed. The single-scattering model as described in Chapter 3, and shown in Appendix A, was used to simulate BSE surface distributions of PMMA for two beam energies (5 keV and 20 keV). In order to simulate experimental conditions, the model used a PMMA thickness of 1.2 μm on a silicon substrate. The results of this simulation are plotted in Figure 4-11. While the BSE distribution is only one aspect of the electron-PMMA interaction, it provides a simple method of visualizing the anticipated electron flux at the surface (not including the incident beam). The Monte-Carlo simulation parameters used for PMMA were an average atomic number of 6.5, an average molecular weight of 13 g/mol, and density of 1 g/cm^3. As expected, the broadening of the beam in PMMA is a strong function of beam energy, with higher energies resulting in increased scattering distances. The plot in Figure 4-11 represents a view of the BSE fraction relative to beam energy. Clearly, the BSE fraction is much higher at larger distances for high beam energies. Consequently, while high beam energy yields higher resolution features, the breadth of the interaction region results in excessive EBID contamination.

These conclusions regarding scattering in the resist are supported by the results of the second set of lines, which were deposited at 10 keV. Figure 4-12 contains electron micrographs of the experiments that were performed with two beam currents—0.004 nA and 0.91 nA. The 20 keV and 10 keV experiments were performed on the same sample, so the post-deposition processing was identical. Therefore, the differences between Figure 4-10 and Figure 4-12 are due to deposition conditions. Similar to Figure 4-10,

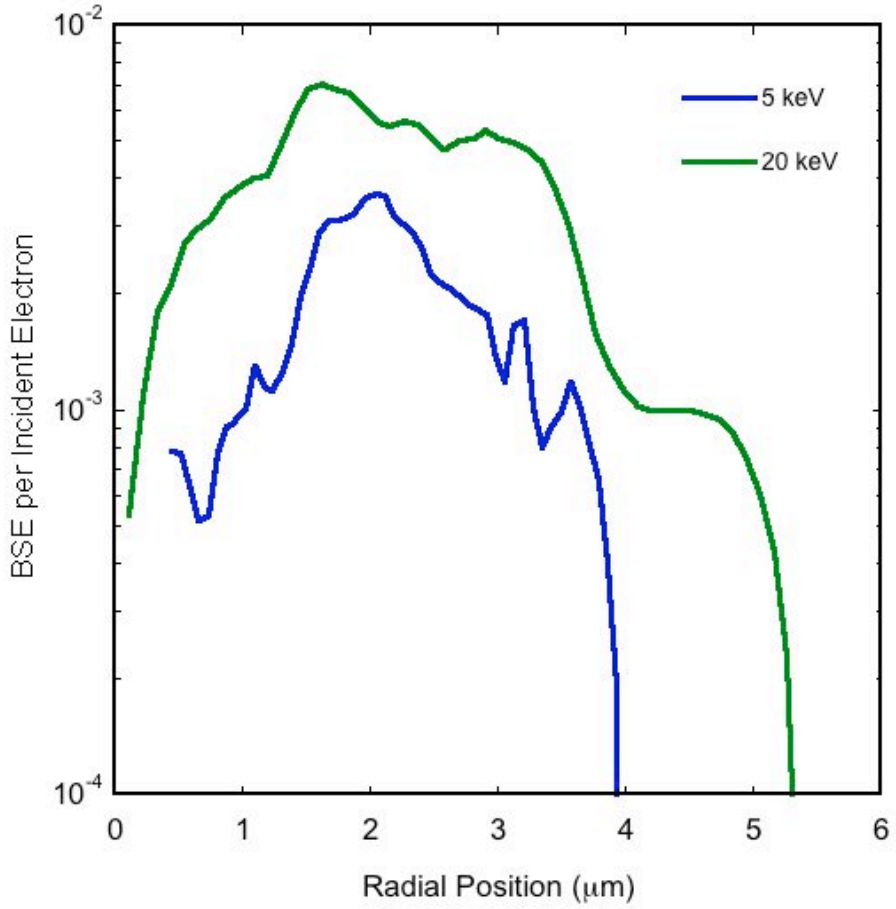

Figure 4-11: Simulated BSE Surface Distribution in PMMA

A plot showing the backscattered fraction of incident electrons in PMMA as a function of radial position. The data was normalized relative to the highest fraction of the two beam energies. High beam energies result in much higher BSE current at great distances from the beam.

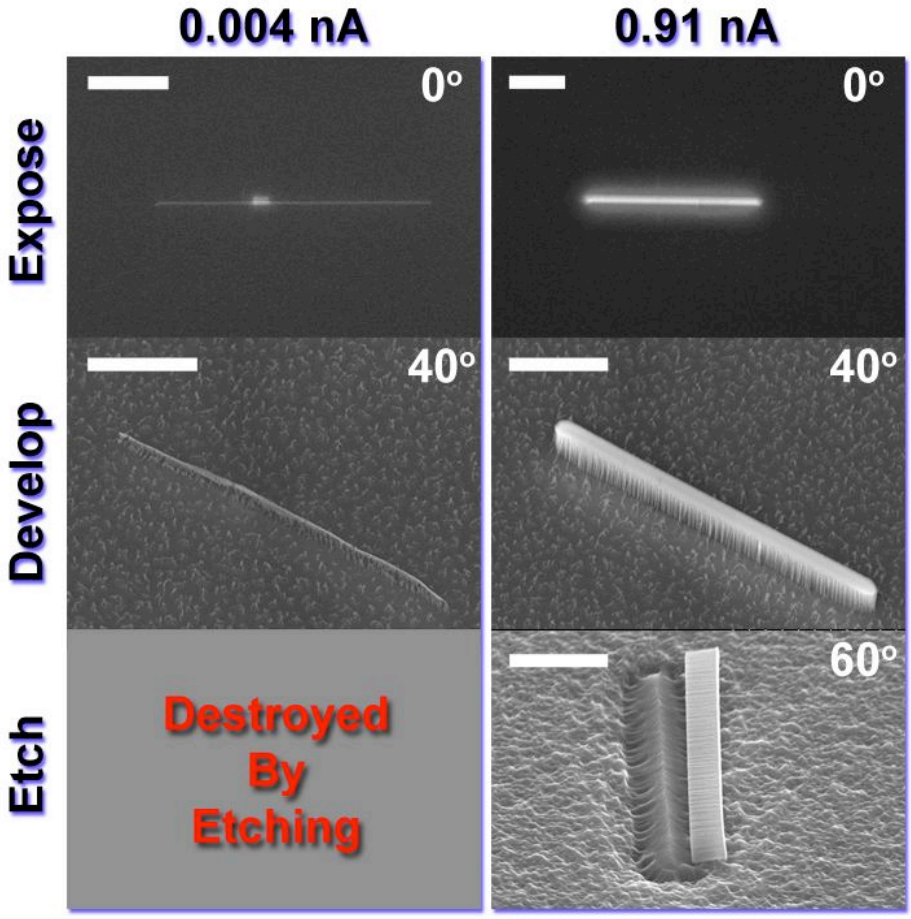

Figure 4-12: Beam Current Effects on 10 keV Deposition

Electron micrographs of bilayer MDL experiments where two beam currents were used to deposit identical lines. The top images are as-deposited EBID tungsten lines. The middle images are following a refractory descum and dry develop. The bottom images are following a silicon plasma etch. The low dose pattern did not survive etching. Scale bars are three microns.

Figure 4-12 includes post-deposition, post-development, and post-etching images. While the 10 keV high dose feature is larger than the 20 keV high dose feature, the peripheral contamination around the 20 keV line extends much farther. To aid visualization of this scattering phenomenon, Figure 4-13 includes close-up images of the two high dose lines. The image has been modified by tinting the contaminated region for emphasis. From Figure 4-13 it can be seen that the contamination spread for the 10 keV line is ~2.5 μm, while for the 20 keV line, the spread is ~ 5.7 μm.

Other observations from Figure 4-12 are similar to those made previously that sufficient dose is critical for etch mask survival. The low dose, 10 keV line was damaged during the descum process and did not survive the subsequent etch. The 10 keV high dose line did survive the descum and etch, but similar to the 20 keV high dose line, the etch mask collapsed during etching. While this is not fully understood, it is possible that the plasma results in charging of the resist and the ensuing forces on the lines cause the collapse.

Another problem with the bilayer MDL process may be related to the interaction of scattered electrons with the photoresist at the silicon surface. The micrographs of the high dose line in Figure 4-12 show an interesting phenomenon. Obviously, the contamination is visible in the post-deposition image of Figure 4-12, but closer observation of the post-development image shows that there is a slight discoloration of the surface surrounding the etch mask. This discoloration corresponds to the location of the contamination ring, but is actually at the silicon surface. From the post-etch image in Figure 4-12, it can be seen that etch masking occurred in the discolored region. This

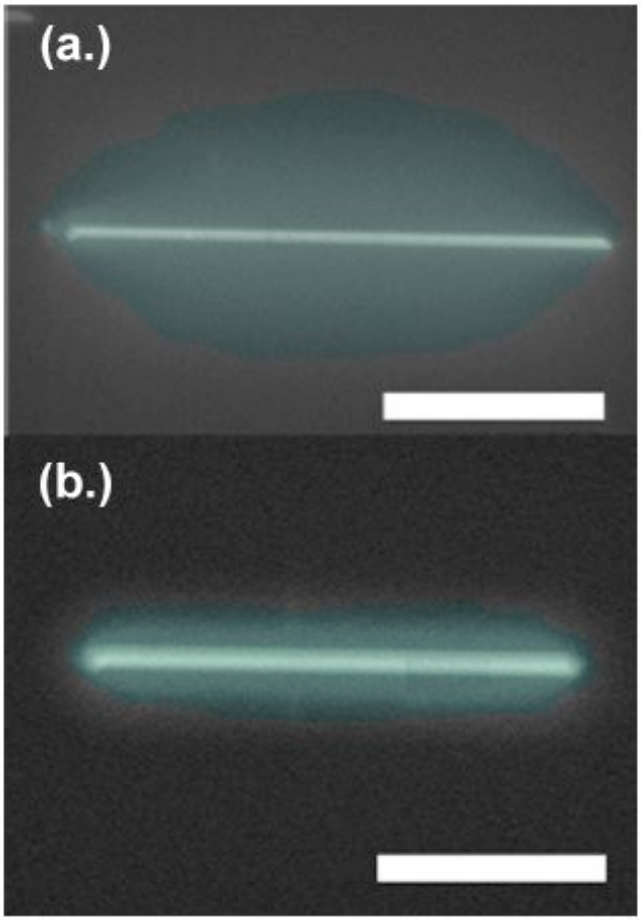

Figure 4-13: Contamination Due to Electron Scattering in Resist

Electron micrographs of bilayer MDL experiments where (a.) 20 keV beam energy and (b.) 10 keV beam energy were used to deposit lines. Higher energy results in higher resolution, but more scattering contamination. Low energy results in a loss of resolution, but less scattering contamination. Scale bars are five microns.

indicates that the discolored region is somehow modified, resulting in differential selectivity to the silicon plasma etch. While this effect is not fully understood at this time, it could be related to electron-beam modification of the photoresist at the interface.

To investigate this effect, single-scattering Monte-Carlo simulations were performed in order to see the interfacial effects in this modified region. The simulation conditions were 1,000 electrons, and 10 keV beam energy. Figure 4-14 shows a plot of the interaction volume assuming a one-micron PMMA resist on a silicon substrate. As silicon scatters electrons more efficiently than photoresist, there is an increase in the power density deposited at the interface relative to the bulk of the resist. While this is not conclusive, this increase in energy deposited at the interface may result in "burning" of the resist, resulting in increased plasma etch resistance. This could possibly explain the etch masking that occurs as shown in Figure 4-12.

The common theme among all of the previously discussed bilayer MDL experiments is that electron scattering in the resist layer compromises the process. Whether the problem is scattered-electron-induced deposition at the resist surface or electron interactions at the silicon/photoresist interface, scattered electrons in the resist layer appeared to be the main problem. There are at least three potential solutions to these observed difficulties, both of which reduce the spatial spread of electrons in the resist layer.

One method of reducing the electron spread is by use of a photoresist with different electron scattering properties. It is possible to envision a highly scattering resist layer in which the scattered electrons remain highly localized at the resist surface, thereby

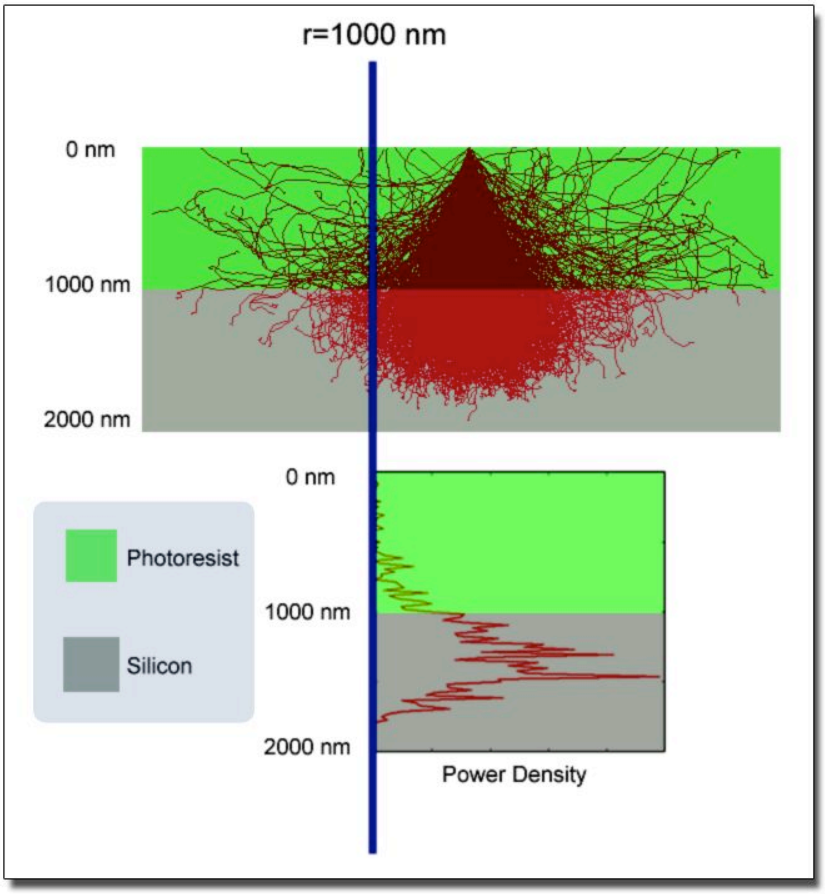

Figure 4-14: Energy Deposited at Silicon/Photoresist Interface

Results of a Monte-Carlo simulation of 10 keV electrons in a 1000 nm photoresist on silicon. The deceleration of electrons at the interface results in an increase in the power density deposited at the interface. This may be the origin of the unwanted etch masking surrounding the EBID feature.

reducing the spatial spread of scattered electrons. The opposite case could also be applied, where a relatively non-scattering resist is used, so that the incident beam is scattered a minimal amount. Unfortunately, the change of resist material introduces several additional problems, which may offset the benefits of the bilayer process. The high selectivity between the tungsten EBID layer and the underlying photoresist was the main advantage of the bilayer approach for MDL. A change of material systems would require substantial additional research efforts, which will involve new dry-development and etch mask removal strategies. Therefore, it was determined that the approach of changing resist materials would best be left to future research.

A simpler method of reducing the spread of electrons in the resist involves a careful consideration of the effects of incident beam energy on electron scattering. As the beam energy is increased, the interaction volume increases, which results in a greater spatial distribution of electrons. Therefore, low beam energy is likely to be better suited for bilayer MDL applications and yield a more localized contamination region. It is important to recall that the MDL processes discussed in this chapter are being developed to use in conjunction with the DEAL concept parallel electron beam lithography system. The DEAL system is designed to be operated at electron energies of less than 1 keV.[108] Whereas development of the bilayer MDL process has been performed in an SEM where resolution is compromised at low energies, if realized, the DEAL system should be able to overcome this problem by using short working distances. In an attempt to understand resolution-limiting processes, and to confirm process viability, the SEM was operated at 5 keV energy and above because of degraded SEM performance at low energy. While

these conditions are outside of the DEAL operating limits, it is anticipated that the information obtained from gained such studies may extrapolate to lower energy. For this reason, development of the bilayer MDL process was continued using effective SEM beam energies, and other electron-spread-limiting measures must be investigated.

Perhaps the most straightforward method for reducing the electron spread in the resist layer for ideal SEM conditions is through control of the resist thickness. The simulation results presented in Figure 4-14 show that as electrons penetrate the resist and enter the silicon substrate, they are scattered more efficiently. Consequently, the electrons are localized in a smaller interaction volume than would occur in the absence of the silicon. This implies that the silicon substrate itself can act as an electron "trap" by more effectively decelerating the scattered electrons. The additional energy lost to the silicon substrate can be the difference between an electron remaining in the sample or being able to re-emerge at the resist surface and induce contamination. Therefore, coupled optimization of the electron trapping and minimization of electron spread in the resist is likely to result in more desirable bilayer MDL results.

In order to explore this hypothesis, several Monte-Carlo single scattering simulations were performed to further evaluate the potential effects of the resist/silicon interface. Since a Monte-Carlo-based EBID model is beyond the scope of this work, it is necessary to use indicators from the simulation that can provide insight as to trends might be expected. One such indicator is the spatial distribution of BSE as was used to qualitatively explain the peripheral contamination issues (see Figure 4-11). Figure 4-15 is a plot of the simulated BSE spatial distribution at the resist surface for a beam energy

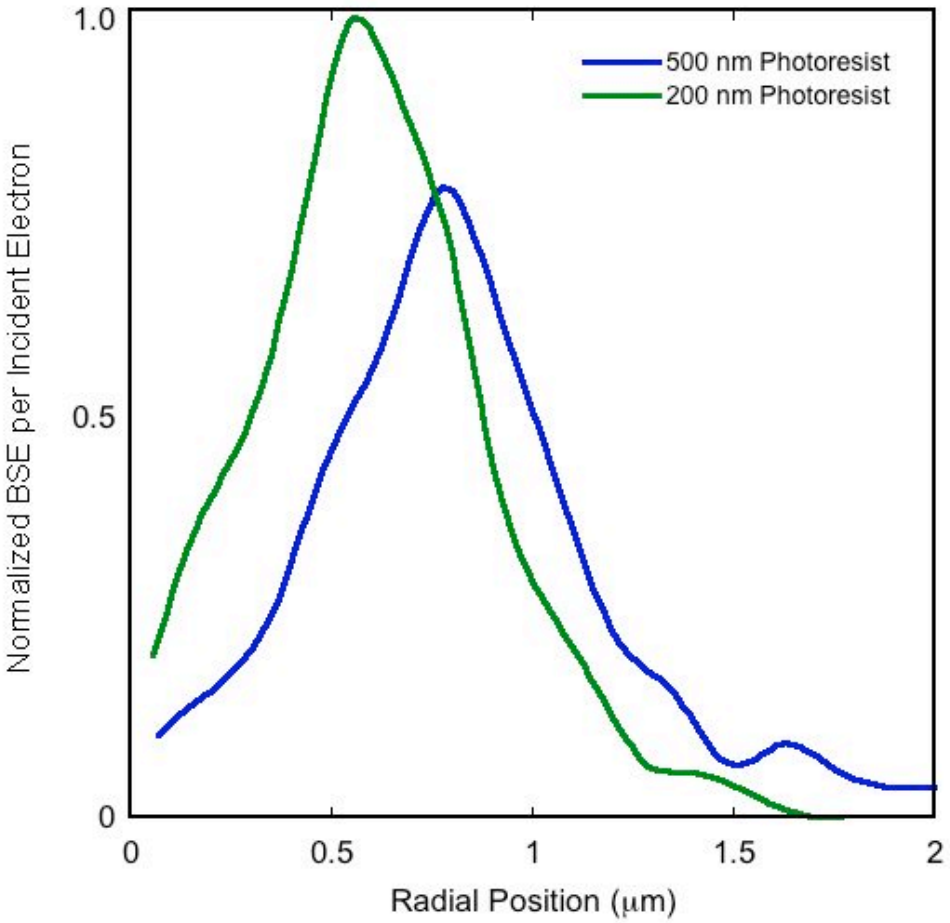

Figure 4-15: Effect of Resist Thickness on Electron Spread

Results of a Monte-Carlo simulation of 10 keV electrons in a 500 nm and a 200 nm resist on silicon. Electrons penetrate the thin resist and less spread than with a thick resist. The result of this is a more confined electron flux distribution at the resist surface for thinner resists.

of 10 keV, and with 2,000 electrons simulated. Two different resist thickness were modeled in order to illustrate the effects of decreased scattering on the BSE surface flux. It can be seen that by decreasing the thickness of the resist from 500 nm to 200 nm, that the resultant BSE distribution is modified. By lowering the resist thickness, the electrons penetrate the resist more quickly, which results in less spatial spread of the scattered electrons. The net result of this effect is that the BSE are confined to a smaller area, and result in a higher electron flux nearer to the incident beam. This is an intuitive result inasmuch as it is expected that the BSE distribution will approach the silicon BSE coefficient as the resist thickness approaches zero.

In addition to the BSE distribution, other simulated indicators can be employed to further elucidate the effects of resist thickness on the spatial spread of electrons. By running a series of Monte-Carlo simulations with varying resist thickness, a tremendous amount of information is generated, all of which may be useful if viewed correctly. For instance, the average radial deviation of electrons from the impact point may be useful as a measure of electron spread. Similarly, the maximum radial displacement of a single electron may also provide a measure of the electron spread. The seemingly endless variations of data representation and the multi-dimensional nature of the problem add to the complexity of choosing which data to analyze. Again, it is beyond the scope of this work to extensively investigate the simulated electron spread. For that reason, the least code- and computationally-intensive indicator was chosen to very briefly verify the effects of resist thickness on the electron spread. In this case, the maximum radial position achieved by any single electron was used as an indicator of the breadth of the

electron spread. Figure 4-16 displays the results of several simulations with varying resist thickness in which the output was maximum radial position. Clearly, there is an initial sharp increase in the maximum radial position with increased resist thickness, which subsequently reaches an approximate plateau. The peak value of the spread occurs for a resist thickness of approximately 400 nm. Coincidentally, the 400 nm resist thickness corresponds to ~ 13% ($1/e^2$) of the modified Bethe range, R_B, of 10 keV electrons, which is given by integration of Eq. (3.5). The modified Bethe range for 5 keV electrons yields a Bethe range of ~ 920 nm, 13% of which is ~ 120 nm. Subsequent simulations using 5 keV electrons showed that the maximum radial spread occurred at approximately 120 nm after which a plateau value was reached. The functionality of the 5 keV data was nearly identical to that of Figure 4-15. While certainly not conclusive, these initial calculations suggest that that the quantity R_B/e^2 may represent the upper limit on the desired resist thickness, below which the size of the scattered electron volume decreases sharply.

The next bilayer MDL experiments were intended to test these theoretical insights and improve the process resolution by using thin a thin photoresist layer. The previous experiments utilized Shipley SPR 955 CM-2.1 for the resist layer. In order to obtain a thinner resist layer, Shipley SPR 955 CM-0.7 was used. The two resists are chemically identical, but the latter has a much lower viscosity, which allows for thinner coatings. A spin speed of 5,000 rpm was used to spin the resist on a silicon substrate to a thickness of approximately 360 nm.

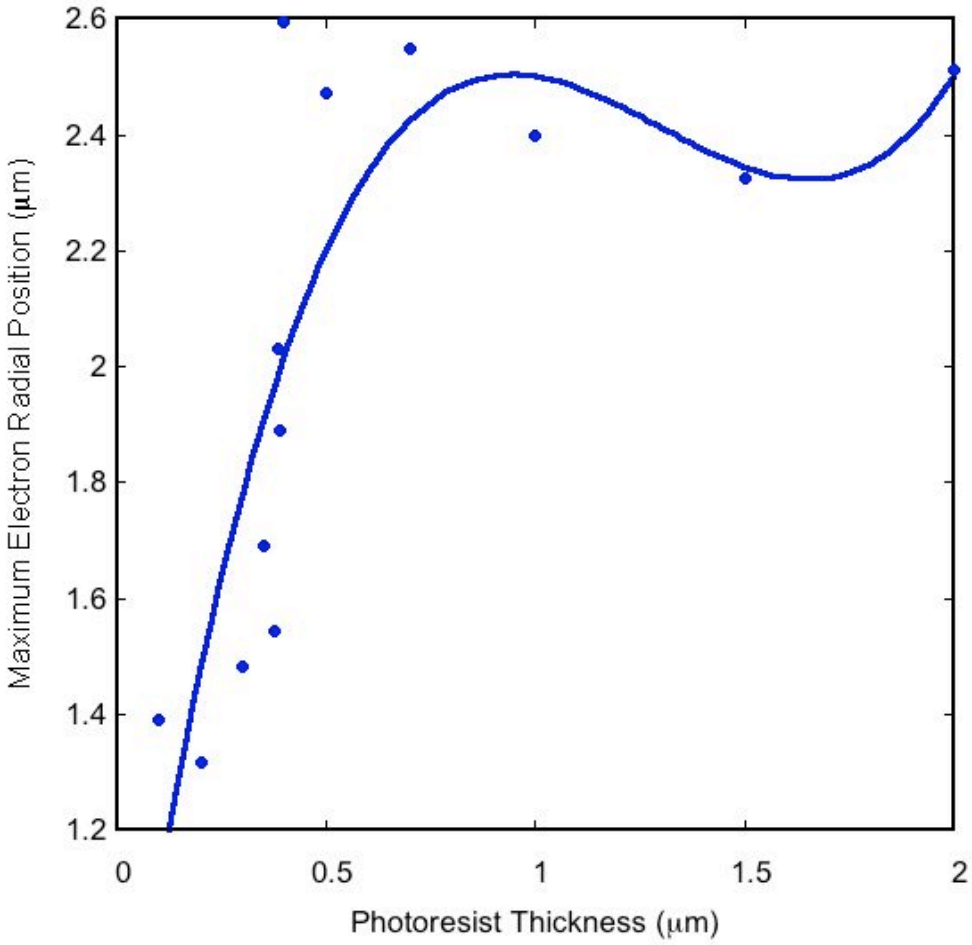

Figure 4-16: Effect of Resist Thickness on Maximum Electron Radial Position

Results of a Monte-Carlo simulation of 10 keV electrons in variable resist thickness on silicon. The maximum radial position of electrons is decreased sharply for thin resist, resulting in a confined scattered electron volume.

Several bilayer MDL experiments were performed to investigate the process on the thinner resist. Two different beam energies—5 keV and 30 keV—were used to deposit of series of lines using *Slow 3* scan mode (131 seconds per frame) with varying electron doses. Common deposition conditions were a chamber pressure of 8 mPa and maximum gun brightness. After deposition, all samples were exposed to a 10 second refractory descum, followed by a 90 second dry-develop, and a 90 second silicon ICP plasma etch.

Figure 4-17 shows the results of a high dose, low energy experiment in which beam energy of 5 keV and a beam current of 120 pA were used to deposit a line with a single *Slow 3* scan. The results displayed in Figure 4-17 support the hypothesis that reduced scattering in a thin resist should improve the bilayer MDL process. It appears that the effects of reduced scattering by the resist and lower beam energy work in concert to improve the uniformity of the deposit and reduce the amount of peripheral contamination. The linewidth of the feature as shown in Figure 4-17 after etching was approximately 300 nm. While this linewidth is much larger that desired, the uniformity offers promise.

Additional lines were deposited at 30 keV beam energy with both a single and a double pass of *Slow 3* scans. The post-deposition processing parameters for these two lines was identical to the previous dry-development and silicon etch parameters. Figure 4-18 shows the results of the double scan process, and Figure 4-19 displays the results of the single scan process. The increased resolution of the beam at 30 keV translates to higher resolution lines as shown in Figure 4-18 and Figure 4-19. These two figures

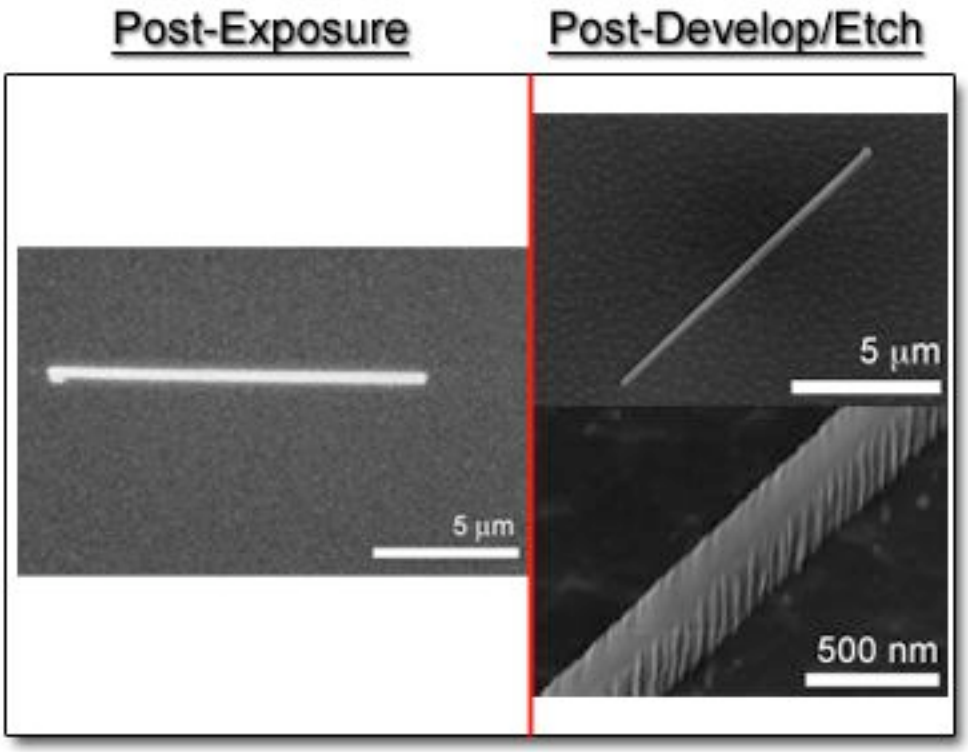

Figure 4-17: Thin Resist MDL—Low Energy, High Dose

Electron micrographs of post-exposure and post-develop/etch MDL experiments in which 5 keV beam energy and 120-pA beam current were used to deposit lines with a single scan. Much improved etch uniformity was observed with the thin resist process. The resultant linewidth is ~ 300 nm. The images on the right were taken at a 40^{o} tilt.

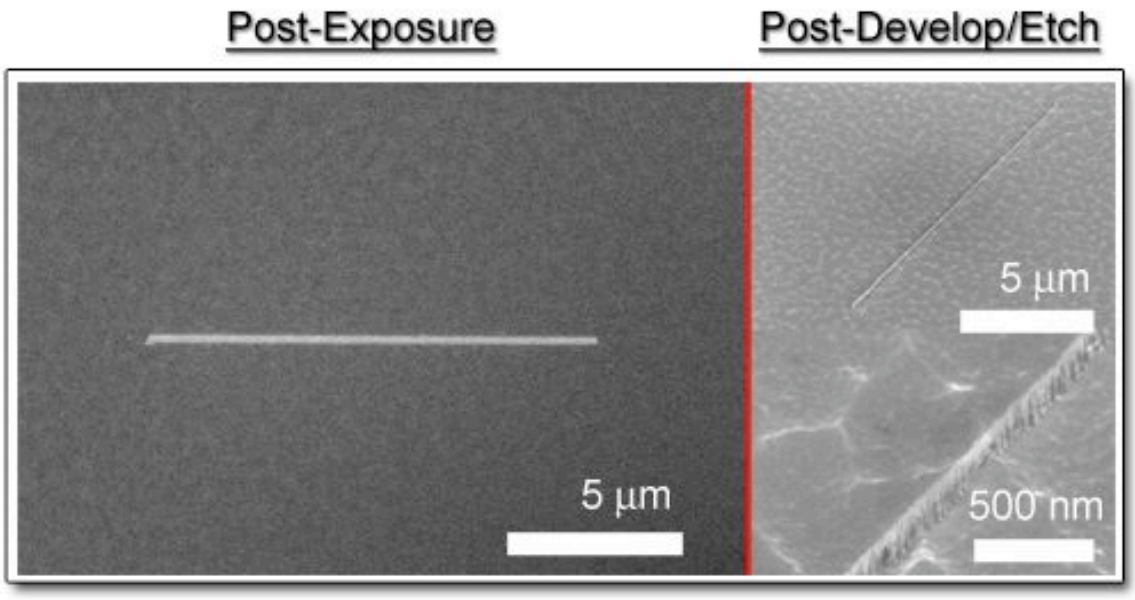

Figure 4-18: Thin Resist MDL—High Energy, Double Scan

Electron micrographs of post-exposure and post-develop/etch MDL experiments in which 30 keV beam energy and 1.15 nA beam current were used to deposit a line with a two scans. Linewidth is reduced by using 30 keV. The resultant linewidth is ~ 85 nm. The images on the right were taken at a 40^{o} tilt.

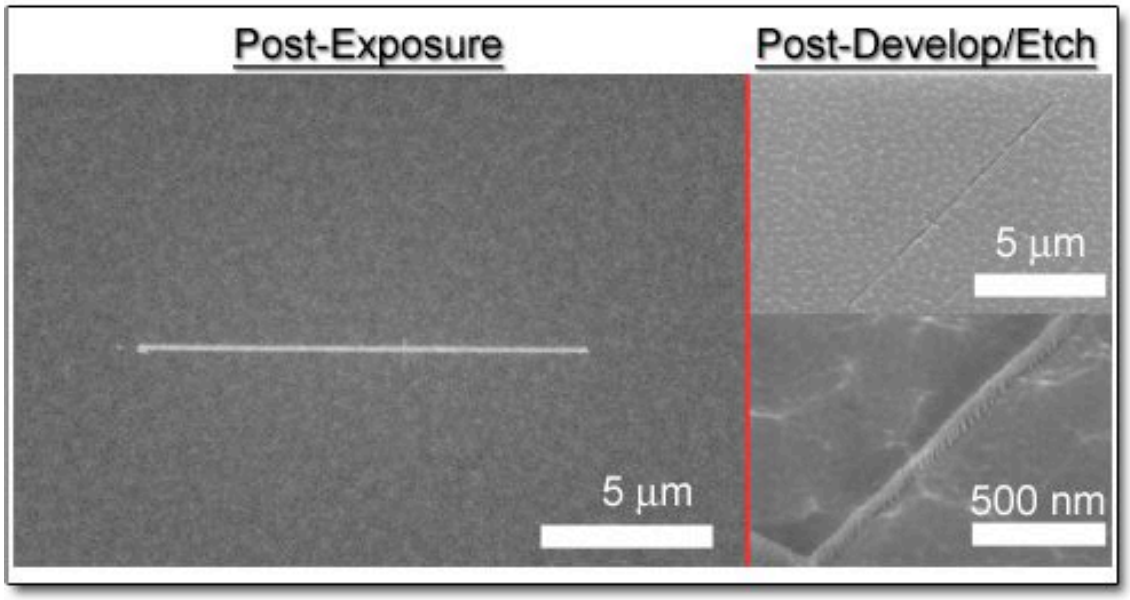

Figure 4-19: Thin Resist MDL—High Energy, Single Scan

Electron micrographs of post-exposure and post-develop/etch MDL experiments in which 30 keV beam energy and 1.15 nA beam current were used to deposit a line with a single scan. Linewidth is reduced by using a single scan as opposed to a double scan. The resultant linewidth is ~ 60 nm. The images on the right were taken at a 40^{o} tilt.

demonstrate that the dose received from a single line scan with 1.15 nA beam current is sufficient to provide an etch mask. In this case, the double scan shown in Figure 4-18 is overexposed, so that the linewidth was compromised. The linewidth of the double scan in Figure 4-18 is approximately 85 nm, while the single scan linewidth in Figure 4-19 is approximately 60 nm.

The final, and most promising thin resist bilayer MDL experiments were performed with the same conditions as in the previous three experiments. The beam energy used was 5 keV, and a very small beam current of 3 pA was used to deposit the EBID tungsten. Single and double scans were performed, both of which were adequate dosages for surviving the refractory descum, dry development, and etch. In an attempt to minimize the peripheral contamination, no post-exposure imaging was performed. Therefore, only the results of the post-develop/etch are shown in Figure 4-20. These results show that the best linewidth of approximately 35 nm occurs with the smallest current used. Assuming a beam diameter of 35 nm, this corresponds to a dose of ~10^5 $\mu C/cm^2$, or a line dose of 39.3 $\mu C/cm$. While this dose is orders of magnitude higher than that required for many EBL resists, the survival of the etch mask under these conditions implies that even lower doses may be adequate and produce even smaller linewidths.

4.6 Summary and Future Work

Two approaches to maskless, direct-write lithography using electron beam-induced deposition (EBID) to produce ultra-thin masking layers were investigated. One

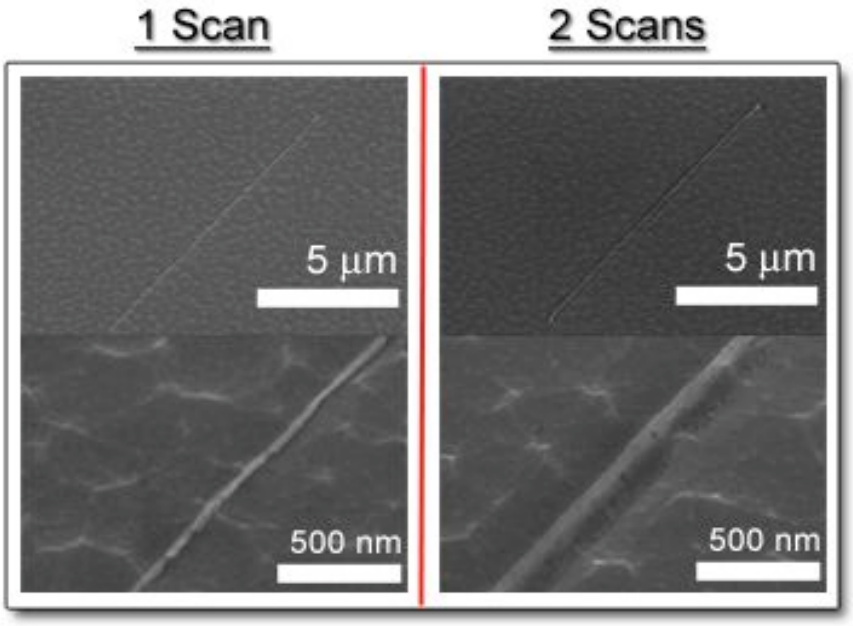

Figure 4-20: Thin Resist MDL—Low Energy, Low Dose

Electron micrographs of post-exposure and post-develop/etch MDL experiments in which 5 keV beam energy and 3 pA beam current were used to deposit lines with a single scan and a double scan. The minimum linewidth was obtained by using this very low dose. The resultant linewidth of the single scan was ~ 35 nm, and the linewidth for the double scan was ~ 115 nm. The images on the right were taken at a 40^{o} tilt.

of the processes (single layer) made use of directly written SiO_x features deposited from a tetraethoxysilane precursor vapor as a masking layer for an amorphous silicon thin film. The second process (bilayer) implemented a secondary masking layer consisting of standard photoresist into which a pattern—directly written by EBID tungsten from WF_6 precursor—was transferred.

The single layer process was found to be extremely sensitive to the etch selectivity of the plasma etch. Several silicon etch process parameters were explored, but the etch mask typically only survived a few seconds of plasma etching. As a result, patterns were successfully transferred into silicon, but only to a minimal depth. It is believed that the limitations of the single layer lithography process can be overcome by optimization of the reactive ion etch process. With the addition of substrate and chamber heating/cooling, and the ability to use a chlorine-based plasma, it is likely that the selectivity can be increased substantially. Therefore, future experiments with the single layer process may yield more success using a better-suited dry etch system. In addition, different EBID material systems should be investigated for increased selectivity to the desired substrate or thin film material.

The selectivity problems with the single layer process necessitated a shift of focus from a single layer process to a bilayer process. The bilayer lithography technique involved the use of a secondary masking layer of photoresist on which the pattern is directly written by tungsten EBID. The excellent etch resistance of tungsten in an oxygen plasma was the primary reason for choosing it as the direct-write masking layer. Several parameters were varied in order to establish an anisotropic oxygen plasma dry-

development process for transferring the EBID pattern into the underlying photoresist.

Additionally, the effects of deposition parameters on the resulting bilayer pattern transfer were investigated. It was determined that electron scattering in the resist resulted in significant peripheral contamination problems, which compromised the geometry and integrity of the desired feature. A brief refractory descum plasma etch was implemented to remove the peripheral tungsten contamination prior to the development process. Etch mask survival during the descum process was found to be dependent upon the pattern receiving sufficient dose. It was also established that overexposure by either excessive current, or excessive scan time resulted in increased linewidth.

Bilayer experiments were designed in order to reduce the spatial spread of electrons in the photoresist layer and obtain minimal linewidths. The use of thin photoresist layers and low beam energies reduces the spread of electrons in the resist. These conditions, coupled with lower dose (low current and short scan times) were used to produce lines with an average width of ~ 35 nm.

Several bilayer experimental results presented indicate great future potential for the maskless, direct-write process. Future development of the technique should include an optimization study for determining minimum dose requirements. An additional optimization study regarding the minimum resist thickness could contribute to improved process resolution. The presented results suggest that the rapid deceleration of electrons at the photoresist/silicon interface reduces scattering contamination.

For this reason, a highly dense electron-stopping layer beneath the photoresist might be a worthwhile subject of future investigation. Perhaps the most promising future

application is for the implementation with the Digital Electrostatically focused e-beam Array Lithography (DEAL) concept, which will require ultra-thin, direct-write resist schemes. The low landing energy (less than 1 keV) and proposed dose control system of DEAL are ideally suited for high resolution EBID bilayer lithography processing. With optimized deposition, post-deposition processing, and electron optics, it seems feasible that the process could be used to produce sub-10 nm features.

Chapter 5—EBID Device Application: Digital Electrostatically Focused Electron-beam Array Direct-Write Lithography (DEAL) Field Emitter Repair

5.1 Introduction and Motivation

As discussed in Section 4.1, the push for higher resolution lithography has inspired a vast amount of research into novel patterning techniques. Standard photolithographic processes are rapidly approaching their fundamental limits. While current electron beam lithography (EBL) can approach the desired resolution for near-future industrial requirements, other issues such as low wafer throughput have yet to be resolved. As discussed previously, standard EBL processes use single electron sources for patterning resist. As a result, the single electron source must scan the wafer to achieve pattern definition. This serial process is highly time-consuming for simple patterns, and even more so for complex patterns.

One of the potential solutions for the low throughput problem is the use of a parallel digitally addressable field emitter array (DAFEA) as a multiple source EBL system. This type of structure is the foundation for the concept of Digital Electrostatically focused e-beam Array direct-write Lithography (DEAL)[107] in which multiple field emission cathodes are fabricated in a massively paralleled array for use as a maskless EBL system.

The current DEAL device design is centered around the use of vertically aligned carbon nanofiber (VACNF) field emission cathodes for the electron sources. The use of carbon nanostructures for field emission applications[107,110-113] has proved to be quite a fruitful research area since the discovery of carbon nanotubes[114] in 1991. Carbon nanofibers are related to carbon nanotubes, but can be deterministically grown in arrays by standard photolithographic processes. VACNFs also possess high geometric field enhancement factors by the nature of their small tip radii. These properties coupled with the ability of massive production, make VACNFs very attractive for use as the FE source for DEAL devices. In pursuit of DEAL goals, VACNF-based triode structures were fabricated and successfully operated to demonstrate electrostatic focusing.[115] In addition to beam focusing, VACNF-based triodes have been produced[110] and used[108] to pattern lines in PMMA. Figure 5-1 is an illustration of a VACNF-based DAFEA triode structure for use in the DEAL concept.

The purpose of this chapter is to describe experiments in which an EBID-based DEAL device repair scheme was developed. Prior to performing an actual triode device repair, several experiments were carried out using a microfabricated gated cathode and an EBID emitter. The results of this the gated cathode and the triode (DEAL) device repair will be discussed in the following sections.

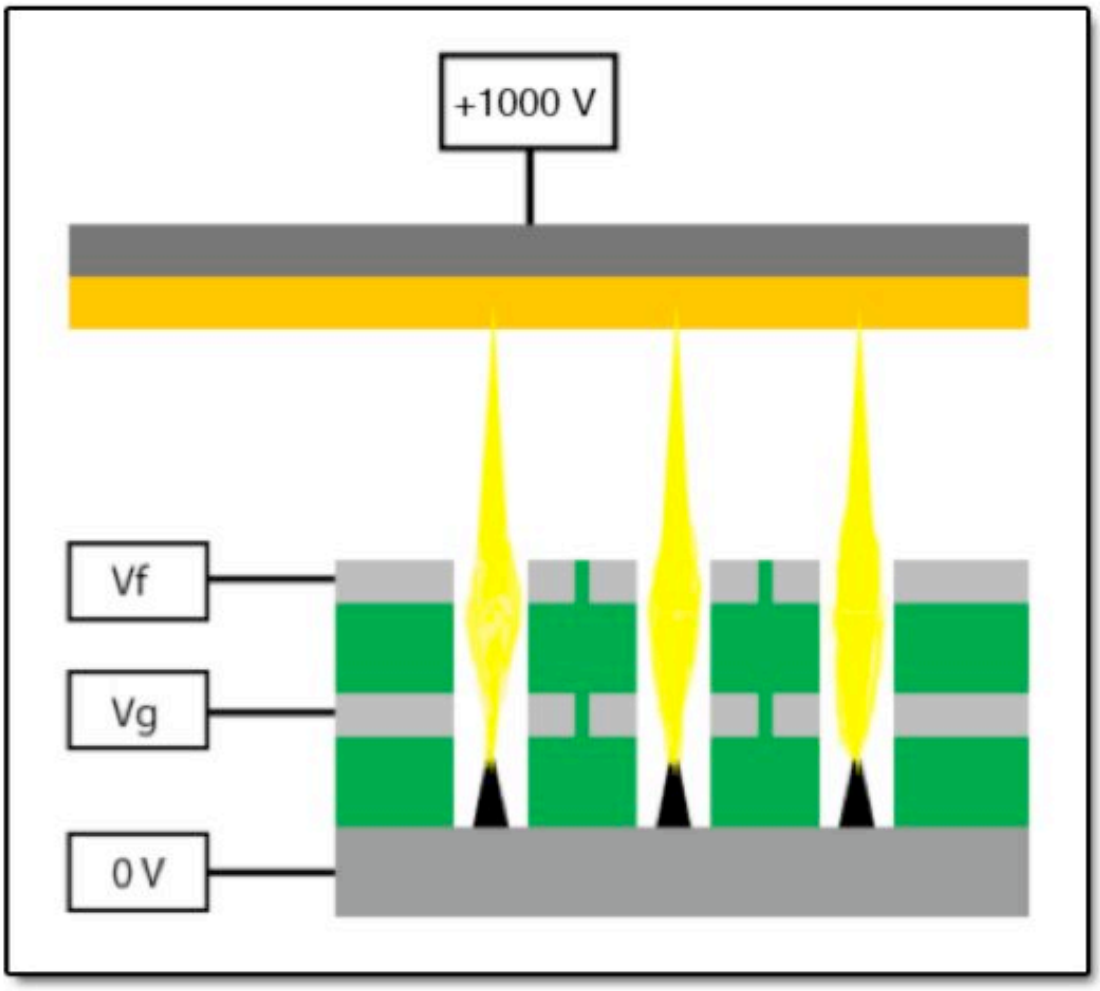

Figure 5-1: Illustration of DEAL Concept and Device Operation

An illustration showing a parallel DAFEA array as applied in the DEAL concept. Applying an extraction voltage, V_g, to the gate electrode, controls emission from CNF cathodes. The extracted electron beam is then focused on the anode by application of a focus voltage, V_f, at the focus grid. For EBL purposes, the anode is a PMMA-coated substrate 100 μm from the device.

5.2 Background and Relevant Literature

The VACNF growth process is controllable[116] on an average basis, but there can be significant fiber to fiber variation due to localized plasma deviation during the growth process. As a result, many nanofibers may be damaged, displaced, or absent subsequent to the growth process. Consequently, an important aspect of the DEAL lithography configuration is to account for the possibility of bad emitters or emitter degradation. While the current design redundancy allows for a limited number of bad emitters, there is still a need for a technique to repair or replace bad emitters. Since DEAL device fabrication involves the use of a self-aligned process[110] as shown in Figure 5-2 in which the nanofiber is deposited in the early stages of fabrication, the repair process must occur post-fabrication and inspection. This is a highly restrictive requirement, which necessitates the use of a direct-write fabrication process.

As described in Chapter 1, electron beam-induced deposition (EBID) is a direct-write technique that has the capability to deterministically grow high aspect ratio nanostructures by irradiation of a stationary point on a substrate during deposition. In addition, a wide array of metals and semiconductors such as cobalt[17], carbon[34], silicon[28], and tungsten[43] can be deposited by EBID. Consequently, one of the more commonly reported applications of EBID materials has been in the area of FE device fabrication. Therefore, EBID is ideally suited for FE device repair and, hence, DEAL device repair.

While the concept of using EBID for FE device repair is novel, its use in the deposition of field emitting materials is well documented. The FE properties of gold and

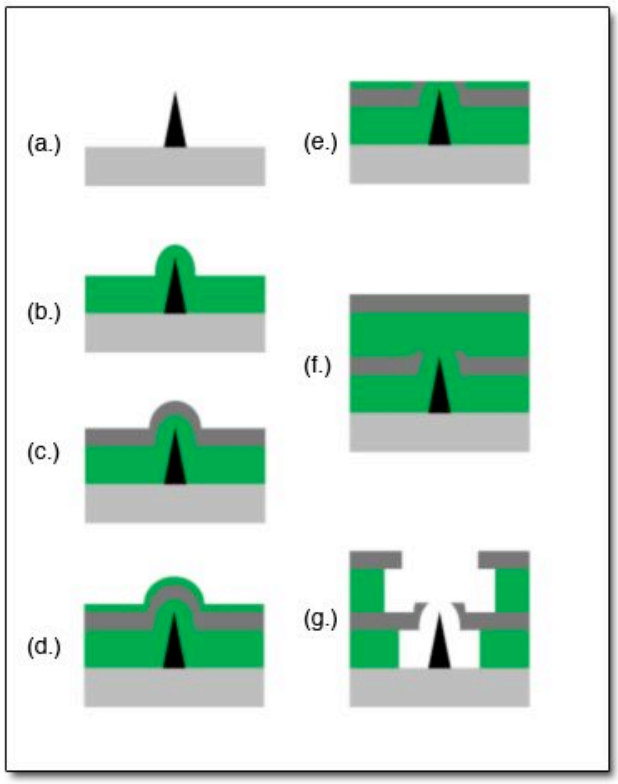

Figure 5-2: Illustration of DEAL Self-Aligned Fabrication Process

An illustration showing the fabrication process for DEAL self-aligned triode devices. Beginning with a silicon wafer with patterned CNF (a.), a conformal SiO_2 layer is grown by PECVD (b.). The wafer is then coated with the gate metal (c.) and with an additional thin sacrificial SiO_2 layer (d.). A chemical mechanical planarization is performed to expose the metal bump, which is subsequently etched by RIE (e.). An additional SiO_2 layer is deposited, followed by the focus electrode metal (f.). Finally, the focus aperture is patterned and etched (g.).

platinum nanostructures deposited by EBID have probably been investigated more thoroughly than any other EBID materials. Koops *et al*. reported on the FE characterization of EBID gold tips with tip radii of less than 7 nm.[44] Schobler *et al*. reported that gold EBID tips showed Fowler-Nordheim behavior and excellent temporal stability when coupled with an ion mirror. The emission sites were shown to undergo a forming process in which multiple sites eventually converged to a single point.[117]

Field emission properties of platinum tips were reported in a device fabricated solely by EBID.[45] In this work, EBID was used to deposit an insulating SiO_2 aperture, followed by EBID deposition of a platinum extraction grid. A platinum nanofiber emitter was then grown in the aperture and the gate was connected to an electrical lead by means of an EBID platinum wire (refer to Figure 1-4). These devices exhibited Fowler-Nordheim behavior indicating field emission from the platinum tip.[45] More recently, platinum EBID nanostructures were used as FE cathodes for planar microtriode arrays.[46]

5.3 Experimental

The general experimental parameters and techniques used for the following experiments are covered in Chapter 2. Therefore, this section only outlines the experimental details specific to this chapter such as choice of EBID precursor and FE device test chamber setup and operation.

While EBID has been used to produce gold and platinum field emitters, tungsten field emitters have not been thoroughly investigated. The availability of tungsten

precursor, as well as prior experience with tungsten deposition made it a logical choice for these experiments. Earlier EBID deposition of field emitters employed organometallic precursors and resultant metal deposition was highly contaminated with carbon and oxygen.[55,118] A non-organometallic EBID precursor, WF_6, has been shown to result in less contamination and a much higher metallic content in the deposit.[14,32] In addition to the deposit purity issues, WF_6 has other advantages over $W(CO)_6$ for EBID tungsten deposition. Tungsten hexacarbonyl is a solid at room temperature and pressure, which has a prohibitively low vapor pressure. Use of $W(CO)_6$ typically requires heating to achieve desirable vapor flow rates and consequently suffers from the problem of downstream condensation of $W(CO)_6$. On the contrary, the boiling point of WF_6 is 17.5^{o}C, which mitigates condensation problems. The ability to achieve high flow rates and high pressures of WF_6 is necessary for the high deposition rates required to produce high aspect ratio, sharp tips.

The SEM was operated in point mode for deposition of EBID field emitting nanostructures. In order to deposit optimal FE structures, the operating conditions were chosen as to produce high aspect ratio, sharp, metallic tips. Typical conditions used for depositing this type of feature are high pressure, high beam energy, and low beam current. Operating conditions for depositing FE reported here were a chamber pressure of approximately 8 mPa, a beam energy of 20 keV, and a beam current of ~33 pA. Detailed operation of the EBID setup is provided in Chapter 2.

Finished FE device testing was performed in a custom-built vacuum chamber with electrical feedthroughs. The finished devices were wire-bonded onto custom-made

printed circuit board packages and loaded into the vacuum chamber, which was pumped to a base pressure of less than 0.1 mPa. Four Keithley Instruments source-measurement units, model 2400 and 237, were used and individually connected to the cathode, the gate electrode, the focus electrode and the anode of the triode as shown in Figure 5.1. In the case of gated cathode testing, there is no focus electrode—only a gate, cathode, and an anode. In this FE test setup, the anode was a copper collecting plate that was placed approximately 6.7 mm away from the device. During the FE testing, all parallel gate electrodes except the one under examination were connected together with the common cathode. The gate that was being tested was grounded, the anode was set at +1,000 V potential, and the cathode was negatively biased from -60 V to -250 V. When applicable, the focus electrode was set at ground potential for this initial FE test. All field emission measurements were done at room temperature.

The lithography test bed as previously described[108] consisted of a modified JEOL 5D-II EBL system in which the electron column was removed. The triode devices can be mounted on a motorized stage equipped with fiber-optic displacement sensors for accurate positioning. Four Keithley 237 SMUs were used to control/monitor the triode devices. PMMA-coated glass substrates for lithography testing were loaded into the system using the standard JEOL 5D-II cassettes. In an arrangement similar that shown in Figure 5-1, the device chip was lowered to approximately 500 μm above the substrate. During writing, the cathode was operated at -500V with respect to the glass substrate.

5.4 Results and Analysis—EBID for FE Device Repair

Initial FE testing of EBID nanostructures was performed by depositing nanofibers in a gated cathode device fabricated specifically for this purpose. While the ultimate goal of this work is to demonstrate DEAL device repair, it was necessary to determine the FE properties of the EBID nanofibers in a more controlled device. Therefore, an empty gated cathode device was fabricated so that the EBID emitter could be deposited as the final step of fabrication. Gated cathode fabrication was performed on 100 mm diameter, device quality, low resistivity, n-type silicon wafers (Figure 5-3a). A one μm SiO_2 film was deposited onto the silicon substrate using a silane-based RF PECVD process (Figure 5-3b). The wafer was then metallized with 150 nm of molybdenum deposited by electron beam evaporation (Figure 5-3c). The gate apertures were then defined using photolithography and a reactive ion etch (RIE) was performed to etch the aperture pattern through the Mo film back to the oxide layer (Figure 5-3d). The structures were then immersed in a dilute solution of hydrofluoric acid in order to remove the oxide and form the apertures. The resultant gated structure had a 1.5-μm-diameter gate aperture opening and was approximately one micron deep. In addition, electrodes were patterned and etched into the molybdenum gate layer by photolithography and RIE.

The final step of fabrication was the deposition of tungsten nanofibers by EBID at the center of each aperture (Figure 5-3e). Emitters were deposited in the gated apertures using a 20 kV accelerating voltage and a beam current of approximately 33 pA. The SEM was focused at a working distance of 14.1 mm, and the vapor injector needle was

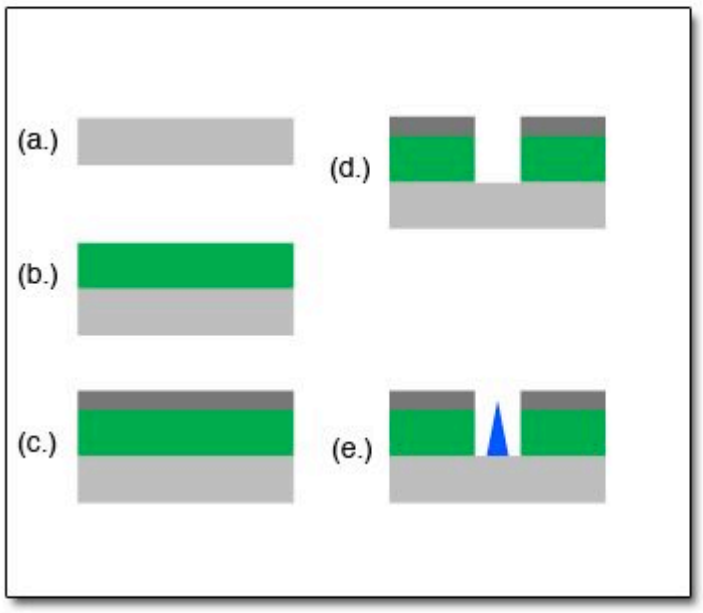

Figure 5-3: Illustration of EBID Gated Cathode Fabrication Process

An illustration showing the microfabrication process flow for EBID-emitter-based gated cathode devices. Initially, an n-type silicon wafer (a.) is topped with a one-micron silicon dioxide thin film (b.) by PECVD. The wafer is then metallized with molybdenum (c.). Photolithography is then used to pattern the aperture, which is subsequently etched by a combination of RIE and wet etching (d.) Electrodes are photolithographically defined (not shown), and EBID is used to deposit a tungsten emitter in the aperture (e.).

positioned 1 mm above the surface and 1 mm laterally from the deposition spot using the method described in Chapter 2. Once the growth rate is calibrated for the specific EBID growth conditions, the growth rate is stable to ~ 5% so the nanofiber height can be controlled within ~ 50 nm of the targeted 1-μm tall fibers. The deposition time was varied between 60 and 90 seconds and the magnification used was ×30,000 in point analysis mode. Figure 5-4 shows representative images of the finished gated cathode structure with EBID tungsten nanofiber emitters. The resultant tungsten nanofibers were ~1 μm tall, 40 nm in diameter, and had tip diameters of less than 15 nm. As evidenced by the micrographs in Figure 5-4, the high aspect ratio (~25:1) nanofibers were well registered to the 1.5-μm diameter apertures. Twelve fibers were deposited, and the measured average radial offset was 80 nm with a standard deviation of 40 nm. The offset is due in large part to the fact that the alignment was performed at a magnification of only ×10,000 as dictated by the aperture size. In addition to acceptable registry, these micrographs also show the quality of this process–it was deterministic and there were no observable defects in the devices.

In order to investigate the FE characteristics of the EBID nanofiber, the chip was packaged and tested as outlined in the previous section. In the test setup, the anode was held at +1,000 V and the gate was grounded, while the anode current was recorded as a function of the cathode voltage. A typical I-V curve and the associated Fowler-Nordheim plot are shown in Figure 5-5. The anode current shows linear fit when plotted in Fowler Nordheim coordinates, indicating cold field emission. The data presented in Figure 5-5 is shown as collected and no noise-reduction averaging was performed.

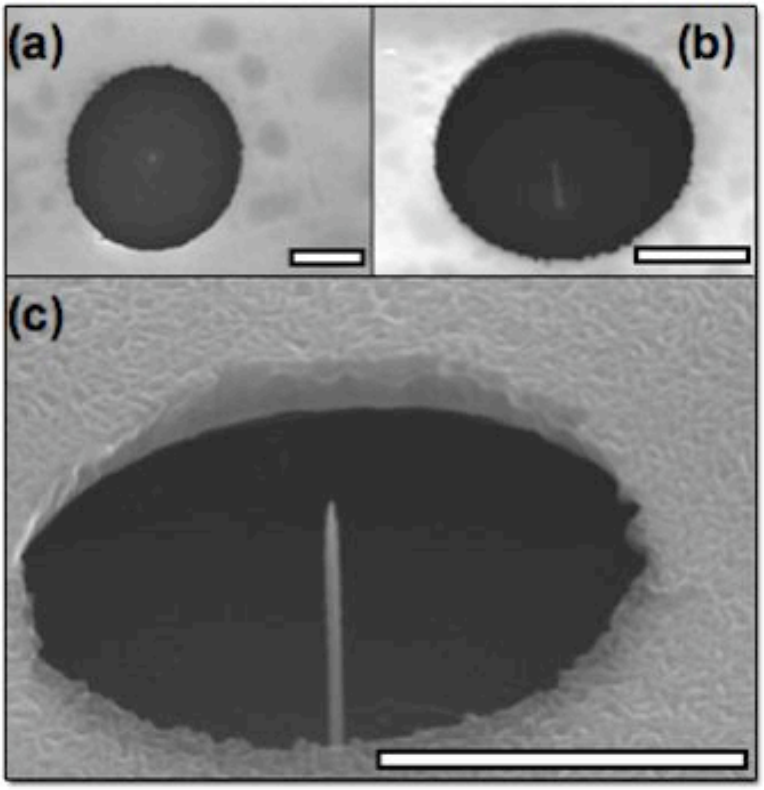

Figure 5-4: Electron Micrographs of EBID-Based Gated Cathodes

SEM micrographs of completed EBID gated cathode devices. Image (a.) was taken at normal beam incidence. Image (b.) is an oblique angle micrograph taken at 45^{o} incidence angle. Image (c.) is a close-up image of a finished device. All scale bars are 1 μm.

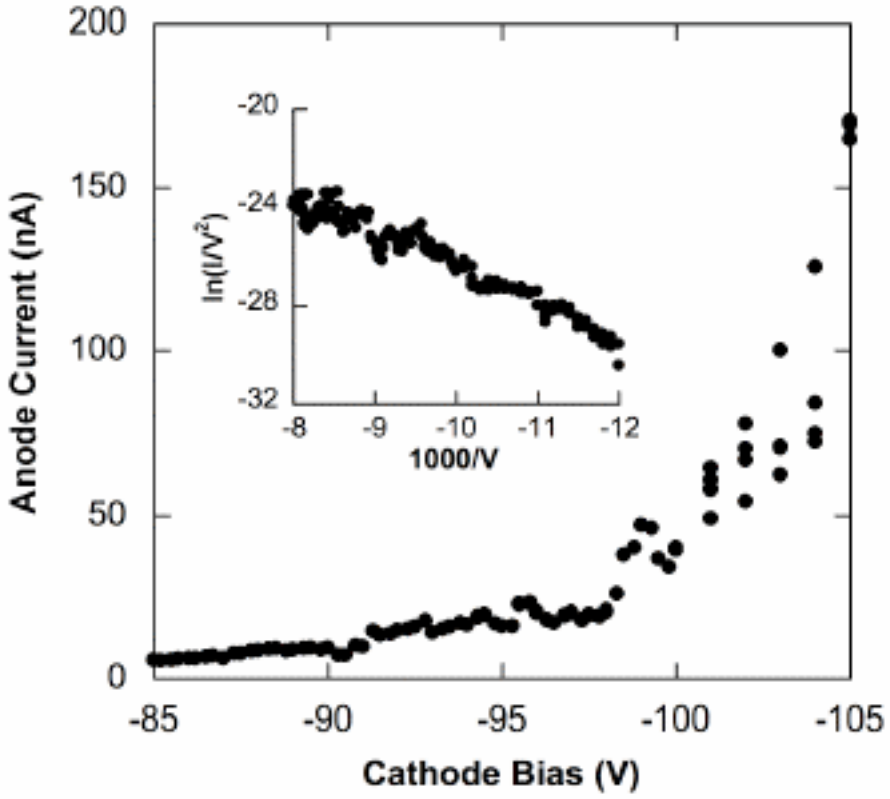

Figure 5-5: Field Emission I-V Curve for EBID-Based Gated Cathode

A plot of the current-voltage response of a gated cathode with an integrated EBID tungsten emitter. The inset plot is the same data plotted in Fowler-Nordheim coordinates, exhibiting linearity, and indicating field emission.

The threshold voltage (defined as the amount of negative voltage biased on the cathode with respect to the gate required to yield 20 nA of current) was initially around 130 V, and then dropped to 90 V within a few minutes. A drop in threshold voltage or increase in emission current after FE initiation has been previously observed with similar devices.[113] The high initial threshold voltage is possibly due to contamination of the tungsten tips. The threshold voltage after initiation is similar to other devices reported[110] considering the aperture diameter. Due to the wide aperture opening, the emission current collected by the gate less than 5%. It is also worth noting that a current as high as a few μA was extracted from a single 15 nm W tip without device failure.

The temporal stability of the EBID nanofiber cathode was also examined. The results of this experiment are shown as a plot in Figure 5-6. This data was produced by recording the cathode voltage necessary to maintain 40 nA of emission current. In accordance with previous studies[119], the cathode voltage fluctuation of ±10% as shown in Figure 5-6 may be due in part to the operation in moderate vacuum conditions. It has been reported that high temperature heating or flashing to eliminate adsorbed species may reduce this noise.[120,121]

Although the voltage (or current) amplitude appeared noisy, the beam spot as observed on a phosphor anode indicated that the beam maintained constant position when the cathode was operated at constant current. Dramatic changes in the total emission current (an order of magnitude or more) caused the beam spot on the phosphor anode to shift and change in brightness—an effect that occurred more frequently at high current. This is an indication that as the emission current changes, emission position from the tips

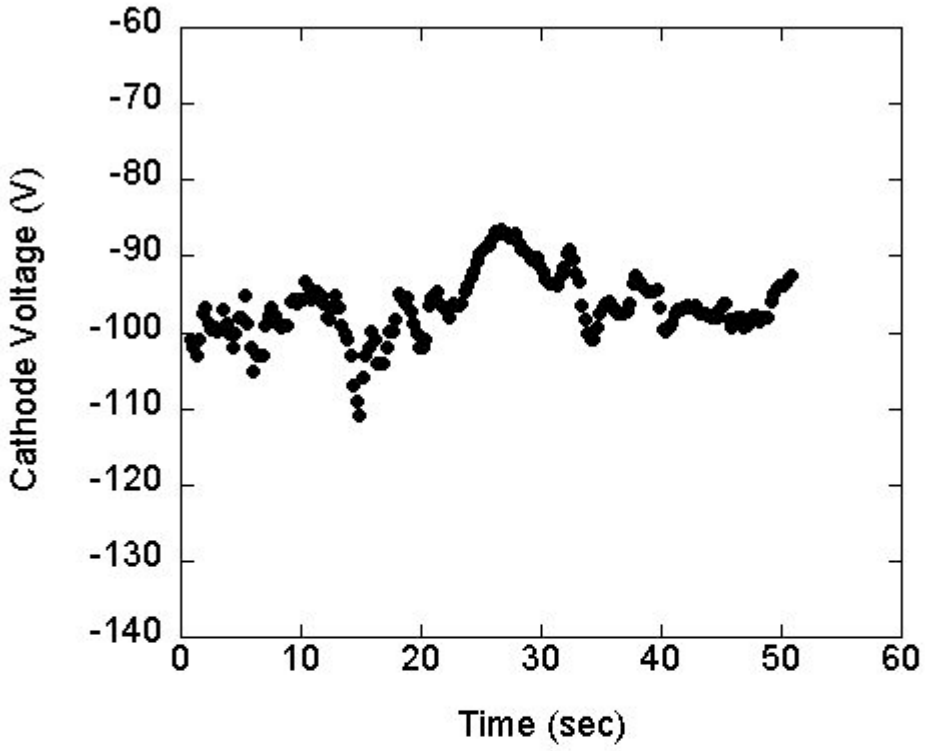

Figure 5-6: Temporal Stability of EBID-Based Gated Cathode

A plot of the temporal behavior of a gated cathode with an integrated EBID tungsten emitter. The data indicates the cathode voltage required to maintain 40 nA of emission current as a function of time.

changes, as well as the total emission area. This type of variation will result in blurred/distorted lines written by focusing triodes (DEAL devices). Fortunately, this change in emission area is not observed at emission currents below 40 nA. This is because at low macroscopic fields, only a limited emission area can be activated. For massively parallel EBL applications such as DEAL, the devices are operated at low emission current, so the emission area is approximately constant. Furthermore, a dose control circuit can be employed so that current fluctuations can be minimized.

Subsequent to characterizing the EBID tungsten nanofiber gated cathodes, the use of the technique to repair DEAL devices was then investigated. In order to do so, several triode device chips with missing or damaged CNF were loaded into the EBID SEM setup as described in Chapter 2. Figure 5-7a is an electron micrograph of one such device, in which the CNF emitter was absent.

An EBID deposition process identical to that used in the gated cathode experiments was employed to deposit tungsten nanofibers in the defective devices. The EBID conditions consisted of a 20 keV beam, 33 pA beam current, and an ambient chamber pressure of 8 mPa. Figure 5-7b is an electron micrograph of the device following nanofiber deposition, and Figure 5-7c is a tilted view of the same device. It is important to note that the geometry of the tungsten emitter as deposited in the triode device was inferior to that shown in Figure 5-4. This is almost certainly attributable to reduced WF_6 flow into the deeper triode aperture. While the depth of the diode device is only 1 μm, the triode device is 2 μm deep, resulting in degraded mass transport to the bottom of the aperture.

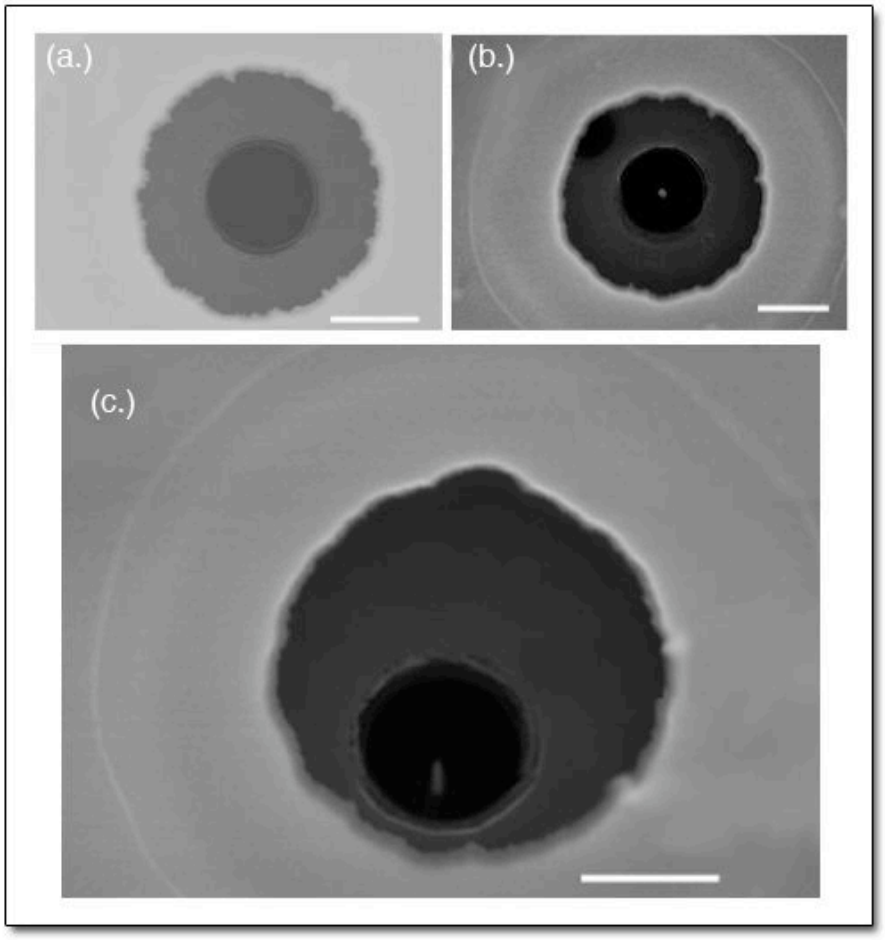

Figure 5-7: Electron Micrographs of EBID-Repaired DEAL Devices

Electron micrographs showing (a.) the finished DEAL structure with a missing nanofiber; (b.) a normal view of the device structure after a tungsten nanofiber was fabricated by EBID; (c.) a 20^{o} tilted view of a tungsten nanofiber inside the repaired device. All scale bars are 1 μm in length.

Following the EBID-based DEAL device repair, the chip was wire-bonded to the previously described test package. The packaged device was then loaded into the FE test chamber to verify that the device would field emit. The device was operated in the same manner as the gated cathode, with exception to the focus electrode (which does not exist on the gated cathode). The cathode voltage was swept, while the focus and gate electrodes were held at zero volts. The copper anode was again held at +1000 V during the device operation. The results of the field emission testing are shown in Figure 5-8. The tungsten nanofiber did indeed field emit as evidenced by the linearity of the Fowler-Nordheim plot shown in Figure 5-8b. The repaired devices demonstrated good longevity and were able to perform continuously for hours and repeatedly over days in relatively low vacuum (~10^{-4} Pa).

The purpose of a DEAL device is to perform lithography; as such, the repaired device should be capable of patterning resist with similar effectiveness to the CNF-based structures. Consequently, the repaired devices were tested for their ability to pattern PMMA. The chip was loaded into the modified EBL system described in the previous section. The nanofiber chip was positioned 500 μm above the substrate during the patterning, and the cathode was operated at -500 V with respect to the PMMA-coated glass substrate. A series of lines were written on the substrate, each using a different focus electrode voltage. Figure 5-9 is an optical micrograph of the resulting line patterns after development. There were 5-volt increments in the focus voltage between each line; the decrease in the linewidth from top to bottom reflected better focusing of the electron beam at higher focus voltages.

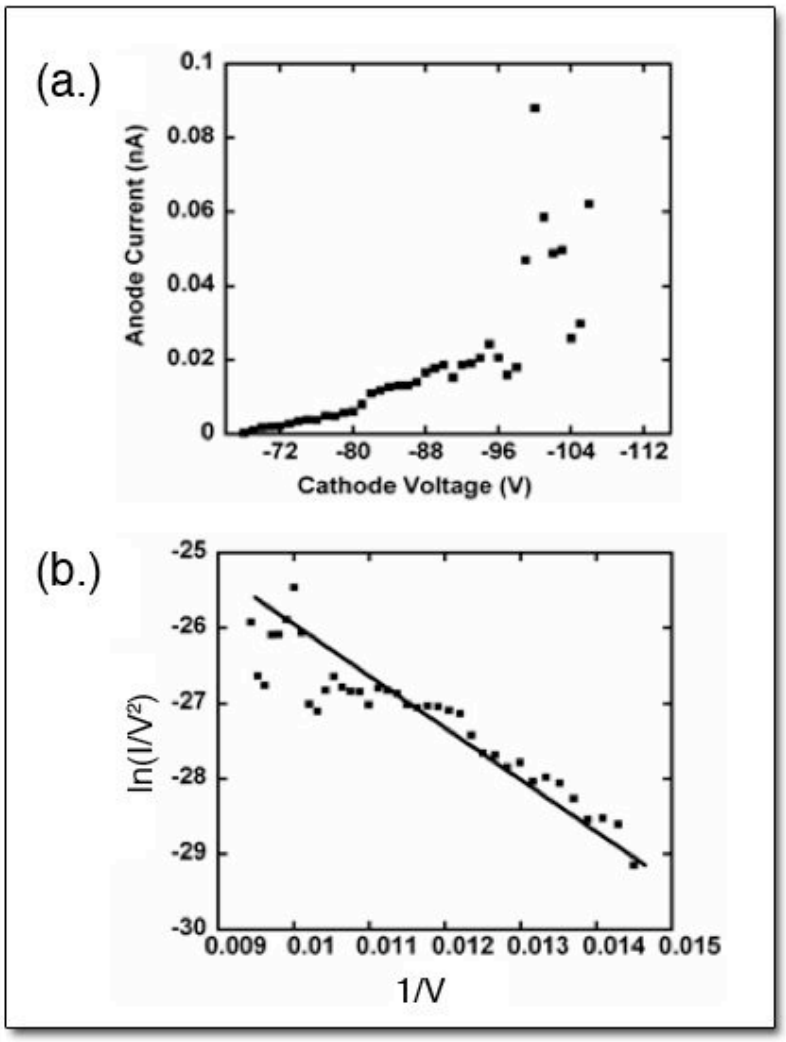

Figure 5-8: Field Emission I-V Behavior for EBID-Repaired DEAL Device

Plots showing the field emission I-V characteristics of a DEAL device following EBID repair. The standard I-V response is shown (a.), as well as the same data plotted in Fowler-Nordheim coordinates (b.).

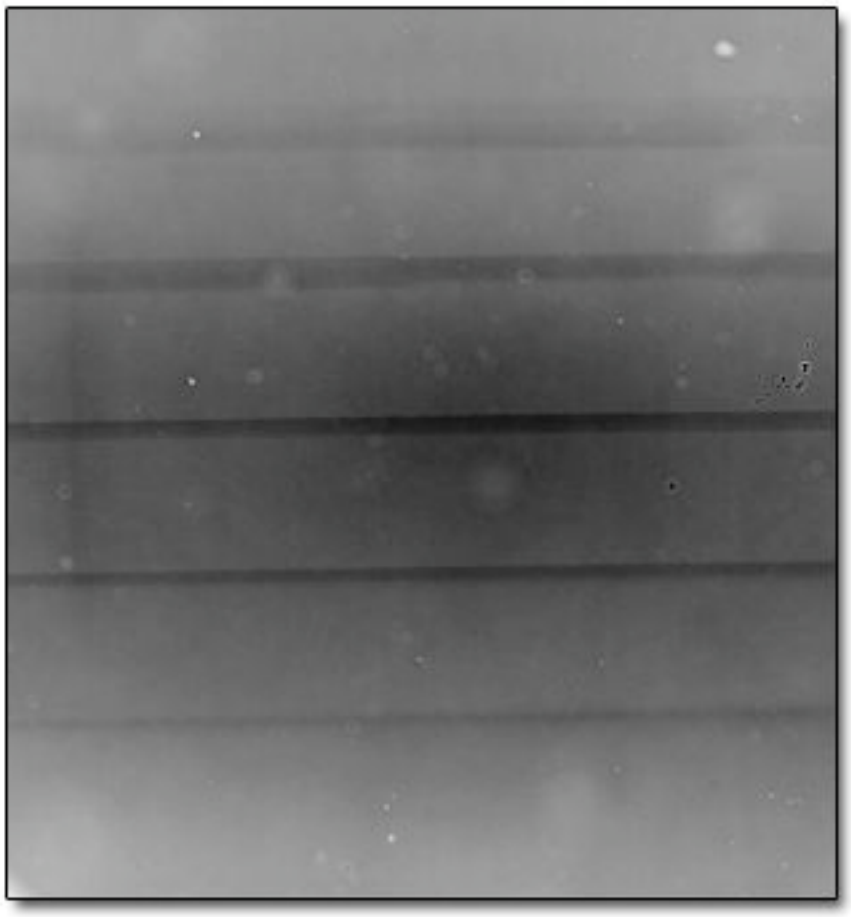

Figure 5-9: Optical Image of EBL Results Using EBID-Repaired DEAL Device

Optical micrograph of lines patterned in PMMA by direct writing from EBID-repaired DEAL device. Each line represents a 5 V increment in the focus electrode voltage. For visual reference, the bottom line has a linewidth greater than 1 μm. The image was inverted in order to increase the pattern visibility.

The best linewidth obtained was greater than one micron—a dimension that is comparable to that produced by the CNF-based DEAL devices, but significantly greater than desired. Therefore, while EBID can be used to repair DEAL devices, their current design limits the highest attainable resolution. For that reason, some fundamental changes in design are necessary improve upon the DEAL lithography process resolution. Coincidentally, the capabilities of EBID may allow for redesign of some facets of DEAL devices that could improve resolution. Discussion of this subject is reserved for the following section.

5.5 Summary and Future Work

The current DEAL parallel EBL system is a CNF-based FE array in which damaged CNF cathodes frequently occur. Damaged or missing emitters are very common, so there is a need for a repair process. There are strict fabrication limitations on the repair process as the repair must be deterministic and able to be performed on a completed device. Direct-write EBID is an ideal nanofabrication technique that satisfies these requirements, and as a result, EBID-based repair techniques were developed, characterized, and tested.

Due to familiarity and availability of precursor, tungsten was chosen as the material to be used for EBID-based repair. The need for high aspect ratio structures with sharp tips indicated that very high growth rates would be necessary. The simplest method of increasing growth rates is to simply increase the precursor flux at the beam

interaction point in the case of a mass transport limited growth. For this reason, WF_6—a liquid at room temperature and pressure—was chosen over $W(CO)_6$, which is a solid with a very low vapor pressure under the same conditions. The relatively high vapor pressure of WF_6 allowed for increased vapor flux at the surface as opposed to the solid $W(CO)_6$, resulting in high deposition rates. Additionally, WF_6 contains no carbon and oxygen, and is therefore subject to less contamination and, consequently, lower resistivity deposits.

Prior to repairing actual DEAL devices, the FE properties of the tungsten nanostructures were determined in a gated cathode structure that was fabricated specifically for this characterization. The gated cathode device was approximately one micron deep with a 1.5 μm diameter aperture opening. Tungsten EBID nanofibers were deposited in the apertures and were well registered to the device. The I-V response of the devices during vacuum FE testing indicated stable, cold field emission from the EBID cathodes. The emission threshold voltage was shown to decrease from -130 V to -90 V after a short initiation period. These results were comparable to the I-V response of CNF-based DEAL devices.

Following FE characterization of the EBID gated cathode, an actual DEAL device repair was attempted. The device used to demonstrate repair had a missing CNF emitter, but was otherwise identical to functioning DEAL structures. The gate electrode aperture was approximately 1 μm in diameter and the focus aperture diameter was approximately 2.5 μm. Prior to performing lithography, the FE characteristics of the triode were verified and shown to be stable for extended periods of operation. Finally, lithography was performed using the repaired device to write a series of lines in PMMA with variable

focus voltage. Successful focusing of the beam with increased focus voltage was evident in the patterned and developed PMMA. While the best linewidth of greater than 1 μm was comparable to that produced with CNF-based DEAL devices, the result is far from the ultimate linewidth required of parallel EBL systems.

Simulations and analysis have recently shown that these discouraging results are likely due to limitations in the current DEAL design. A more effective electrode configuration has not been implemented due to incompatibilities with available microfabrication procedures. By placing the FE cathode in a conducting well, the equipotential lines can be modified in such a way as to produce a self-focusing effect. To aid visualization of the electrode arrangement, Figure 5-10 is included to show the differences between a standard DEAL triode and the "suppressor" triode design. As shown in Figure 5-10, the fundamental difference is that the suppressor device has an emitter that is shielded by the surrounding silicon well. Numerical simulations of the two configurations have shown the advantages and disadvantages of both.

The results of simulations performed in FlexPDE® to calculate the electric potential in the devices is shown in Figure 5-11. Simulation of both the standard triode and the suppressor devices has shown that the emitter placement in the recessed well has major effects on the equipotential lines. The first of these effects relates to the ability of the suppressor to focus more effectively. As shown in Figure 5-11, the equipotential lines cannot penetrate the conducting materials, so that their behavior at the tip is quite different from the standard configuration. In the case of the triode configuration, the electric field penetrates the insulator so that the equipotential lines wrap around the tip

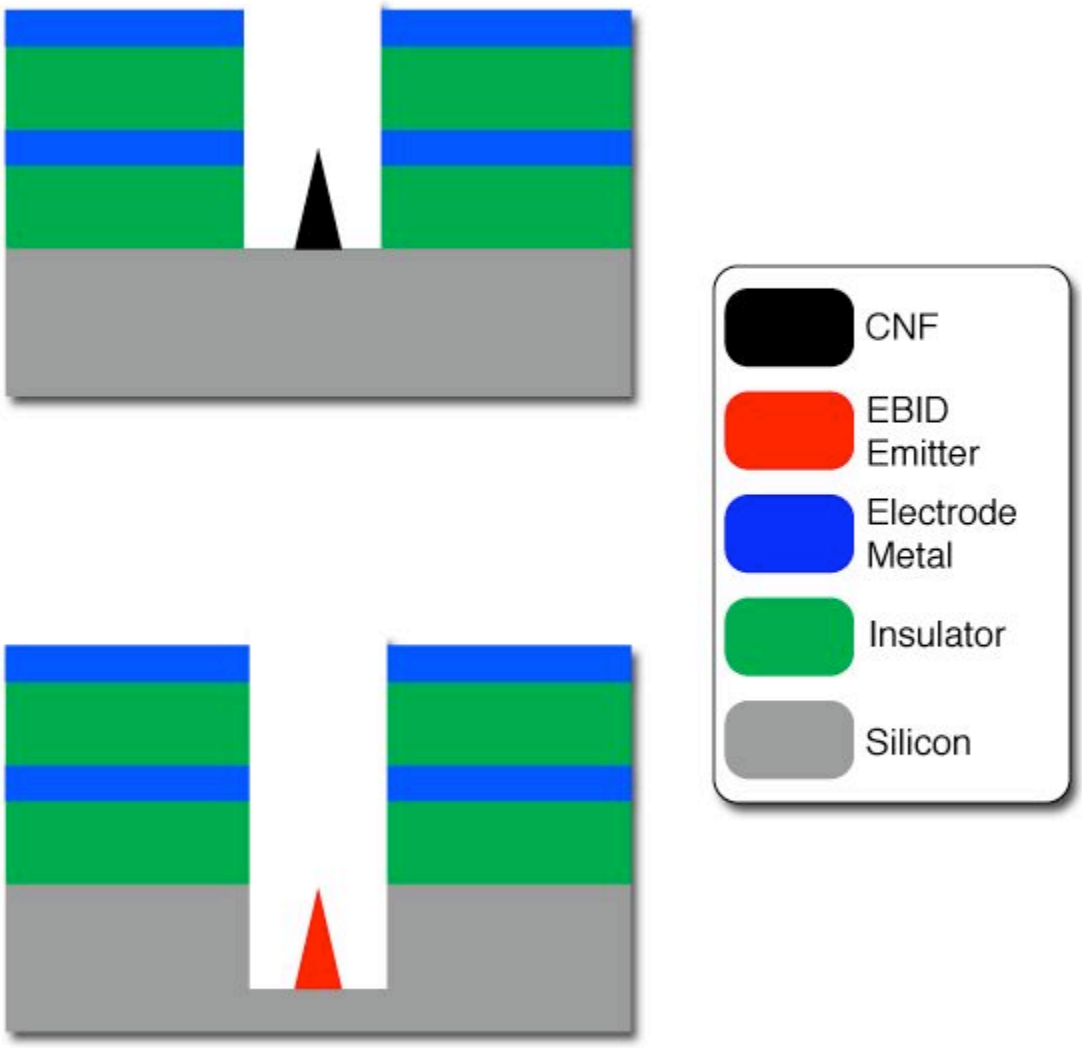

Figure 5-10: Illustration of Standard and Suppressor DEAL Configurations

Illustrations of the standard DEAL triode configuration (top) and the proposed suppressor configuration (bottom). Placement of the emitter in a conducting well as in the suppressor device changes the equipotential lines to reduce the divergence of the emitted electron beam.

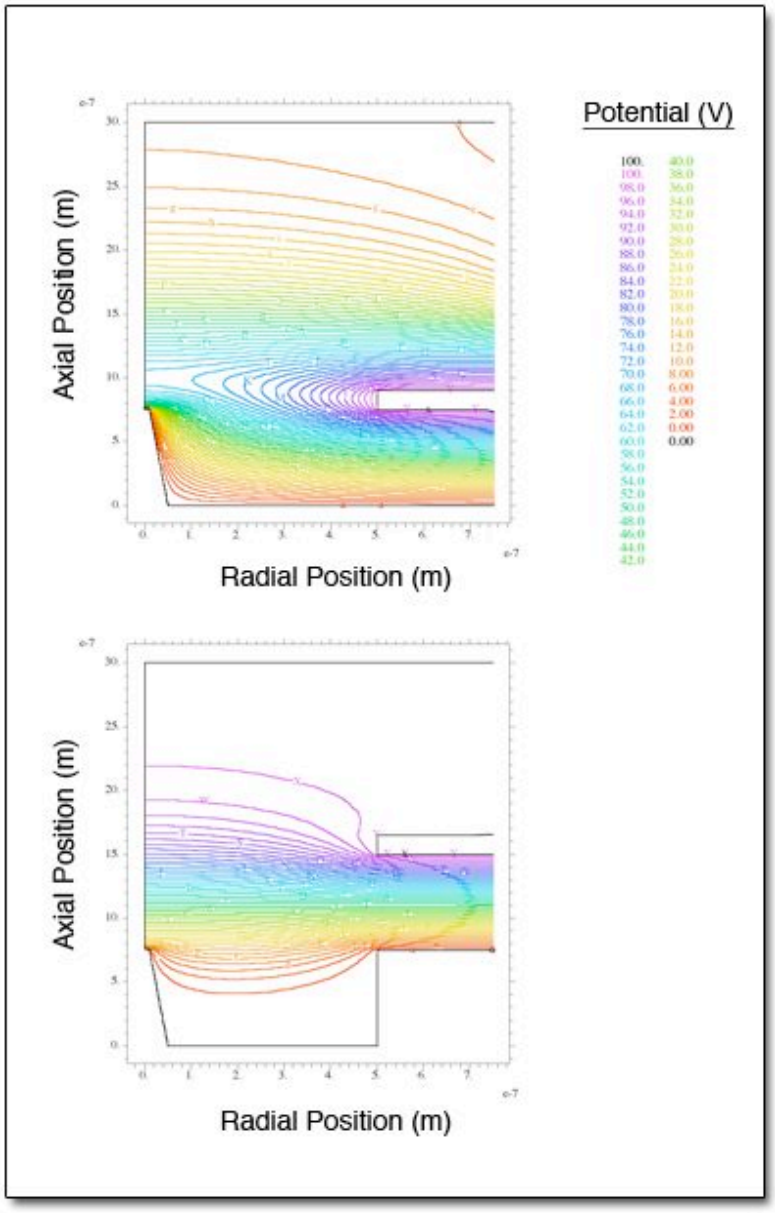

Figure 5-11: Simulated Potential in Standard DEAL and Suppressor Devices

Contour plots depicting the equipotential lines in biased, standard DEAL devices (top), and the proposed suppressor geometry (bottom). The reduced curvature of the equipotential lines for the suppressor results in a less divergent beam and improves focus.

very sharply (top of Figure 5-11). In contrast, the suppressor forces the equipotential lines to curve around the silicon well so that the lines do not curve so sharply around the tip. Electron trajectory simulations have shown that electrons emitted from the nanofiber are less spatially divergent in the suppressor due to this effect.

While the suppressor geometry provides substantial focus improvement, it is not without penalty. From Figure 5-11, it can be seen that the density of equipotential lines at the tip of the nanofiber is much higher for the standard triode device. In physical terms, this corresponds to higher electric fields at the tip of the triode device as compared to the suppressor. The consequence of the reduced fields at the tip is that higher voltages are required to initiate emission in the suppressor device. Unfortunately, the PECVD SiO_2 breaks down at the fields required to obtain emission. Therefore, high quality thermal SiO_2 must be used in order for the suppressor to function without dielectric breakdown occurring.

The need for thermal SiO_2 places stringent requirements on possible fabrication schemes for the suppressor geometry and requires that the conducting well be etched back through the oxide and into the silicon. Therefore, the CNF growth process, which involves catalyst placement on the silicon substrate, is not compatible with the suppressor fabrication scheme. In addition, the shielding that is responsible for the improved focusing of the suppressor also prevents the growth of CNF in conducting wells. It was determined that EBID deposition of emitters will alleviate most of these problems and should enable the realization of the suppressor device. EBID-based suppressor devices are currently being fabricated, and will be tested in the near future.

Chapter 6—Conclusions

The phenomenon of electron beam heating (EBH) was used to explain several otherwise anomalous experimental observations associated with electron beam-induced deposition (EBID). It was shown that a reduction in surface coverage of TEOS as controlled by elevated localized temperatures reduces the EBID deposition rate. A Monte Carlo electron-solid interaction model integrated with a finite element model was used to simulate the tip temperature of a nanofiber as a function of current, beam energy, and nanofiber geometry. For typical experimental conditions, the simulation suggests that the nanofiber tip temperature decreases with increasing beam energy. Simulation results suggest that the nanofiber tip temperature depends strongly on the position of the electron interaction volume relative the radius of the nanofiber, with the maximum temperature occurring when the interaction volume radius is equal to the nanofiber radius. It was also determined by simulation that the tip temperature increases as the nanofiber height increases. According to the model, typical experimental EBID conditions are capable of generating tip temperature increases of 30 K—a temperature that was shown experimentally capable of dramatically reducing the deposition rate. The reduced deposition rate of the nanofibers at longer times and higher currents was correlated with the increased nanofiber tip temperature inherent to these conditions. These conditions result in reduced surface coverage of the TEOS precursor, which limits the growth in a mass transport limited regime. The observed energy dependence of the deposition rate was partially correlated to thermal effects, but the turn-over in the growth

rate at high-energy is not consistent with this model and may be due to a transition to a reaction rate limited process.

Based on experimental observations and simulated results—low current, high energy, and short nanostructures are conducive to low temperature and high deposition rates. Fortunately, these conditions are also favorable for high resolution EBID processing. Therefore, the thermal effects should only be significant when depositing high aspect ratio nanostructures. The strong geometric dependence of the temperature rise indicates that future EBH models should involve realistic physical representations, and future simulations of bulk heating by irradiation should incorporate surface roughness. In addition, radiative and convective heat losses should be taken into account in further EBH simulations.

Two approaches to maskless, direct-write lithography using EBID to produce ultra-thin masking layers were investigated. One of the processes (single layer) made use of directly written SiO_x features deposited from a tetraethoxysilane precursor vapor as a masking layer for an amorphous silicon thin film. The second process (bilayer) implemented a secondary masking layer consisting of standard photoresist into which a pattern—directly written by EBID tungsten from WF_6 precursor—was transferred.

The single layer process was found to be extremely sensitive to the etch selectivity of the plasma etch. Several silicon etch process parameters were explored, but the etch mask typically only survived a few seconds of plasma etching. As a result, patterns were successfully transferred into silicon, but only to a minimal depth. It is believed that the limitations of the single layer lithography process can be overcome by

optimization of the reactive ion etch process. Future experiments with the single layer process may yield more success using a better-suited dry etch system. In addition, different EBID material systems should be investigated for increased selectivity to the desired substrate or thin film material.

The selectivity problems with the single layer process necessitated a shift of focus from a single layer process to a bilayer process. The bilayer lithography technique involved the use of a secondary masking layer of photoresist on which the pattern is directly written tungsten EBID. The excellent etch resistance of tungsten in an oxygen plasma was the primary reason for choosing it as the direct-write masking layer. Several parameters were varied in order to establish an anisotropic oxygen plasma dry-development process for transferring the EBID pattern into the underlying photoresist.

Additionally, the effects of deposition parameters on the resulting bilayer pattern transfer were investigated. It was determined that electron scattering in the resist resulted in significant peripheral contamination problems, which compromised the geometry and integrity of the desired feature. A brief refractory descum plasma etch was implemented to remove the peripheral tungsten contamination prior to the development process. Etch mask survival during the descum process was found to be dependent upon the pattern receiving sufficient dose. It was also established that overexposure by either excessive current, or excessive scan time resulted in increased linewidth.

Bilayer experiments were designed in order to reduce the spatial spread of electrons in the photoresist layer and obtain minimal linewidths. The use of thin photoresist layers and low beam energies reduces the spread of electrons in the resist.

These conditions, coupled with lower dose (low current and short scan times) were used to produce lines with an average width of ~ 35 nm.

The current Digital Electrostatically focused e-beam Array Lithography (DEAL) system design consists of a parallel array of carbon-nanofiber (CNF)-based field emission (FE) devices. Damaged or missing CNF cathodes frequently occur, thus necessitating a deterministic repair process. As a result, an EBID-based repair technique—utilizing WF_6 precursor to deposit tungsten nanofibers—was developed, characterized, and tested.

Initially, the FE properties of the tungsten nanostructures were determined in a gated cathode structure that was fabricated specifically for this characterization. The gated cathode device was approximately one micron deep with a 1.5 μm diameter aperture opening. Tungsten EBID nanofibers were deposited in the apertures and were well registered to the device. The I-V response of the devices during vacuum FE testing indicated stable, cold field emission from the EBID cathodes. The emission threshold voltage was shown to decrease from -130 V to -90 V after a short initiation period. These results were comparable to the I-V response of CNF-based DEAL devices.

Following FE characterization of the EBID gated cathode, an actual DEAL device repair was performed by replacing a missing CNF cathode. The FE characteristics of the triode were verified and shown to be stable for extended periods of operation. Finally, lithography was performed using the repaired device to write a series of lines in PMMA with variable focus voltage. Successful focusing of the beam with increased focus voltage was evident in the patterned and developed PMMA. The results of both the FE testing and lithography were consistent with standard CNF-based DEAL devices.

References

[1] K. R. Hart, T.F. Kassner, and J. K. Maurin, Philos. Mag. **21,** 453 (1970).

[2] S. Matsui and K. Mori, J. Vac. Sci. Technol. B **4,** 299 (1986).

[3] P. A. Crozier, J. Tolle, J. Kouvetakis, and C. Ritter, Appl. Phys. Lett. **84,** 3441 (2004).

[4] N. Silvis-Cividjian, C. W. Hagen, P. Kruit, M. A. J. v. d. Stam, and H. B. Groen, Appl. Phys. Lett. **82,** 3514 (2003).

[5] S. Rubel, M. Trochet, E. E. Ehrichs, W. F. Smith, and A. L. d. Lozanne, J. Vac. Sci. Technol. B **12,** 1894 (1994).

[6] H. W. P. Koops, A. Reinhardt, F. Klabunde, A. Kaya, and R. Plontke, Microelectron. Eng. **57-58,** 909 (2001).

[7] K. T. K.-v. Platen and W. H. Bruenger, J. Vac. Sci. Technol. B **14,** 4262 (1996).

[8] F. Rugamas, D. Roundy, G. Mikaelian, G. Vitug, M. Rudner, J. Shih, D. Smith, J. Segura, and M. A. Khakoo, Meas. Sci. Technol. **11,** 1750 (2000).

[9] H. W. P. Koops, J. Kretz, M. Rudolph, and M. Weber, J. Vac. Sci. Technol. B **11,** 2386 (1993).

[10] K. Ueda and M. Yoshimura, Thin Solid Films **464-465,** 331 (2004).

[11] T. Hoshino, K. Watanabe, R. Kometani, T. Morita, K. Kanda, Y. Haruyama, T. Kaito, J. Fujita, M. Ishida, Y. Ochiai, and S. Matsui, J. Vac. Sci. Technol. B **21,** 2732 (2003).

[12] M. J. van Bruggen, B. van Someren, C. W. Hagen, and P. Kruit, in *The 49th International Conference on Electron, Ion, and Photon Beam Technology and Nanofabrication* (Orlando, FL USA, 2005).

[13] H. W. P. Koops, R. Weiel, D. P. Kern, and T. H. Baum, J. Vac. Sci. Technol. B **6,** 477 (1988).

[14] K. Gamo, D. Takehara, Y. Hamamura, M. Tomita, and S. Namba, Microelectron. Eng. **5,** 163 (1986).

[15] A. Ishibashi, K. Funato, and Y. Mori, J. Vac. Sci. Technol. B **9,** 169 (1991).

[16] J. Fujita, M. Ishida, T. Ichihashi, Y. Ochiai, T. Kaito, and S. Matsui, J. Vac. Sci. Technol. B **21,** 2990 (2003).

[17] Y. M. Lau, P. C. Chee, J. T. L. Thong, and V. Ng, J. Vac. Sci. Technol. A **20,** 1295 (2002).

[18] I. Utke, A. Luisier, P. Hoffmann, D. Laub, and P. A. Buffat, Appl. Phys. Lett. **81,** 3245 (2002).

[19] R. R. Kunz, T. E. Allen, and T. M. Mayer, J. Vac. Sci. Technol. B **5,** 1427 (1987).

[20] T. Takahashi, Y. Arakawa, M. Nishioka, and T. Ikoma, Appl. Phys. Lett. **60,** 68 (1992).

[21] M. Weber, H. W. P. Koops, M. Rudolph, J. Kretz, and G. Schmidt, J. Vac. Sci. Technol. B **13,** 1364 (1995).

[22] V. Scheurer, H. W. P. Koops, and T. Tschudi, Microelectron. Eng. **5,** 423 (1986).

[23] T. J. Stark, T. M. Mayer, D. P. Griffis, and P. E. Russell, J. Vac. Sci. Technol. B **10,** 2685 (1992).

[24] T. J. Stark, T. M. Mayer, D. P. Griffis, and P. E. Russell, J. Vac. Sci. Technol. B **9,** 3475 (1991).

[25] S. Wang, Y.-M. Sun, Q. Wang, and J. M. White, J. Vac. Sci. Technol. B **22,** 1803 (2004).

[26] F. Cicoira, K. Leifer, P. Hoffmann, I. Utke, B. Dwir, D. Laub, P. A. Buffat, E. Kapon, and P. Doppelt, J. Cryst. Growth **265,** 619 (2004).

[27] N. A. Kislov, I. I. Khodos, E. D. Ivanov, and J. Barthel, Scanning **18,** 114 (1996).

[28] S. Matsui and M. Mito, Appl. Phys. Lett. **53,** 1492 (1988).

[29] B. H. Chin and G. Ehrlich, Appl. Phys. Lett. **38,** 253 (1981).

[30] S. Lipp, L. Frey, C. Lehrer, B. Frank, E. Demm, S. Pauthner, and H. Ryssel, J. Vac. Sci. Technol. B **14,** 3920 (1996).

[31] W. J. Mitchell and E. L. Hu, J. Vac. Sci. Technol. B **17,** 1622 (1999).

[32] S. J. Randolph, K. L. Klein, P. D. Rack, and M. L. Simpson, (2005).

[33] V. Gopal, E. A. Stach, V. R. Radmilovic, and I. A. Mowat, Appl. Phys. Lett. **85,** 49 (2004).

[34] I. Utke, B. Dwir, K. Leifer, F. Cicoira, P. Doppelt, P. Hoffmann, and E. Kapon, Microelectron. Eng. **53,** 261 (2000).

[35] K. Molhave, D. N. Madsen, A. M. Rasmussen, A. Carlsson, C. C. Appel, M. Brorson, C. J. H. Jacobsen, and P. Boggild, Nano Lett. **3,** 1499 (2003).

[36] Z. Q. Liu, K. Mitsuishi, and K. Furuya, J. Appl. Phys. **96,** 619 (2004).

[37] M. D. Croitoru, G. Bertsche, and D. P. Kern, in *The 49th International Conference on Electron, Ion, and Photon Beam Technology and Nanofabrication* (Orlando, FL USA, 2005).

[38] T. Brintlinger, M. S. Fuhrer, J. Melngailis, I. Utke, T. Bret, A. Perentes, P. Hoffmann, P. Doppelt, and M. Abourida, in *The 49th International Conference on Electron, Ion, and Photon Beam Technology and Nanofabrication* (Orlando, FL USA, 2005).

[39] T. Liang, A. Stivers, R. Livengood, P. Y. Yan, G. Zhang, and F. C. Lo, J. Vac. Sci. Technol. B **18,** 3216 (2000).

[40] T. Liang and A. Stivers, Proc. SPIE **4688,** 375 (2002).

[41] T. Liang, D. Bald, B. Lieberman, and A. Stivers, in *The 49th International Conference on Electron, Ion, and Photon Beam Technology and Nanofabrication* (Orlando, FL USA, 2005).

[42] T. Morita, R. Kometani, K. Watanabe, K. Kanda, Y. Haruyama, T. Hoshino, K. Kondo, T. Kaito, T. Ichihashi, J. Fujita, M. Ishida, Y. Ochiai, T. Tajima, and S. Matsui, J. Vac. Sci. Technol. B **21,** 2737 (2003).

[43] S. Matsui, T. Ichihashi, and M. Mito, J. Vac. Sci. Technol. B **7,** 1182 (1989).

[44] H. W. P. Koops, C. Schossler, A. Kaya, and M. Weber, J. Vac. Sci. Technol. B **14,** 4105 (1996).

[45] K. Murakami and M. Takai, J. Vac. Sci. Technol. B **22,** 1266 (2004).

[46] J. Sellmair, K. Edinger, and H. W. P. Koops, Journal of Vacuum Science & Technology B (Microelectronics and Nanometer Structures) **23,** 781 (2005).

[47] C. Lehrer, L. Frey, S. Petersen, H. Ryssel, M. Schafer, and T. Sulzbach, J. Vac. Sci. Technol. B **22,** 1402 (2004).

[48] L. Dong, F. Arai, and T. Fukuda, Appl. Phys. Lett. **81,** 1919 (2002).

[49] F. Arai, P. Liu, L. Dong, T. Fukuda, T. Noguchi, and K. Tatenuma, in *Pure metal deposit using multi-walled carbon nanotubes decorated with ruthenium dioxide super-nanoparticles*, Munich, Germany, 2004 (IEEE), p. 196.

[50] T. Mukawa, S. Okada, R. Kobayashi, M. Ishida, T. Ichihashi, Y. Ochiai, S. Matsui, and J. Fujita, in *The 49th International Conference on Electron, Ion, and Photon Beam Technology and Nanofabrication* (Orlando, FL USA, 2005).

[51] K. L. Lee, R. R. Thomas, A. Viehbeck, and E. J. M. O'Sullivan, J. Vac. Sci. Technol. B **11,** 2204 (1993).

[52] T. Djenizian, L. Santinacci, and P. Schmuki, Appl. Phys. Lett. **78,** 2940 (2001).

[53] A. Perentes, A. Bachmann, M. Leutenegger, I. Utke, C. Sandu, and P. Hoffmann, Microelectron. Eng. **73-74,** 412 (2004).

[54] E. J. Sanchez, J. T. Krug II, and X. S. Xie, Rev. Sci. Instrum. **73,** 3901 (2002).

[55] P. D. Rack, S. Randolph, Y. Deng, J. Fowlkes, Y. Choi, and D. C. Joy, Appl. Phys. Lett. **82,** 2326 (2003).

[56] T. Bret, I. Utke, A. Bachmann, and P. Hoffmann, Appl. Phys. Lett. **83,** 4005 (2003).

[57] A. Perentes, T. Bret, I. Utke, and P. Hoffmann, in *The 49th International Conference on Electron, Ion, and Photon Beam Technology & Nanofabrication* (Orlando, FL USA, 2005).

[58] T. Djenizian, L. Santinacci, and P. Schmuki, J. Electrochem. Soc. **151,** G175 (2004).

[59] M. Shimojo, K. Mitsuishi, A. Tameike, and K. Furuya, J. Vac. Sci. Technol. B **22,** 742 (2004).

[60] Z. Q. Liu, K. Mitsuishi, and K. Furuya, J. Appl. Phys. **96,** 3983 (2004).

[61] W. F. van Dorp, C. W. Hagen, B. van Someren, and P. Kruit, in *The 49th International Conference on Electron, Ion, and Photon Beam Technology & Nanofabrication* (Orlando, FL USA, 2005).

[62] K. T. K.-v. Platen, J. Chlebek, M. Weiss, K. Reimer, H. Oertel, and W. H. Brunger, J. Vac. Sci. Technol. B **11,** 2219 (1993).

[63] N. Silvis-Cividjian, C. W. Hagen, L. H. A. Leunissen, and P. Kruit, Microelectron. Eng. **61-62,** 693 (2002).

[64] J. D. Fowlkes, S. J. Randolph, and P. D. Rack, in *The 49th International Conference on Electron, Ion, and Photon Beam Technology and Nanofabrication* (Orlando, FL USA, 2005).

[65] K. T. K.-v. Platen, L.-M. Buchmann, H.-C. Petzold, and W. H. Brunger, J. Vac. Sci. Technol. B **10,** 2690 (1992).

[66] H. Fujioka, K. Nakamae, M. Hirota, K. Ura, N. Tamura, and T. Takagi, J. Phys. D: Appl. Phys. **23,** 266 (1990).

[67] T. Bret, I. Utke, and P. Hoffmann, Microelectron. Eng. **78-79,** 307 (2005).

[68] Z. Q. Liu, K. Mitsuishi, and K. Furuya, Nanotechnology **15,** S414 (2004).

[69] G. Q. Xie, M. Song, K. Mitsuishi, and K. Furuya, Appl. Phys. A **79,** 1843 (2004).

[70] A. Luisier, I. Utke, T. Bret, F. Cicoira, R. Hauert, S.-W. Rhee, P. Doppelt, and P. Hoffmann, J. Electrochem. Soc. **151,** C590 (2004).

[71] T. Bret, S. Mauron, I. Utke, and P. Hoffmann, Microelectron. Eng. **78-89,** 300 (2005).

[72] M. Shimojo, M. Takeguchi, M. Tanaka, K. Mitsuishi, and K. Furuya, Appl. Phys. A **79,** 1869 (2004).

[73] D. A. Alman, D. N. Ruzic, and J. N. Brooks, Physics of Plasmas **7,** 1421 (2000).

[74] W. L. Morgan, C. Winstead, and V. McKoy, Journal of Applied Physics **92,** 1663 (2002).

[75] Y.-K. Kim, K. K. Irikura, M. E. Rudd, M. A. Ali, P. M. S. J. S. Coursey, R. A. Dragoset, A.R. Kishore, K. J. Olsen, A. M. Sansonetti, G.G. Wiersma, D.S. Zucker, and M.A. Zucker, (National Institute of Standards and Technology, 1997).

[76] J. D. Fowlkes, S. J. Randolph, and P. D. Rack, J. Vac. Sci. Technol. B (Accepted 2005).

[77] H. Hiroshima and M. Komuro, Nanotechnology **9,** 108 (1998).

[78] T. E. Madey and J. T. Yates, J. Vac. Sci. Technol. **8,** 525 (1971).

[79] M. Ohring, *The Materials Science of Thin Films*, 2 ed. (Academic Press, 2001).

[80] J. B. Hudson, *Surface Science: An Introduction* (Butterworth-Heinemann, Boston, 1992).

[81] P. B. Mirkarimi, J. Appl. Phys. **91,** 81 (2002).

[82] S. P. Hau-Riege, A. Barty, P. B. Mirkarimi, S. Baker, M. A. Coy, M. Mita, V. E. Robertson, T. Liang, and A. Stivers, J. Appl. Phys. **96,** 6812 (2004).

[83] T. R. Groves, J. Vac. Sci. Technol. B **14,** 3839 (1996).

[84] D. Chu, D. T. Bilir, R. F. W. Pease, and K. E. Goodson, J. Vac. Sci. Technol. B **20,** 3044 (2002).

[85] M. Weber, J. Phys. D: Appl. Phys. **27,** 1363 (1994).

[86] I. Utke, T. Bret, D. Laub, P. A. Buffat, L. Scandella, and P. Hoffmann, Microelectron. Eng. **73-74,** 553 (2004).

[87] D. C. Joy, Scanning Microscopy **5,** 329 (1991).

[88] L. L. Tedder, G. Lu, and J. E. Crowell, J. Appl. Phys. **69,** 7037 (1991).

[89] M. L. Wise, O. Sneh, L. A. Okada, and S. M. George, J. Vac. Sci. Technol. B **13,** 865 (1995).

[90] R. C. Bracken and S. A. Rizvi, in *VLSI Handbook*, edited by N. G. Einspruch (Academic Press, Orlando, 1985), p. 328-350.

[91] G. E. Moore, Electronics **38** (1965).

[92] H. J. Levinson and W. H. Arnold, in *Handbook of Microlithography, Micromachining, and Microfabrication*; *Vol. 1*, edited by P. Rai-Choudhury (SPIE Optical Engineering Press, Bellingham, 1997).

[93] R. K. Watts, in *VLSI Handbook*, edited by N. G. Einspruch (Academic Press, Orlando, 1985).

[94] M. J. Bowden, in *Introduction to Microlithography*, 2 ed., edited by L. F. Thompson, C. G. Willson, and M. J. Bowden (American Chemical Society, Washington, D.C., 1994), p. 19-138.

[95] M. Rothschild, Materials Today **8,** 18 (2005).

[96] R. F. Pease, Microelectron. Eng. **78-79,** 381 (2005).

[97] M. A. McCord and M. J. Rooks, in *Handbook of Microlithography, Micromachining, and Microfabrication*; *Vol. 1*, edited by P. Rai-Choudhury (SPIE Optical Engineering Press, Bellingham, 1997).

[98] S. Matsui, Applied Physics Letters **55,** 134 (1989).

[99] D. Wang, P. C. Hoyle, J. R. A. Cleaver, G. A. Porkolab, and N. C. MacDonald, J. Vac. Sci. Technol. B **13,** 1984 (1995).

[100] S. Thomas, Journal of Applied Physics **45,** 161 (1974).

[101] B. Carriere and B. Lang, Surface Science **64,** 209 (1977).

[102] P. E. Allen, D. P. Griffis, Z. J. Radzimski, and P. E. Russell, Journal of Vacuum Science & Technology A (Vacuum, Surfaces, and Films) **10,** 965 (1992).

[103] J. F. Kimball, P. E. Allen, D. P. Griffis, Z. J. Radzimski, and P. E. Russell, Journal of Vacuum Science & Technology A (Vacuum, Surfaces, and Films) **12,** 2457 (1994).

[104] T. K. Whidden, S.-J. Yang, A. Jenkins-Gray, M. Pan, and M. N. Kozicki, J. Electrochem. Soc. **144,** 605 (1997).

[105] K. Sawada, M. Ishida, T. Nakamura, and T. Suzaki, Applied Physics Letters **55,** 1636 (1989).

[106] T. Yasuda, M. Nishizawa, and S. Yamasaki, Appl. Phys. Lett. **76,** 3203 (2000).

[107] L. R. Baylor, D. H. Lowndes, M. L. Simpson, C. E. Thomas, M. A. Guillorn, V. I. Merkulov, J. H. Whealton, E. D. Ellis, D. K. Hensley, and A. V. Melechko, Journal of Vacuum Science and Technology B: Microelectronics and Nanometer Structures **20,** 2646 (2002).

[108] L. R. Baylor, W. L. Gardner, X. Yang, R. J. Kasica, M. A. Guillorn, B. Blalock, H. Cui, D. K. Hensley, S. Islam, D. H. Lowndes, A. V. Melechko, V. I. Merkulov, D. C. Joy, P. D. Rack, M. L. Simpson, and D. K. Thomas, J. Vac. Sci. Technol. B **22,** 3021 (2004).

[109] A. K. Paul, A. K. Dimri, and R. P. Bajpai, Proceedings of the SPIE - The International Society for Optical Engineering **4936,** 93 (2002).

[110] M. A. Guillorn, X. Yang, A. V. Melechko, D. K. Hensley, M. D. Hale, V. I. Merkulov, M. L. Simpson, L. R. Baylor, W. L. Gardner, and D. H. Lowndes, Journal of Vacuum Science & Technology B (Microelectronics and Nanometer Structures) **22,** 35 (2004).

[111] N. de Jonge, J. Appl. Phys. **95,** 673 (2004).

[112] Q. H. Wang, M. Yan, and R. P. H. Chang, Appl. Phys. Lett. **78,** 1294 (2001).

[113] M. A. Guillorn, M. D. Hale, V. I. Merkulov, M. L. Simpson, G. Y. Eres, H. Cui, A. A. Puretzky, and D. B. Geohegan, Applied Physics Letters **81,** 2860 (2002).

[114] S. Iijima, Nature **354,** 56 (1991).

[115] M. A. Guillorn, Thesis, University of Tennessee, 2003.

[116] A. V. Melechko, V. I. Merkulov, T. E. McKnight, M. A. Guillorn, K. L. Klein, D. H. Lowndes, and M. L. Simpson, Journal of Applied Physics **97,** 41301 (2005).

[117] C. Schobler, A. Kaya, J. Kretz, M. Weber, and H. W. P. Koops, Microelectron. Eng. **30,** 471 (1996).

[118] M. Takai, T. Kishimoto, H. Morimoto, Y. K. Park, S. Lipp, C. Lehrer, L. Frey, H. Ryssel, A. Hosono, and S. Kawabuchi, Microelectronic Engineering **41-42,** 453 (1998).

[119] V. Semet, V. T. Bihn, P. Vincent, D. Guillot, K. B. K. Teo, M. Chhowalla, G. A. J. Amaratunga, W. I. Milne, P. Legagneux, and D. Pribat, Appl. Phys. Lett. **81,** 343 (2002).

[120] R. Collazo, R. Schlesser, and Z. Sitar, Diamond and Related Materials **11,** 769 (2002).

[121] K. Hata, A. Takakura, and Y. Saito, Surface Science **490,** 296 (2001).

Appendix A

Example Matlab® Code

```
function MCSSfiber_2d

% Monte Carlo Electron Solid Interaction Simulation using Single Scattering model.
% This model will calculate the electron trajectories within an SiO2 nanopillar on a
% tungsten substrate and determine the energy deposition profile.

clear all;        % Clear the memory
close all;        % Close all open figures
clc;              % Clear the command window
tic;              % Start the calculation timer

% Define all of the global variables used in subsequent subfunctions.
global rhoS AS ZanS JS Na  rhoW AW ZanW JW swtch

%-----------------------------------------------------------------------------------------------------
% (1.) Constant definitions and matrix initializations.
%-----------------------------------------------------------------------------------------------------
colordef white          % Define the plot background color
opengl neverselect      % Set the graphics driver
ntraj=5000;             % Number of incident electrons
Eo=5;                   % Incident beam energy (keV)
Ef=.1;                  % Final electron energy (~0)
plotswitch=0;           % Plotswitch=1 will plot the interaction region
pillarad=500e-9;        % Radius of nanofiber
pillarht=100e-9;        % Height of nanofiber
pillarad=pillarad*100;    % Convert to cm.
pillarht=pillarht.*100;   % Convert to cm.
Na=6.022e23;              % Avogadro's number

% Tungsten material parameters
ZanW=74;       % Atomic Number
AW=183.84;     % Atomic Mass (g/mol)
rhoW=19.25;    % Density (g/cc)

% SiO2 material parameters
ZanS=10.81;    % Average Atomic Number
AS=20;         % Average Atomic Mass (g/mol)
rhoS=2.2;      % Density (g/cc)

% Initialize the energy and position vectors for every electron.
for ii=1:1:ntraj
```

```
    E(ii,1)=Eo;          % Initial energy
    x(ii,1)=0;           % Initial x position
    y(ii,1)=0;           % Initial y position
    z(ii,1)=0;           % Initial z position
    r(ii,1)=0;           % Initial r position
end
% Calculate the mean ionization potential in keV
JS=(9.76.*ZanS+(58.5./(ZanS.^0.19))).*1e-3;  % Loss per event (keV)
JW=(9.76.*ZanW+(58.5./(ZanW.^0.19))).*1e-3;  % Loss per event (keV)

% Initialize and seed the random number generator
rand('state',sum(100*clock));

%Initialize backscattered electron counter
back=0;

% Force the initial electron position into the SiO2 material
swtch=1;

%-----------------------------------------------------------------------------------------------------
% (2.) Monte-Carlo electron position calculations.
%-----------------------------------------------------------------------------------------------------

%Calculate trajectories and electron xyz positions.
for jj=1:1:ntraj
    % Initialize a step counter to find out how many collisions are occurring
    step_count=2;
    cx=0;       %Initial x direction cosine
    cy=0;       %Initial y direction cosine
    cz=1;       %Initial z direction cosine (cz=1 for normal beam upward)

   while E(jj,step_count-1)>=Ef

      if z(jj,step_count-1)>=pillarht
         swtch=0;   % Electron is in Tungsten
      else
         swtch=1;   % Electron is in SiO2
      end
      % Use Rutherford cross-section function to determine the step length and scattering
      % angle
      [step,phi]=rutherford(E(jj,step_count-1));
```

```
    % Direction vector calculations to determine change in electron positions.
    AM=-(cx./cz);
    AN=1./sqrt((1+(AM^2)));, V1=AN.*sin(phi);
    V2=AN.*AM.*sin(phi);
    psi=2.*pi.*rand;
    V3=cos(psi);, V4=sin(psi);
    ca=(cx.*cos(phi))+(V1.*V3)+(cy.*(V2).*(V4));
    cb=(cy.*cos(phi))+(V4.*(cz.*V1-cx.*V2));
    cc=(cz.*cos(phi))+(V2.*V3)-(cy.*V1.*V4);

    % Calculate the new electron positions after a scattering event.
    x(jj,step_count)=x(jj,step_count-1)+(step.*ca);
    y(jj,step_count)=y(jj,step_count-1)+(step.*cb);
    z(jj,step_count)=z(jj,step_count-1)+(step.*cc);
    r(jj,step_count)=sqrt((x(jj,step_count).^2)+y(jj,step_count).^2);

    % Calculate the energy lost after traversing a step
    dE=step.*funkeval(E(jj,step_count-1));
    E(jj,step_count)=E(jj,step_count-1)+dE;
    deltaE(jj,step_count)=E(jj,step_count-1)-E(jj,step_count);

    % Add one to the step counter
    step_count=step_count+1;

    % Reset the new direction cosines to the current direction cosines
    cx=ca;, cy=cb;, cz=cc;

    % Determination of electron position relative to nanopillar
    % If electron is above nanopillar top or outside nanopillar
     if (z(jj,step_count-1)<=0 & step_count~=2) | (r(jj,step_count-1)>pillarad &…
           z(jj,step_count-1)<pillarht)
        back=back+1;        % Add one to the backscattered counter
        z(jj,step_count-1)=0; % Set the final z position to zero
        break               % Break the loop if backscattered
     end % Ends if statement
  end     % Ends while statement
end       % Ends for statement

%-----------------------------------------------------------------------------------------------------
% (3.) Refine the position matrices.
```

```
%-------------------------------------------------------------------------------------------------

% The longest trajectory will define one dimension of the matrix.
[junk,mat_size]=size(z);

% Loop through each electron's trajectory
for ii=1:1:ntraj

   % Loop through every scattering event of every electron starting at number 2
   for jj=2:1:mat_size-1

      % If z position is less than or equal to the surface, the electron must
      % have been backscattered.  Or if the energy is below the final energy, the
      % electron must have stopped.
      if (z(ii,jj)<=0) | (r(ii,jj)>pillarad & z(ii,jj)<pillarht)

         % Since the electron is finished, make all of the false zero positions equal
         % to the last position in which an actual scattering event occurred.
         z(ii,jj)=z(ii,jj-1);
         x(ii,jj)=x(ii,jj-1);
         y(ii,jj)=y(ii,jj-1);
         r(ii,jj)=r(ii,jj-1);

         % Since the electron is finished, make the energy in the excess zero positions
         % equal to zero
         E(ii,jj+1)=0;
         deltaE(ii,jj+1)=0;

      end    % Ends if statement
   end       % Ends for statement
end          % Ends for statement

% Calculate the backscattered coefficient (ratio of backscattered to incident)
eta2=back./ntraj;




%-------------------------------------------------------------------------------------------------
```

```
% (4.) Sort energy data to determine energy deposition profile.
%-------------------------------------------------------------------------------------------------
% Convert the position data from centimeters to meters.
r=r./100;
z=z./100;
x=x./100;
y=y./100;

% Calculate the maximum and minimum r and z positions.
maxr=max(max(r));
maxz=max(max(z));

% Define constant differential elements.
delr=3e-9;
delz=3e-9;

% Create the rr and zz spatial grid vectors.
rr=0:delr:maxr;
zz=0:delz:maxz;

% Calculate length of the rr and zz vectors.
rnum=length(rr);
znum=length(zz);

% Energy loss vector initialization.
E_loss=zeros(znum,rnum);

% Loop through each electron and position
for ii=1:1:ntraj

   for jj=1:1:mat_size

    % If the electron is backscattered, break the loop.
    if z(ii,jj)<=0 & jj~=1
       break
    end

    if r(ii,jj)<maxr & z(ii,jj)<maxz
    % Determine the r and z matrix indices.
     indr=floor(((r(ii,jj))./delr)+1);
     indz=floor(((z(ii,jj))./delz)+1);
```

```
        % If the index is falsely low, make it the first index.
        if indr==0
           indr=1;
        end

        % If the index is falsely low, make it the first index.
        if indz==0
           indz=1;
        end

        % If the index is falsely high, make it the last index.
        if indr>rnum
           indr=rnum;
        end
        % If the index is falsely high, make it the last index.
        if indz>znum
           indz=znum;
        end

        % Calculate the energy lost at the given position
        E_loss(indz,indr)=E_loss(indz,indr)+deltaE(ii,jj);

        end   % Ends if statement
     end      % Ends for statement
end           % Ends for statement

% Calculate total energy lost by all electrons
sumeloss=sum(sum(E_loss));

% Calculate the fraction of the incident energy deposited
efficiency=sumeloss./Eo./ntraj;

% Calculate the given volume elements of the spatial grid
for ii=1:1:rnum-1
   volume(ii)=pi.*(rr(ii+1).^2-rr(ii).^2).*delz;
end

% Estimate the last two volumes to be equal
volume(rnum)=volume(rnum-1);
```

```
% Convert the energy lost into eV per electron per volume.
for ii=1:1:rnum
   E_loss(:,ii)=E_loss(:,ii).*1000./ntraj./volume(ii);
end

%-----------------------------------------------------------------------------------------------------
% (5.) Desired Output.
%-----------------------------------------------------------------------------------------------------

% Output the energy loss efficiency
fprintf('The energy loss efficiency is %3.3f\n',efficiency);

% Write the energy loss data to tab-delimited text files
dlmwrite('rdata.txt',rr);
dlmwrite('zdata.txt',zz);
dlmwrite('elossdata.txt',E_loss);

% Plot a contour of the energy loss
figure;                % Open a new figure
contour(rr,zz,E_loss);   % Create contour plot
axis equal;            % Force equal scale on both axes

% If interaction volume was requested, then plot
if plotswitch==1
   figure;                % Open a new figure
   % Determine how many trajectories to skip over when plotting the interaction volume
   nskip=1;
   % Loop through the desired trajectories and plot on the same graph
   for ii=1:nskip:ntraj
      plot(r(ii,:).*1e4,z(ii,:).*1e4);
      hold on;
   end
% Apply plot labels
title('Electron-Nanopillar Interaction Region');
xlabel('radial (\mum)');
ylabel('axial (\mum)');
end

toc;  % End the calculation timer

%-----------------------------------------------------------------------------------------------------
```

```
% (6.) Subfunction Routines.
%--------------------------------------------------------------------

%--------------------------------------------------------------------------
function [dEds]=funkeval(E)
%--------------------------------------------------------------------------
% Evaluates the energy loss function for a given energy
global rhoS AS ZanS JS Na  rhoW AW ZanW JW swtch
% Applies tungsten parameters
if swtch==0
   rho=rhoW;
   A=AW;
   Zan=ZanW;
   J=JW;
end
% Applies SiO2 parameters
if swtch==1
   rho=rhoS;
   A=AS;
   Zan=ZanS;
   J=JS;
end
% Calculates energy loss
dEds=(-78500.*rho.*Zan./A./E).*log((1.166.*E./J)+1);
return
%--------------------------------------------------------------------------

%--------------------------------------------------------------------------
function [step,phi]=rutherford(E)
%--------------------------------------------------------------------------
% Use Rutherford cross-section function to determine the step length and
% scattering angle
global rhoS AS ZanS JS Na  rhoW AW ZanW JW swtch
% Applies tungsten parameters
if swtch==0
   rho=rhoW;
   A=AW;
   Zan=ZanW;
   J=JW;
end
% Applies SiO2 parameters
```

```
if swtch==1
   rho=rhoS;
   A=AS;
   Zan=ZanS;
   J=JS;
end
% Calculate step length and scattering angle
alpha=3.4e-3.*Zan.^(.67)./E;
sigma=5.21e-21.*((Zan./E).^2).*(4.*pi./alpha./(1+alpha)).*((E+511)./(E+1024)).^2;
mfp=A.*(1./(Na.*rho.*sigma));
step=-mfp.*log(rand);
phi=acos((1-((2.*alpha.*rand)./(1+alpha-rand))));
return
%-------------------------------------------------------------------------


% END OF PROGRAM
%-----------------------------------------------------------------------------------------------
%-----------------------------------------------------------------------------------------------
%-----------------------------------------------------------------------------------------------
```

Appendix B

Example FlexPDE® Code

```
{-------------------------------------------------------------------------------------------------------}
{ FlexPDE Code for Simulating Electron Beam Heating of SiO2 Nanofibers}
{-------------------------------------------------------------------------------------------------------}

{-------------------------------------------------------------------------------------------------------}
TITLE 'Localized Heating in EBID Silicon Dioxide Nanostructures'
{-------------------------------------------------------------------------------------------------------}

{-------------------------------------------------------------------------------------------------------}
{ Define the cylindrical coordinate system}
COORDINATES
ycylinder('r','z')
{-------------------------------------------------------------------------------------------------------}

{-------------------------------------------------------------------------------------------------------}
{ Simulation parameters and controls}
SELECT
ngrid=10                                {Minimum number of grids}
regrid=on                               {Automatically refine mesh}
errlim=1e-3                             {Simulation accuracy}
contours=15                             {Minimum number of contours}
paintregions on                         {Color the defined regions}
paintmaterials on                       {Color the defined materials}
{-------------------------------------------------------------------------------------------------------}

{-------------------------------------------------------------------------------------------------------}
{ Definition of simulation variables}
VARIABLES
T                                   {Temperature}
{-------------------------------------------------------------------------------------------------------}

{-------------------------------------------------------------------------------------------------------}
{ Definition of constants and desired functions}
DEFINITIONS
oxide=500e-9                            {Oxide film thickness}
tungsten=500e-9                         {Tungsten film thickness}
base=oxide+tungsten                     {Convenience constant}
pillarad=50e-9                          {Nanofiber radius}
ht=500e-9                               {Nanofiber height}
I=500e-12                               {Incident beam current}
k                                       {Initialize thermal conductivity}
eloss=table("1.5kv_5000e_50r_500h.txt")     {Import energy loss data}
source=eloss*I                              {Heat source term}
```

```
fluxd_r=-k*dr(T)                                {Radial heat flux}
fluxd_z=-k*dz(T)                                {Axial heat flux}
fluxd=vector( fluxd_r, fluxd_z)                 {Resultant heat flux}
fluxdm=magnitude(fluxd)                         {Magnitude of heat flux}
{-------------------------------------------------------------------------------------------------------}

{-------------------------------------------------------------------------------------------------------}
{ Definition of partial differential equations}
EQUATIONS
div(-k*(grad(T)))-source = 0                    {Steady-state heat equation}
{-------------------------------------------------------------------------------------------------------}

{-------------------------------------------------------------------------------------------------------}
{ Definition of the simulated domain, regions and boundaries}
BOUNDARIES

{Define outer domain and boudary conditions}
  region 'Outer Domain'
  k=174                                         {Thermal conductivity of tungsten}
  start (0,0) natural(T)=0 line to (pillarad,0) to (pillarad,ht) to
    (pillarad+base,ht) value(T)=300 line to (pillarad+base,ht+base)
    to (0,ht+base) natural(T)=0 line to finish

{Define nanofiber as a silicon dioxide region}
  region 'Oxide Nanofiber'
  k=1.4                                         {Thermal conductivity of SiO2}
  start (0,0) line to (pillarad,0) to (pillarad,ht) to (0,ht) to finish

{Define top film as a tungsten region}
  region 'Tungsten Film'
  k=174                                         {Thermal conductivity of tungsten}
  start(0,ht) line to (pillarad+base,ht) to (pillarad+base,ht+tungsten)
    to (0,ht+tungsten) to finish

{Define substrate as a silicon dioxide region}
  region 'Oxide Substrate'
  k=1.4                                         {Thermal conductivity of SiO2}
  start(0,ht+tungsten) line to (pillarad+base,ht+tungsten) to
    (pillarad+base,ht+base) to (0,ht+base) to finish
{-------------------------------------------------------------------------------------------------------}


{-------------------------------------------------------------------------------------------------------}
```

```
{Request visual output of simulated solution}
PLOTS
{Contour plot of temperature}
  contour(T)
    painted                                {Color regions between contours}
    nominmax                               {Don't show min and max markers}
{Line plot of temperature down symmetry axis of nanofiber}
  elevation(T) from(0,0) to (0,ht)
{-------------------------------------------------------------------------------------------------------}

 END
{-------------------------------------------------------------------------------------------------------}
{-------------------------------------------------------------------------------------------------------}
{-------------------------------------------------------------------------------------------------------}
```

Appendix C

Chapter 1 Reprint Permissions

Figure 1-3

This is a License Agreement between Steven J. Randolph ("You") and American Institute of Physics ("American Institute of Physics"). The license consists of your order details, the terms and conditions provided by American Institute of Physics, and the payment terms and conditions.

License Number
1286540033378
Type of Use
Republish Portions
Licensed content title
Focused-electron-beam-induced deposition of freestanding three-dimensional nanostructures of pure coalesced copper crystals
Licensed content author
I. Utke, A. Luisier, P. Hoffmann, D. Laub, and P. A. Buffat
Licensed content publisher
American Institute of Physics
License date
Aug 12, 2005
Requestor Type
Third Party
Include other media
Yes
Number of portions
1

Figure 1-4

This is a License Agreement between Steven J. Randolph ("You") and AVS The Science & Technology Society ("AVS The Science & Technology Society"). The license consists of your order details, the terms and conditions provided by AVS The Science & Technology Society, and the payment terms and conditions.

License Number
1286540499523
Type of Use
Republish Portions
Licensed content title
Characteristics of nano electron source fabricated using beam assisted process
Licensed content author
Katsuhisa Murakami and Mikio Takai
Licensed content publisher
AVS The Science & Technology Society
License date
Aug 12, 2005
Requestor Type
Third Party
Include other media
Yes
Number of portions
1

Figure 1-5

This is a License Agreement between Steven J. Randolph ("You") and AVS The Science & Technology Society ("AVS The Science & Technology Society"). The license consists of your order details, the terms and conditions provided by AVS The Science & Technology Society, and the payment terms and conditions.

License Number
1286540294378
Type of Use
Republish Portions
Licensed content title
Resolution limits in electron-beam induced tungsten deposition
Licensed content author
K. T. Kohlmann-von Platen, J. Chlebek, M. Weiss, K. Reimer, H. Oertel, and W. H. Brünger
Licensed content publisher
AVS The Science & Technology Society
License date
Aug 12, 2005
Requestor Type
Third Party
Include other media
Yes
Number of portions
1

Figure 1-6

2 September 2005
Our ref: HG/smc/Sept.2005.jl023
Mr Steven Randolph

Srandol3@utk.edu

Dear Mr Randolph

MICROELECTRONIC ENGINEERING, Vol 78-79, No 1, 2005, Pages 307-313, Bret et al, 'Influence of …', 1 Figure only

As per your letter dated 9 August 2005, we hereby grant you permission to reprint the aforementioned material at no charge **in your thesis** subject to the following conditions:

1. If any part of the material to be used (for example, figures) has appeared in our publication with credit or acknowledgement to another source, permission must also be sought from that source. If such permission is not obtained then that material may not be included in your publication/copies.

2. Suitable acknowledgment to the source must be made, either as a footnote or in a reference list at the end of your publication, as follows:

"Reprinted from Publication title, Vol number, Author(s), Title of article, Pages No., Copyright (Year), with permission from Elsevier".

3. Reproduction of this material is confined to the purpose for which permission is hereby given.

4. This permission is granted for non-exclusive world **English** rights only. For other languages please reapply separately for each one required. Permission excludes use in an electronic form. Should you have a specific electronic project in mind please reapply for permission.

5. This includes permission for UMI to supply single copies, on demand, of the complete thesis. Should your thesis be published commercially, please reapply for permission.

Yours sincerely
Helen Gainford
Rights Manager

Vita

Steven J. Randolph was born on December 24, 1976 in Nashville, Tennessee. He graduated from Springfield High School, in Springfield, Tennessee, in 1995. Steven obtained a Bachelor of Science from the University of Tennessee, Knoxville in 2002. He graduated summa cum laude with a major in chemistry. Upon completion of his undergraduate work, Steven continued his work at the University of Tennessee by entering the graduate program in Materials Science & Engineering. Following the completion of his Master of Science, he continued his work at the university in pursuit of a Ph.D. in Materials Science & Engineering.